Electronic and Structural Properties of the Ge/GeO$_2$ Interface through Hybrid Functionals

THÈSE N^O 5363 (2012)

PRÉSENTÉE LE 24 MAI 2012
À LA FACULTÉ DES SCIENCES DE BASE
CHAIRE DE SIMULATION À L'ÉCHELLE ATOMIQUE
PROGRAMME DOCTORAL EN PHYSIQUE

ÉCOLE POLYTECHNIQUE FÉDÉRALE DE LAUSANNE

POUR L'OBTENTION DU GRADE DE DOCTEUR ÈS SCIENCES

PAR

Jan Felix BINDER

acceptée sur proposition du jury:

Prof. O. Schneider, président du jury
Prof. A. Pasquarello, directeur de thèse
Prof. N. Marzari, rapporteur
Dr M. Perego, rapporteur
Dr G. Pourtois, rapporteur

(EPFL

ÉCOLE POLYTECHNIQUE
FÉDÉRALE DE LAUSANNE

Suisse
2012

Abstract

The performance of silicon based microelectronic circuits reaches the end of the roadmap. New material systems are required for further improvements in speed and power consumption. Germanium is a possible candidate to substitute silicon for microelectronic devices. Its hole mobility is the highest of all semiconductor materials. Together with its lower band gap it could be an ideal material for energy-saving devices.

This thesis is dedicated to first principles studies of the Ge/GeO$_2$ interface through hybrid density functional theory. The substoichiometric region of the interface is of special interest. A wide substoichiometric region is supported by total energy calculations of a set of crystalline model systems. An unexpected structure organization was found through molecular dynamics simulations of substoichiometric GeO. We found that a majority of germanium and oxygen atoms are threefold coordinated, forming valence alternation pairs (VAPs). A detailed energetic analysis located the VAPs in the low-oxygen region of the interface. VAPs show interesting properties : They are prone to charge trapping. The electron trapping level might explain the bad performance of n-type doped devices. Furthermore, VAPs might be at the origin of the difficulties of H passivation at the Ge/GeO$_2$ interface.

Since threefold Ge atoms are negatively charged and threefold O atoms are positively charged, VAPs give rise to dipoles. These dipoles may reduce the interface dipole created by the electronegativity difference in the Ge–O bond. With this mechanism, we can explain the wide range of experimental valence band offsets (VBOs) with the occurrence of different density levels of VAPs at the Ge/GeO$_2$ interface. This suggestion is further confirmed by the determination of the VBO and Ge 3d core-level shift for an atomistic model structure of the Ge/GeO$_2$ interface. Both values are systematically lower than typical experimental values for the Ge/GeO$_2$ interface. Taking the extra dipole into account, our calculated VBOs and XPS shifts are in excellent agreement with experimental values. These results confirm that the structural properties of the Ge/GeO$_2$ interface deviate significantly from its Si counterpart.

Keywords : Ge/GeO$_2$ interface, valence alternation pairs, valence band offset, core-level spectroscopy, hybrid functionals.

Zusammenfassung

Die auf Silizium basierende Mikroelektronik erreicht das Ende ihrer Miniaturisierung. Schon in einigen Jahren, können die von der Halbleiterindustrie selbst auferlegten Ziele zur Verkleinerung und Effektivitätssteigerung mit Silizium als Halbleitermaterial aufgrund fundamentaler physikalischer Gesetze nicht mehr erreicht werden.

Um die gesteckten Ziele einer Verdoppelung der Leistungsfähigkeit von integrierten Schaltkreisen alle zwei Jahre weiter zu ermöglichen, sind neue Materialien nötig, die Silizim ergänzen oder gar ersetzt. Germanium zeigt Vorteile gegenüber Silizium. Die Ladungsträgerbeweglichkeit der Höcher ist die höchste aller Halbleitermaterialien. Die relativ klein Bandlücke zwischen besetzten und unbesetzten Zuständen ermöglicht energieeffizientere Schaltungen, was gerade im stetig wachsenden Markt der mobilen Endgeräte von Nutzen ist.

Germanium hat allerdings auch Nachteile gegenüber Silizium. Germaniumdioxid ist thermisch weniger stabil als sein Silizum Gegenstück. Dadurch zeigt die Grenzfläche zwischen Halbleiter und Oxid eine wesentlich höhere Dichte an Bindungsfehlern zwischen den beteiligten Atomen als an der entsprechenden Silizium Grenzfläche.

Die vorliegende Doktorarbeit untersucht die Eigenschaften der Ge/GeO_2 Grenzschicht mit den Methoden der Hybrid-Dichtefunktionaltheorie. Dem unterstoichometrischen Oxid, das an der Grenzfläche auftritt, wird besondere Aufmerksamkeit gewidmet. In Molekulardynamik Simulationen hat sich eine von Silizium unbekannte Anordnung der Atome gezeigt. Ein Teil der Ge und O Atome hat drei nächste Nachbarn. Die Ge Atome sind dadurch negativ geladen, wohingengen die dreifach gebundenen O Atome positiv geladen sind. In Siliziumoxid haben Siliziumatome immer vier nächste Nachbarn und Sauerstoffatome sind immer mit zwei Siliziumatomen gebunden. Wir zeigen, dass die Konzentration dieser intrinsischen Defekte Einfluss auf den Grenzflächendipol hat. Dies hat Auswirkungen auf den Energieabstand zwischen Valenzbändern an beiden Seiten der Grenzfläche. Darüber hinaus, verändert es den Abstand der in Röntgenphotoelektronenspektroskopie gemessenen Kernzuständen. Dies kann die Schwankungen in diesen experimentell zugänglichen Größen erklären, die abhängig vom Fertigungsverfahren der Oxidschicht, an der Grenzfläche auftreten.

Schlüsselwörter: Ge/GeO_2 Grenzfläche, Valenzebandversatz, Röntgenphotoelektronenspektroskopie, Hybrid-Dichtefunktionaltheorie.

Contents

Contents

1 Introduction

1.1 Historical overview

Germanium was first predicted in 1871 by D. I. Mendeleev, a Russian chemist. [1] It was first found and characterized by Clemens Alexander Winkler close to Freiburg Germany. He published his findings in two detailed articles in 1886 and 1887 [152, 153]. Up to the late 1930s, germanium was believed to be a poorly conducting metal. Also nowadays pure germanium bars are labeled "Germanium Metal".

Germanium was the material used in the first transistor constructed by John Bardeen, William B. Shockley, and Walter H. Brattain in December 1947. The invention of the germanium transistor has been one of the most important events in shaping modern day life. It is difficult to come up with any modern day activity which is not influenced by the transistor. Bardeen, Shockley, and Brattain were honoured with the Nobel prize in physics 1956 [133].

In the following years the semiconductor industry began to grow. The fabricated devices became smaller and smaller, while the performance of the transistor could be increased. A remaining problem was the purity of the germanium crystals. Making germanium of the required purity was proving to be a serious problem, and limited the number of transistors that actually worked from a given batch of material. The temperature dependent sensitivity of germanium also limited the usefulness. Silicon overcame these problems, and the first silicon based transistor was made in January 1954 at Bell Laboratories [139]. This was the beginning of the "Silicon Age".

A further advantage of silicon compared to germanium is the stability of its oxide. Silicon dioxide, also known as silica, is most commonly found in nature as sand or quartz. The good match between silicon dioxide and silicon leads to extremely small defect densities at the Si/SiO_2 interface. [2] With this new material system showing very good interface properties it

---

1. He is the creator of the first version of the periodic table of elements.
2. The defect density of pure Si/SiO_2 interface is not so small, but hydrogen can be used to passivate electrically active defects.

becomes possible to realize a new transistor principle. The metal-oxide-semiconductor field effect transistor. Germanium dioxide is less stable and therefore not optimal for the new device technology. Germanium disappeared from most transistors by the late 1960s.

At this time one also starts to produce electronic circuits in clean environments. The reduction of dust together with use of purer semiconductor materials allows one to produce smaller structures. In 1965, Gordon E. Moore, a co-founder of Intel, analysed that the number of transistors in integrated circuits had doubled approximately every two years since 1958, and he predicted that this trend would continue [102]. Since those days, the semiconductor industry has overcome all technical problems of miniaturization and has continued to follow Moore's law. In the year 1971, Intel built the first commercially available microprocessor, the Intel 4004. It was made in a 10 μm process, and had 2300 transistors. The processor performed 92'000 instructions per second. 40 years later, Intel sells microprocessors within the 32 nm technology, with half a billion transistors.

1.2   Metal oxide semiconductor field effect transistors

Today, the most used transistor type is the metal-oxide-semiconductor field effect transistor (MOSFET). Its physical principal was first patented by Julius Edgar Lilienfeld in 1925. The first working transistor of this type was constructed at Bell Labs in 1959 by Dawon Kahng and Martin Atalla. During the last 50 years the MOSFET transistor has undergone a variety of technological improvements, but the basic principle has not changed. The MOSFET behaves like a parallel plate capacitor: when a gate voltage is applied to the gate, charges on the metal are compensated by opposite charges in the semiconductor. These latter charges form the channel connecting the source and the drain of the transistor.

In the following a n-channel device is discussed. In this device, the channel carriers are electrons. A common MOSFET is a four-terminal device that consists of a p-type semiconductor substrate into which two n-type doped regions, the source and drain, are formed (compare Fig. 1.1). The gate oxide is formed by thermal oxidation of Si resulting in a high quality interface with SiO_2. The metal contact on the insulator is called the gate.[3] The SiO_2 region separates the two electrodes and acts as dielectric. The distance between the two n-p junctions is the channel length L. A MOSFET is surrounded by a thick oxide to electrically isolate it from adjacent devices. When a low voltage is applied to the gate, the main channel is shut off, and the source and drain electrodes correspond to two p-n junctions connected back to back. When a sufficiently large positive bias is applied to the gate, a channel is formed between source and drain. The two contacts are then connected by a conducting surface n-channel through which a large current can flow. The conductance of this channel can be modulated by the gate voltage.

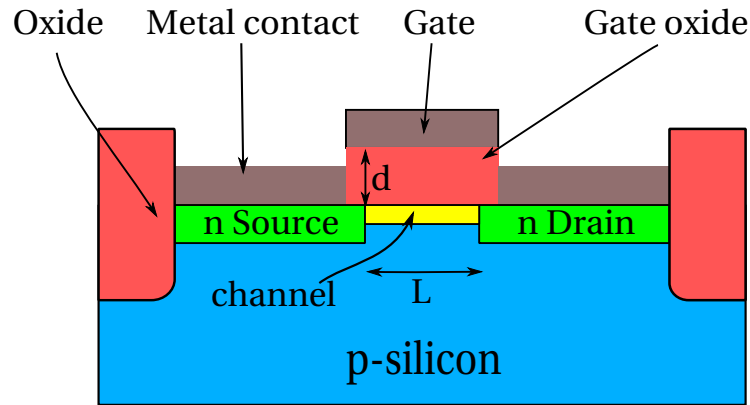3. Today doped polysilicon is more commonly used as gate electrode.

Figure 1.1 – Schematic picture of a MOSFET device.

The capacitance C of the transistor is given by

$$C = \frac{A\epsilon_r\epsilon_0}{d} \tag{1.1}$$

where A is the capacitor area, ϵ_r is the relative dielectric constant of the gate dielectric, and ϵ_0 the vacuum permittivity. With decreasing gate dielectric thickness d the capacitance of the structure increases, and so does the number of charges in the channel. This is the main mechanism responsible for the higher performance of new MOSFET transistors upon reduction of the device dimensions. It also allows the integration of a higher number of transistors on a chip, enabling higher speed and reduced cost.

A problem arising from the scaling of the oxide layer thickness concerns the leakage current flowing through the MOSFET. When the thickness of the gate dielectric becomes too small charge carriers can flow through it. Quantum mechanical tunnelling is the mechanism responsible for this.

An alternative way of increasing the capacitance is using as gate oxide an insulator with a higher dielectric constant. This increases the capacitance of the transistor and the number of charges in the channel without changing the thickness of the barrier. This improves the performance of the transistor and reduces the leakage current flow through the structure [69]. In this context nitrides sometimes replace oxides as dielectrics, because of their higher dielectric constants [69]. For further improvements, materials with much higher dielectric

constants are needed. HfO$_2$ and ZrO$_2$ belong to the class of so called high-κ materials. When a high-κ metal oxide like ZrO$_2$ or HfO$_2$ is deposited on an semiconductor substrate, a low-κ interfacial layer forms. This low-κ interfacial layer decreases the effective dielectric constant [69]. To quantify the effect of increased dielectric constants in the oxide region of the MOSFET, an effective oxide thickness (EOT) is usually given for the transistor. The EOT value is defined as the required thickness of SiO$_2$ to achieve an electrically equivalent capacitance as the high-κ material [69]. Through high-κ oxides like HfO$_2$ or ZrO$_2$, the leakage current flow through silicon-based devices can be reduced by several orders of magnitude allowing for further scaling of the MOSFETs [69].

1.3 The Ge/GeO$_2$ interface

As the scaling of silicon-based MOSFETs is approaching its technological and fundamental limits, new materials are needed to further improve the performance of integrated circuits. In this context, germanium has been shown to display several advantages over silicon for the use in field-effect transistors [73]. For instance, the mobilities of both holes and electrons are significantly higher than in silicon. Germanium has even the highest p-type mobility of all Group IV and III-V semiconductor materials [75]. The band gap is an important parameter of a semiconductor material, because it affects the supply voltage and the scalability of a device. The germanium band gap (E_g = 0.66 eV) is significantly smaller than the silicon band gap (E_g = 1.12 eV), but still large enough to avoid instabilities through thermionic emissions and band-to-band tunneling [121]. Moreover, the lower band gap makes it possible to operate devices at lower voltages [73]. This reduces the power consumption, making it interesting especially for the growing market of mobile devices. Another advantage is that germanium requires lower temperatures for dopant activation which might allow for an easier integration with a high-κ dielectric material like HfO$_2$ [73]. However, germanium-oxide interfaces generally show considerably higher defect densities than their silicon counterparts [4]. This is related to the lower stability of GeO$_2$ compared to SiO$_2$. GeO$_2$ has a lower melting point and is soluble in water, which makes it vulnerable against environmental influences. At the interface with germanium, it even evaporates to GeO in gas phase: [123, 104, 80, 150]

$$GeO_2 + Ge \rightarrow 2GeO(g) \tag{1.2}$$

where the GeO molecules leave the interfacial region through the GeO$_2$ cap layer. In its amorphous solid phase, substoichiometric GeO desorbs already at temperatures of 400 K, whereas its silicon counterpart is stable until 1100 K [39]. Through this process, even an abrupt interface becomes frayed and an unstructured interfacial region appears. This leads to defect densities at Ge/GeO$_2$ interfaces, which are much too high for operating electrical devices [150]. To overcome the desorption of GeO at the interface, Lee *et al.* proposed a high-pressure oxidation method [89]. Through this growth technique, interface defects would strongly be reduced ($D_{it} = 2 \cdot 10^{11} \text{eV}^{-1}\text{cm}^{-2}$). Because of the thermal instability of GeO$_x$, a natural way of reducing defect densities is through a low-temperature oxidation. Recently,

Wada *et al.* proposed a neutral beam oxidation process at low-temperature, yielding even lower D$_{it}$ densities at the Ge/GeO$_2$ interface [149].

Low defect densities at semiconductor/oxide interfaces can also be reached through defect passivation. This means, that an electrically active defect, like a dangling bond (DB), could be passivated by an additional atom. For instance, the Si/SiO$_2$ interface shows high concentrations ($\sim 10^{12}$cm^{-2}) of electrically active centers [136]. These defect centers are mostly Si dangling bonds. They are generated at the interface because of lattice mismatch [136]. The Si dangling bond is paramagnetic and thus detectable in electron spin resonance (ESR) experiments [38]. Upon annealing with hydrogen, almost all dangling bond centers are electrically passivated through the formation of Si–H bonds [38].

Also from this point of view the Ge/GeO$_2$ interface differs from its silicon counterpart. It shows no relevant ESR signals and the passivation with hydrogen does not work [1]. ESR spectra of dangling bonds and the passivation with hydrogen are similar for amorphous Ge and amorphous Si. The small differences can be explained by differing spin-orbit splittings in the two materials [25, 137]. Therefore, the different behaviour at the interface must come from the substoichiometric GeO$_x$. Hence, to make progress, it is important to achieve a detailed understanding of the electronic and structural properties of Ge/GeO$_2$ interfaces.

X-ray photoemission spectroscopy (XPS) is a standard analytical tool for the characterization of semiconductor/oxide interfaces. Core-electrons are emitted and their binding energy is inferred from their kinetic energy. At Ge/GeO$_2$ interfaces, this technique is sensitive to the local structure around Ge atoms and to the electrostatic discontinuity at the interface. For Ge/GeO$_2$ interfaces grown by thermal oxidation, a shift of $\Delta E_{\mathrm{XPS}} = 3.3 \pm 0.1$ eV is generally measured for the Ge 3d core level between nonoxidized Ge in the substrate and fully oxide Ge in GeO$_2$ [129, 124, 106, 42, 101, 79]. In experiments in which the interfaces are grown with oxidizing agents such as O$_3$ (Ref. [119]) and atomic O (Ref. [158]), much larger values (3.7–3.8 eV) have been reported. The spread in the experimentally determined values likely results from the different growth conditions.

The measured XPS shifts can be used to derive valence band offsets (VBOs) through the application of Kraut's method [84, 43]. For the interfaces grown with reactive O species, this method yielded VBOs around 4.5 eV [119, 158]. Valence band offsets can alternatively be obtained directly from photoemission spectra in which the onsets of the valence band edges of both Ge and GeO$_2$ appear. This direct procedure has been found to yield a VBO of 4.0 eV for Ge/GeO$_2$ interfaces obtained by thermal oxidation [106], while a larger VBO value is confirmed for structures grown by O$_3$ oxidation (4.3 eV) [119]. Overall, on the basis of the available experimental data, it appears that the shift ΔE_{XPS} and the VBO vary consistently, supporting that the interfaces achieved with different growth conditions differ in their band alignment.

1.4   Motivation

The improvement of the Ge/GeO$_2$ interface is of technological interest. Experimental and theoretical investigations are needed to understand the differences between Si/SiO$_2$ and Ge/GeO$_2$ interfaces. A special focus lies in the structure of the substoichiometric region at the interface, which appears at the origin of the main differences between Si-based and Ge-based interfaces. To model the amorphous structure in this region, we plan to use molecular dynamics simulations which allow us to explore unexpected structural organizations. The identified structure should be consistent with XPS shifts and valence band offset measured experimentally.

1.5   Outline of the thesis

The present thesis is organized as follows. In Chapter 2 we give a description of the methods and techniques used in this thesis. Most attention is focused on density functional theory. Which is the electronic structure theory used in this work. Chapter 3 discusses the stability of Ge and of GeO$_2$ in different crystalline phases compared to its Si counterparts. We study substoichiometric Ge oxides through a series of crystalline models representing the various oxidation states. We evaluate deviations with respect to a bond-energy description in terms of penalty energies for intermediate oxidation states of Ge. Corresponding bond length variations and band gaps are also given. The calculated penalty energies are significantly lower than for Si indicating higher stability of the substoichiometric phase at Ge/GeO$_2$ interfaces compared to Si/SiO$_2$ interfaces. Next, we study the stability of oxygen vacancies across the Ge/HfO$_2$ interface. On the semiconductor side, the formation energies are obtained for substoichiometric GeO$_x$ of varying x through the previously calculated penalty energies. On the hafnium oxide side, the interface is modeled through bulk models with aligned band structures. Formation energies are compared for different charge states and electron chemical potentials. The oxygen vacancy is found to be most stable in the interfacial germanium oxide layer, for both p-type and n-type doping. This favors the formation of substoichiometric GeO$_x$, consistent with experimental observations.

As representatives of the interfacial substoichiometric GeO$_x$, we model disordered GeO structures in Chapter 4. This is done with *ab initio* molecular dynamics (MD). The resulting structure shows a predominance of threefold coordinated Ge and O atoms. We also generate substoichiometric models through bond-switching Monte-Carlo simulations, which preserve the fourfold Ge and the twofold O coordinations. These differing structures are energetically competitive. Alignment of their electron densities of states to that of GeO$_2$ reveals that the band gap reduction is similar for both structures, mainly occurring through a shift of the valence band edge.

Some important implications due to the formation of valence alternation pairs are discussed in Chapter 5. First, electron and hole trapping in substoichiometric germanium oxides are

investigated. The MD model shows threefold coordinated O and Ge atoms forming valence alternation pairs and is found to present trap states for both carriers. The trapping states correspond to the formation and breaking of Ge–Ge bonds. The associated defect levels are determined within a band diagram of the Ge/GeO$_2$ interface. Next, we compare the Ge–Ge bond energy with the formation energy of a valence alternation pair as the O concentration varies across the Ge/GeO$_2$ interface. Hole trapping energies are calculated for three atomistic models with different O concentrations: bulk Ge with isolated O atoms, amorphous GeO, and amorphous GeO$_2$ with an O vacancy. The reaction is then broken down in three steps involving the breaking of a Ge–Ge bond, charge transfer processes involving dangling bonds, and the formation of a threefold coordinated O atom. The energy of each elemental reaction is estimated through suitable model calculations. The charge transition levels resulting from this analysis agree with those obtained for the atomistic models. Our estimates indicate that hole trapping at low O concentrations occurs at no energy cost for p-type germanium owing to the formation of threefold-coordinated O atoms. Applied to n-type Ge, our analysis indicates that electron trapping in dangling bonds obtained from the breaking of Ge–Ge bonds is unfavorable. The formation energy of a valence alternation pair is evaluated and discussed in relation to previous results. In the last part of this chapter, we study the role of hydrogen at the Ge/GeO$_2$ interface.

Band offsets of the Ge/GeO$_2$ interface are calculated in chapter 6. We consider an atomistic model in which amorphous GeO$_2$ is connected to crystalline Ge through a suboxide transition region showing regular structural parameters. The band offsets are obtained through the application of an alignment scheme which reproduces the experimental band gaps of the interface components. Next, we investigate possible origins for the large variation of band offsets measured at Ge/GeO$_2$ interfaces. We consider atomistic model interfaces with both amorphous and crystalline oxides, in which the bond density reduction accounts for the mass densities of the two interface components. To the extent that all the Ge atoms are fourfold coordinated and all the O atoms are twofold coordinated, the band offsets are found to remain constant within 0.1 eV. We then investigate the role of valence alternation pairs consisting of negatively charged Ge dangling bonds and positively charged threefold coordinated O atoms, which have been suggested to occur in sizeable concentrations in substoichiometric germanium oxide. A valence alternation pair is introduced in one of the atomistic models and is found to affect the band alignment by contributing to the interface dipole. The calculated band offsets shift by 0.7 eV for an areal concentration of valence alternation pairs corresponding to one pair per 8 Ge interface atoms. These pairs would act as fixed charges and are not expected to directly contribute to the defect density in the germanium band gap. The occurrence of such bonding patterns offers a possible explanation for the large range of valence band offsets measured at this interface.

The Ge core-level shift across the Ge/GeO$_2$ interface is determined in chapter 7. We first assess the accuracy achieved within our theoretical framework by comparing calculated and measured core-level shifts for a set of Ge–based molecules. The comparison with experimental data is impressive and results in rms deviations of only 0.04 and 0.02 eV for core-level shifts

calculated with semilocal and hybrid density functionals, respectively. We also compare calculated core-level shifts at the Ge(001)-$c(4 \times 2)$ surface with high-resolution X-ray photoemission spectra finding similar agreement. We then turn to the Ge/GeO$_2$ interface, which we describe with atomistic superlattice models showing alternating layers of Ge and GeO$_2$. The adopted models include a substoichiometric transition region in which all Ge atoms are fourfold coordinated and all O atoms are twofold coordinated, as inferred for Si/SiO$_2$ interfaces. Since the calculation of core-level shifts involves charged systems subject to finite-size effects, we use two different methods to ascertain the core-level shift ΔE_{XPS} between the oxidation state Ge^0 and Ge^{+4} across the interface. In the first method, core-hole relaxations are first evaluated in bulk models of the interface components and then complemented by the initial-state shift calculated across the interface, while the second method consists in direct interface calculations corrected through classical electrostatics.

We conclude this thesis in chapter 8.

2 Methods

Electrons and nuclei are the fundamental particles that determine the properties of atoms, molecules and condensed matter. The theory to describe all these systems is quantum mechanics. Thus our starting point is the Hamiltonian for the system of electrons and nuclei,

$$\hat{H} = -\frac{\hbar^2}{2m_e}\sum_i \nabla_i^2 - \sum_{i,I}\frac{Z_I e^2}{|\mathbf{r}_i - \mathbf{R}_I|} + \frac{1}{2}\sum_{i\neq j}\frac{e^2}{|\mathbf{r}_i - \mathbf{r}_j|} - \sum_I \frac{\hbar^2}{2M_I}\nabla_I^2 + \frac{1}{2}\sum_{I\neq J}\frac{Z_I Z_J e^2}{|\mathbf{R}_I - \mathbf{R}_J|}, \tag{2.1}$$

where electrons are denoted by lower case subscripts and nuclei, with charge Z_I and mass M_I, are denoted by upper case subscripts. Such a system is far too complicated for direct calculations [96].

Born-Oppenheimer approximation

This leads to the first approximation: The separation of the ionic kinetic energy. The masses of the electrons and of the nuclei are very different. The mass of a proton (neutron) is ~ 1800 times larger than the mass of an electron. Hence, the inverse mass of the nuclei $1/M_I$ [96] is very small. A perturbation series can be defined in terms of this parameter and is expected to have general validity for the full interacting system of electrons and nuclei. The Hilbert space can be separated in a electronic and a ionic part $\mathcal{H} = \mathcal{H}^{\text{el}} \otimes \mathcal{H}^{\text{ion}}$. To simplify the following discussion the mass of the nuclei is set to infinity. Then the kinetic energy of the nuclei can be ignored.

Ignoring the nuclear kinetic energy, the fundamental Hamiltonian for the theory of electronic structure can be written as [96]

$$\hat{H} = \hat{T} + \hat{V}_{\text{ext}} + \hat{V}_{\text{ee}} + E_{\text{II}}. \tag{2.2}$$

In Hartree atomic units $\hbar = m_e = e = 4\pi/\epsilon_0 = 1$ these terms may be written in a simple form.

The kinetic energy operator for the electrons $\hat{T}$ is

$$\hat{T} = -\frac{1}{2}\sum_i \nabla_i^2, \tag{2.3}$$

$\hat{V}_{\text{ext}}$ is the potential acting on the electrons due to the nuclei,

$$\hat{V}_{\text{ext}} = \sum_{i,I} V_I \left(|\mathbf{r}_i - \mathbf{R}_I|\right), \tag{2.4}$$

$\hat{V}_{\text{ee}}$ is the electron-electron interaction,

$$\hat{V}_{\text{ee}} = \frac{1}{2}\sum_{i \neq j} \frac{1}{|\mathbf{r}_i - \mathbf{r}_j|}, \tag{2.5}$$

and the final E_{II} is the classical interaction between the nuclei and could contain any other relevant terms that contributes to the total energy of the system. Here the effect of the nuclei upon the electrons is included in a fixed external potential which acts on the electronic variables.

The electron density $n(\mathbf{r})$, plays a central role in electronic structure theory and is given by the expectation value of the density operator $\hat{n}(\mathbf{r}) = \sum_{i=1,N} \delta(\mathbf{r} - \mathbf{r_i})$,

$$n(\mathbf{r}) = \frac{\langle\Psi|\hat{n}(\mathbf{r})|\Psi\rangle}{\langle\Psi|\Psi\rangle} = N\frac{\int d^3r_2\ldots d^3r_N \sum_{\sigma_1} |\Psi(\mathbf{r},\mathbf{r_2},\mathbf{r_3},\ldots,\mathbf{r_N})|^2}{\int d^3r_1 d^3r_2\ldots d^3r_N |\Psi(\mathbf{r_1},\mathbf{r_2},\mathbf{r_3},\ldots,\mathbf{r_N})|^2}, \tag{2.6}$$

which has this form because of the anti-symmetry of the wave function in all the electron coordinates.

The total energy is the expectation value of the Hamiltonian,

$$E = \frac{\langle\Psi|\hat{H}|\Psi\rangle}{\langle\Psi|\Psi\rangle} = \langle\hat{T}\rangle + \langle\hat{V}_{\text{ee}}\rangle + \int d^3r\ V_{\text{ext}}(\mathbf{r})n(\mathbf{r}) + E_{\text{II}}, \tag{2.7}$$

where the term involving the external potential has been explicitly written as a simple integral over the density function. The final term E_{II} resulting from the electrostatic nucleus-nucleus interaction is essential in total energy calculation, but is only a classical additive term in the theory of electronic structure.

Hellmann-Feynman theorem

The Hellmann-Feynman theorem connects the derivative of the total energy with respect to an external parameter with the expectation value of the derivative of the Hamiltonian with respect to the same parameter:

$$\frac{dE_\lambda}{d\lambda} = \frac{d}{d\lambda}\langle\Psi(\lambda)|\hat{H}_\lambda|\Psi(\lambda)\rangle = \langle\Psi(\lambda)|\frac{d\hat{H}_\lambda}{d\lambda}|\Psi(\lambda)\rangle. \tag{2.8}$$

The force is defined as the negative derivative of the total energy with respect to a displacement. Thus, the Hellmann-Feynman theorem can be used to calculate atomic forces:

$$F_{i\alpha} = -\langle \Psi | \frac{d\hat{H}(q_{i\alpha})}{dq_{i\alpha}} | \Psi \rangle,$$ (2.9)

where $q_{i\alpha}$ is the displacement of atom i along the direction α. The only relevant parts of the Hamiltonian (2.1) to determine the atomic forces are the electron-nucleus (given through V_{ext}) and the nucleus-nucleus interaction terms.

2.1 Density functional theory

After separation of the motion of the nuclei, the system has still $\sim 10^{23}$ degrees of freedom. This remains still too complex to solve. Density functional theory (DFT) simplifies the problem. The idea is to describe the interacting many body problem by only one scalar function, the density $n(\mathbf{r})$. The basic theorems of the density functional formalism were derived by Hohenberg and Kohn [70]. By extending an argument for independent fermions, Levy [91] provided a simpler and more general derivation, which will be described in the following. The starting point is the Hamiltonian in Eq. (2.2). For all "N-representable" densities $n(\mathbf{r})$, those which can be obtained from some anti-symmetric wave function $\Psi(\mathbf{r_1}, \mathbf{r_2}, \cdots, \mathbf{r_N})$, Levy defined the functional

$$F[n] = \min_{\Psi \to n} \langle \Psi | \hat{T} + \hat{V}_{\text{ee}} | \Psi \rangle$$ (2.10)

where the minimum is taken over all Ψ that give the density n. $F[n]$ is universal in the sense that it refers neither to a specific system nor to the external potential $V_{\text{ext}}(\mathbf{r})$. If we denote E_{GS}, Ψ_{GS}, and $n_{\text{GS}}(\mathbf{r})$ to be the energy, the wave function, and the density of the electronic ground state, respectively, then the two basic theorems of DFT are

$$E[n] \equiv \int d\mathbf{r} \, V_{\text{ext}}(\mathbf{r}) n(\mathbf{r}) + F[n] \geq E_{\text{GS}}$$ (2.11)

for all N-representable $n(\mathbf{r})$ and

$$\int d\mathbf{r} \, V_{\text{ext}}(\mathbf{r}) n_{\text{GS}}(\mathbf{r}) + F[n_{\text{GS}}] = E_{\text{GS}}.$$ (2.12)

The density and the external potential rather than some other properties of the particles, play a special role, in the Hohenberg-Kohn theorems. These quantities enter the total energy in Eq. (2.7) explicitly only through the simple bilinear integral term $\int d^3 r \, V_{\text{ext}}(\mathbf{r}) \, n(\mathbf{r})$. If there were other terms in the Hamiltonian having this form, then each such pair of external potential and particle density would obey a Hohenberg-Kohn theorem. Within this model, one can rigorously generalize all the above arguments to include two types of densities, the particle density $n(\mathbf{r}) = n(\mathbf{r}, \sigma = \uparrow) + n(\mathbf{r}, \sigma = \downarrow)$ and the spin density $s(\mathbf{r}) = n(\mathbf{r}, \sigma = \uparrow) - n(\mathbf{r}, \sigma = \downarrow)$. This

leads to an energy functional

$$E = E_{HK}[n, s] \equiv E'_{HK}[n] \tag{2.13}$$

where in the last form it is assumed that $[n]$ denotes a functional of the density which depends upon both the spatial position $\mathbf{r}$ and the spin σ. To use these theorems in practical calculations, one transforms the interacting system in the ground state to an auxiliary system of non-interacting particles subject to a self-consistency condition as explained in the following:

$$\hat{H}^{\sigma}_{aux} = -\frac{1}{2}\nabla^2 + V^{\sigma}(\mathbf{r}). \tag{2.14}$$

The Kohn-Sham approach to the full interacting many-body problem consists in rewriting the functional of Eq. (2.12) in the form

$$E_{KS} = T_s[n] + \int d\mathbf{r}\, V_{ext}(\mathbf{r})n(\mathbf{r}) + E_H[n] + E_{II} + E_{ex}[n] \tag{2.15}$$

where

$$T_s = -\frac{1}{2}\sum_{\sigma}\sum_{i=1}^{N^{\sigma}}\langle \Psi^{\sigma}_i | \nabla^2 | \Psi^{\sigma}_i \rangle \tag{2.16}$$

is the independent particle kinetic energy and

$$E_H[n] = \frac{1}{2}\int d^3r d^3r' \frac{n(\mathbf{r})n(\mathbf{r}')}{|\mathbf{r} - \mathbf{r}'|} \tag{2.17}$$

is the classical Coulomb interaction energy of the electron density $n(\mathbf{r})$ interacting with itself.

Finding the solution of the Kohn-Sham auxiliary system for the ground state can be viewed as a minimization problem with respect to the density $n(\mathbf{r})$. Since T_s is explicitly expressed as a functional of the orbitals but all other terms are considered to be functionals of the density, one can vary the wave functions and use the chain rule to derive the variational equation

$$\begin{aligned}\frac{\delta E_{KS}}{\delta \Psi^{\sigma*}_i(\mathbf{r})} = &\frac{\delta T_s}{\delta \Psi^{\sigma*}_i(\mathbf{r})} \\ &+ \left[\frac{\delta E_{ext}}{\delta n(\mathbf{r}, \sigma)} + \frac{\delta E_H}{\delta n(\mathbf{r}, \sigma)} + \frac{\delta E_{xc}}{\delta n(\mathbf{r}, \sigma)}\right]\frac{\delta n(\mathbf{r}, \sigma)}{\delta \Psi^{\sigma*}_i(\mathbf{r})} = 0\end{aligned} \tag{2.18}$$

subject to the orthonormalization constraints

$$\langle \Psi^{\sigma}_i | \Psi^{\sigma'}_j \rangle = \delta_{i,j}\delta_{\sigma,\sigma'}. \tag{2.19}$$

This is equivalent to the Rayleigh-Ritz principle and the general derivation of the Schrödinger

equation [96], except for the explicit dependence of E_H and E_{xc} on n. From Eq. (2.16) follows

$$\frac{\delta T_s}{\delta \Psi_i^{\sigma *}(\mathbf{r})} = -\frac{1}{2}\nabla^2 \Psi_i^\sigma(\mathbf{r}) \qquad \text{and} \qquad \frac{\delta n^\sigma(\mathbf{r})}{\delta \Psi_i^{\sigma *}(\mathbf{r})} = \Psi_i^\sigma(\mathbf{r}). \tag{2.20}$$

This leads to the Schrödinger-like Kohn-Sham equations:

$$(H_{KS}^\sigma - \epsilon_i^\sigma)\Psi_i^\sigma(\mathbf{r}) = 0, \tag{2.21}$$

where the ϵ_i are the eigenvalues and H_{KS} is the effective Hamiltonian

$$H_{KS}^\sigma = -\frac{1}{2}\nabla^2 + V_{KS}^\sigma(\mathbf{r}), \tag{2.22}$$

with

$$\begin{aligned}
V_{KS}^\sigma(\mathbf{r}) &= V_{ext}(\mathbf{r}) + \frac{\delta E_H}{\delta n(\mathbf{r},\sigma)} + \frac{\delta E_{xc}}{\delta n(\mathbf{r},\sigma)} \\
&= V_{ext}(\mathbf{r}) + V_{ee}(\mathbf{r}) + V_{xc}^\sigma(\mathbf{r}).
\end{aligned} \tag{2.23}$$

Approximation of the exchange and correlation energy

The only unknown part is the exchange correlation energy E_{xc}. The basic idea is to apply exact exchange-correlation energies of the homogeneous electron gas as an approximation to the energies in inhomogeneous systems. The local density approximation (LDA) implements this by assuming an exchange-correlation functional $E_{xc}[n]$ of the form

$$E_{xc}[n] = \int n(r)\epsilon_{xc}(n(r))\,dr, \tag{2.24}$$

where ϵ_{xc} is a *function* of the density $n(r)$. To obtain an explicit form of ϵ_{xc}, one separates exchange (E_x) and correlation (E_c) contributions as

$$E_{xc} = E_x + E_c \tag{2.25}$$

and similarly $\epsilon_{xc} = \epsilon_x + \epsilon_c$ for the corresponding energy densities. The exchange energy E_x is defined as the Fock integral applied to the Kohn-Sham (KS) orbitals:

$$E_x[n] = \langle \Phi^{KS} | \hat{V}_{ee} | \Phi^{KS} \rangle - E_H[n], \tag{2.26}$$

where $|\Phi^{KS}\rangle$ is the Slater determinant of the occupied KS orbitals. This expression can be evaluated for the homogeneous electron gas, where the KS orbitals are plane waves (see, e.g., [118]). The resulting exchange energy density is

$$\epsilon_x(n) = -\frac{3}{4\pi}(3\pi^2 n)^{1/3} = -\frac{3}{4\pi}\frac{(9\pi/4)^{1/3}}{r_s} \tag{2.27}$$

where r_s is the Wigner Seitz radius - the radius of a sphere containing one electron on average:

$$n = \frac{3}{4\pi r_s^3}.$$ (2.28)

Analytical expressions for ϵ_c are known for the homogeneous electron gas in the limits of high and low densities. The high-density limit is the limit of weak interactions, in which

$$\epsilon_c(n) = c_0 \log r_s - c_1 + c_2 r_s + \log r_s - c_3 r_s + \dots$$ (2.29)

and the constants c_i are obtained from many-body perturbation theory [118]. In the low-density, i.e. strong coupling limit, there comparison to the electrostatic zero-point vibrational energies of a Wigner crystal [118] yields the analytical expression

$$\epsilon_c(n) = -\frac{d_0}{r_s} + \frac{d_1}{r_s^{3/2} + \dots}$$ (2.30)

and the constants d_i. An expression encompassing both limits, Eq. (2.29) and Eq. (2.30), is

$$\epsilon_c(n) = -2c_0(1 + \alpha_1 r_s) \log \left[1 + \frac{1}{2c_0(\beta_1 r_s^{1/2} + \beta_2 r_s + \beta_3 r_s^{3/2} + \beta_4 r_s^2)} \right],$$ (2.31)

where $\beta_1 = \frac{1}{2c_0} \exp(-\frac{c_1}{2c_0})$, $\beta_2 = 2c_0\beta_1^2$. The remaining coefficients α_1, β_3 and β_4 are obtained by fitting Eq. (2.31) to the quantum Monte Carlo correlation energies found by Ceperley and Alder (see, e.g., [118] and references therein).

These formulas can be illustrated by introducing the exchange-correlation hole $n_{xc}(r, r')$, which describes the depletion of density at r', in the presence of an electron at r. With the concept of coupling constant integration $n_{xc}(r, r')$ can directly be related to the functional $E_{xc}[n]$: Eq. (2.10) is generalized by introducing the coupling constant $\lambda \in [0, 1]$,

$$F_\lambda[n] = \min_{\Psi \to n} \langle \Psi_n^\lambda | \hat{T} + \hat{V}_{ee} | \Psi_n^\lambda \rangle,$$ (2.32)

and defining $|\Psi_n^\lambda\rangle$ as the N-electron state which minimizes $\hat{T} + \lambda \hat{V}_{ee}$ under the constraint of yielding the density $n(\mathbf{r})$. Varying λ from 0 to 1 corresponds to going from the non-interacting Kohn-Sham system with potential $v_{eff}(r)$ to the interacting electron system with the true external potential $v_{ext}(r)$. By assuming an adiabatic connection between $|\Psi_n^1\rangle$ and $|\Psi_n^0\rangle$, it can be shown that [118]

$$E_{xc}[n] = \int_0^1 d\lambda \langle \Psi_n^\lambda | \hat{V}_{ee} | \Psi_n^\lambda \rangle - E_H[n].$$ (2.33)

Using the *conditional* probability $n_2(\mathbf{r}, \mathbf{r}')$ of finding an electron in $d^3 r'$ given there is one in

d^3r, one finds [118]

$$\langle\Psi_n^\lambda|\hat{V}_{\text{ee}}|\Psi_n^\lambda\rangle = \frac{1}{2}\int\,d^3r\,d^3r'\,\frac{n(\mathbf{r})\,n_2(\mathbf{r},\mathbf{r}')}{|\mathbf{r}-\mathbf{r}'|}. \tag{2.34}$$

Now $n_2(,\mathbf{r}')$ can be decomposed for any $|\Psi_n^\lambda\rangle$ into the contribution from the one-electron density $n(\mathbf{r}')$ and the exchange correlation hole $n_{\text{xc}}^\lambda(\mathbf{r},\mathbf{r}')$ [118]:

$$n_2(\mathbf{r},\mathbf{r}') = n(\mathbf{r}') + n_{\text{xc}}^\lambda(\mathbf{r},\mathbf{r}'). \tag{2.35}$$

Using the definition of the Hartree energy and Eq. (2.33), one finds that E_{xc} is determined by the coupling-constant averaged exchange correlation hole $\bar{n}_{\text{xc}}(\mathbf{r},\mathbf{r}') = \int_0^1\,d\lambda\,n_{\text{xc}}^\lambda(\mathbf{r},\mathbf{r}')$:

$$E_{\text{xc}}[n] = \frac{1}{2}\int\,d^3r\,d^3r'\,\frac{n(\mathbf{r})\,\bar{n}_{\text{xc}}(\mathbf{r},\mathbf{r}')}{|\mathbf{r}-\mathbf{r}'|}. \tag{2.36}$$

Hence an accurate approximation to the exchange-correlation functional $E_{\text{xc}}[n]$ is equivalent to having an accurate description of $\bar{n}_{\text{xc}}(\mathbf{r},\mathbf{r}')$.

By definition [118] of n_2 we have $\int\,d^3r'\,n_2(\mathbf{r},\mathbf{r}') = N-1$ and hence

$$\int\,d^3r'\,n_{\text{xc}}^\lambda(\mathbf{r},\mathbf{r}') = -1. \tag{2.37}$$

In analogy to the exchange-correlation energy in Eq. (2.25) and Eq. (2.26), $n_{\text{xc}}^\lambda(\mathbf{r},\mathbf{r}') = n_{\text{x}}(\mathbf{r},\mathbf{r}') + n_{\text{c}}^\lambda(\mathbf{r},\mathbf{r}')$ can be decomposed into the exchange hole $n_{\text{x}}(,\mathbf{r}')$ and the correlation hole $n_{\text{c}}^\lambda(\mathbf{r},\mathbf{r}')$. As the exchange energy is defined as the Fock integral of the KS orbitals, (cf. Eq. (2.26)), one can show [118] that

$$n_{\text{x}}(\mathbf{r},\mathbf{r}') \leq 0 \tag{2.38}$$

in all space and

$$\int\,d^3r'\,n_{\text{x}}(\mathbf{r},\mathbf{r}') = -1. \tag{2.39}$$

The combination of Eq. (2.37) and Eq. (2.39) immediately implies

$$\int\,d^3r'\,n_{\text{c}}(\mathbf{r},\mathbf{r}') = 0. \tag{2.40}$$

In spin polarized DFT calculations, four matrix elements of the spin density matrix $\tilde{n}_{\alpha\beta}(\mathbf{r})$ are in principle required at each point r to describe the electronic ground state properly. However, if noncollinear magnetic effects are negligible, $\tilde{n}_{\alpha\beta}(\mathbf{r})$ can be assumed to be diagonal in all space and only the two spin densities $n_\alpha(\mathbf{r}) = \tilde{n}_{\alpha\alpha}(\mathbf{r})$ for $\alpha = \uparrow,\downarrow$ are left as basic variables.

The generalization of LDA to include spin densities, called local spin density approximation

(LSDA), can be written out for the collinear case as

$$E_{\text{xc}}[n] = \int d^3 r \, n(\mathbf{r}) \epsilon_{\text{xc}}(n_\uparrow(\mathbf{r}), n_\downarrow(\mathbf{r})). \tag{2.41}$$

This LSDA functional can be obtained from the LDA functional using spin scaling relations for kinetic and exchange terms as well as RPA based interpolation of the correlation energy. Widely used parametrisations can e.g. be found in [118].

Although these local approximations are exact only for the homogeneous electron gas, L(S)DA gives surprisingly accurate results even for systems, where the density varies strongly on the scale of the Fermi wavelength or the Thomas-Fermi screening length. This success of L(S)DA is due to the fact that it is derived from a real physical system. Among many other correct features, the LDA exchange correlation hole respects the sum rules of Eq. (2.39) and Eq. (2.40) as well as the negativity condition for the exchange hole, Eq. (2.38).

These features turned out to be of crucial importance for the construction of semilocal generalizations of LSDA. The first exchange correlation functionals including density gradients ∇n - the so-called gradient expansion approximations (GEA) - were less accurate than LDA due to unphysical properties of $n_{\text{xc}}(r, r+u)$ at large u [118]. There n_{x}^{GEA} shows undamped $\cos(2k_f u)$ oscillations, thereby it violates the negativity condition and fulfills the sum rule in Eq. (2.39) only with an additional convergence factor. Furthermore $n_{\text{c}}^{\text{GEA}}$ does not integrate to zero as required by Eq. (2.40) due to a positive u^{-4} tail at large u.

Only at small u the GEA models describe the exchange correlation hole much better than the LDA. Perdew, Wang, Becke *et al.* (see, e.g., [118]) succeeded in constructing functionals that combine the desirable features of the LDA with the more realistic exchange-correlation-hole from the GEA at small u. This class of semilocal functionals, called generalized gradient approximations (GGA), is now widely applied from solid-state physics to chemistry. The mostly used functional of this type is the PBE functional proposed by Perdew, Burke, and Ernzerhoff [116]. A detailed description of how to construct the PBE functional is given in Ref. [118]. All semilocal calculations in this thesis were performed with the PBE functional.

Hybrid density functionals

The third generation of density functionals are called hybrid density functionals. Hybrid density functionals are orbital dependent functionals, where the exchange potential is described in part through the nonlocal Fock exchange potential and in part through a semilocal expression [15]. With respect to semilocal functionals, hybrid functionals improve various physical properties like ionization potentials, electron affinities, and lattice constants. However, their ability to improve the description of band gaps of semiconductors has often been one major motivation to use them. A variety of hybrid functionals are currently in use in chemistry. For the description of solid-state systems, the most used hybrid functionals are the so called PBE0 functional and the HSE functional. The generalized form of the PBE0 functional is also called

PBEh(α), where a fraction α of PBE exchange is replaced by nonlocal Fock exchange.

$$E_{\text{x}}^{\text{PBEh}}(\alpha) = \alpha E_{\text{x}}^{\text{exact}} + (1 - \alpha) E_{\text{x}}^{\text{PBE}} \tag{2.42}$$

For $\alpha = 0.25$, the PBE0 functional is recovered.

The exchange energy of the HSE functional is given by

$$E_{\text{x}}^{\text{HSE}}(\alpha, \omega) = \alpha E_{\text{x}}^{\text{exact,SR}}(\omega) + (1 - \alpha) E_{\text{x}}^{\text{PBE,SR}}(\omega) + E_{\text{x}}^{\text{PBE,LR}}(\omega) \tag{2.43}$$

where $\alpha = 0.25$ and $\omega = 0.106$ bohr^{-1} [67, 68]. $E_{\text{x}}^{\text{HSE}}$ is a generalization of $E_{\text{x}}^{\text{PBE0}}$. By setting $\omega \to 0$ and $\alpha = 0.25$, it transforms back to $E_{\text{x}}^{\text{PBE0}}$. In the limit $\omega \to \infty$, Eq. (2.43) becomes $E_{\text{x}}^{\text{PBE}}$. For $\alpha \to 0$, both functionals in Eq. (2.42) and Eq. (2.43) become $E_{\text{x}}^{\text{PBE}}$.

The separation between short-range and long-range exchange is achieved through the use of a screened exchange kernel given by erfc($\omega r / r$), where the parameter ω corresponds to an inverse screening length and defines the extent of the exchange kernel in real space.

Quantities derived from total energies, including both ionization potentials of molecules and charge transition levels of defects, are found to be very similar in PBE0 and in HSE [82].

The nonlocal Fock exchange energy E_{x} can be written in real space

$$E_{\text{x}} = -\frac{e^2}{2} \sum_{\mathbf{k}n, \mathbf{q}m} w_{\mathbf{k}} f_{\mathbf{k}n} w_{\mathbf{q}} f_{\mathbf{q}m} \int \int d^3\mathbf{r} d^3\mathbf{r}' \frac{\phi_{\mathbf{k}n}^*(r)\phi_{\mathbf{q}m}(r)\phi_{\mathbf{q}m}^*(\mathbf{r}')\phi_{\mathbf{k}n}(\mathbf{r}')}{|\mathbf{r} - \mathbf{r}'|} \tag{2.44}$$

where $\{\phi_{\mathbf{k}n}(\mathbf{r})\}$ are the one-electron Bloch states with possibly fractional occupation $\{f_{\mathbf{k}n}\}$. The sums over $\mathbf{k}$ and $\mathbf{q}$ need to be performed over all $\mathbf{k}$-points chosen to sample the Brillouin zone. The sums over m and n are performed over all bands at these $\mathbf{k}$ points. $w_{\mathbf{k}}$ is the $\mathbf{k}$-point weight.

The corresponding Fock exchange potential is given by

$$\begin{aligned} V_{\text{x}}(\mathbf{r}, \mathbf{r}') &= -e^2 \sum_{\mathbf{q}m} w_{\mathbf{q}} f_{\mathbf{q}m} \frac{\phi_{\mathbf{q}m}^*(\mathbf{r}')\phi_{\mathbf{q}m}(\mathbf{r})}{|\mathbf{r} - \mathbf{r}'|} \\ &= -e^2 \sum_{\mathbf{q}m} w_{\mathbf{q}} f_{\mathbf{q}m} e^{-i\mathbf{q}\mathbf{r}'} \frac{u_{\mathbf{q}m}^*(\mathbf{r}') u_{\mathbf{q}m}(\mathbf{r})}{|\mathbf{r} - \mathbf{r}'|} e^{i\mathbf{q}\mathbf{r}} \end{aligned} \tag{2.45}$$

where $u_{\mathbf{q}m}(\mathbf{r})$ is the periodic part of the Bloch state, $\phi_{\mathbf{q}m}(\mathbf{r})$, at $\mathbf{k}$-point $\mathbf{q}$ with band index m.

2.2 Implementation

Plane-Waves

To calculate the total energy of solids, a plane-wave (PW) expansion of the Kohn-Sham wave function is very useful, as it takes advantage of the periodicity of the crystal. The wave function can be expanded in a plane-waves basis set. The plane waves with wave vector $\mathbf{k}$ have the form $\phi_{\mathbf{k}} \propto e^{-i\mathbf{k}\cdot\mathbf{r}}$. First, the wave function is expressed in its Bloch form [10]

$$\Psi_{n\mathbf{k}}(\mathbf{r}) = e^{i\mathbf{k}\cdot\mathbf{r}} u_{n\mathbf{k}}(\mathbf{r}). \tag{2.46}$$

The periodic Bloch function $u_{n\mathbf{k}}(\mathbf{r})$ are then expanded in plane waves:

$$u_{n\mathbf{k}}(\mathbf{r}) = \frac{1}{\Omega} \sum_{\mathbf{G}} c_{n\mathbf{k}} e^{i\mathbf{G}\cdot\mathbf{r}}. \tag{2.47}$$

The Kohn-Sham orbitals in the plane-wave expansion become

$$\Psi_{n\mathbf{k}} = \frac{1}{\Omega} \sum_{\mathbf{G}} c_n(\mathbf{k}+\mathbf{G}) e^{i(\mathbf{k}+\mathbf{G})\cdot\mathbf{r}}, \tag{2.48}$$

where the sum extends over the reciprocal lattice vectors $\mathbf{G}$ and Ω is the volume of the unit cell. $c_{n\mathbf{k}} = c_n(\mathbf{k}+\mathbf{G})$ are complex coefficients of the PW basis set. In this way, the electronic structure is characterized by a band index n and a wave vector $\mathbf{k}$ restricted to the first Brillouin zone. Since the Kohn-Sham potential converges rapidly with increasing modulus of $\mathbf{G}$, only $\mathbf{G}$ vectors with a kinetic energy smaller than a given cutoff have to be used. This allows one to control the wave function basis with a single parameter E_{cut}.

For finite systems, such as atoms and molecules, plane-waves can also be used in a super-cell approach. The supercell has to be sufficiently large, so that interactions with periodic images are negligible. For charged supercell calculations, the Coulomb energy diverges in this approach. To overcome this problem, one can compensate the charge with a uniform background charge that neutralizes the supercell.

Fock exchange in reciprocal space

Using Eq. (2.47), Eq. (2.45) can be rewritten in its plane wave expansion

$$V_{\text{x}}(\mathbf{r}, \mathbf{r}') = \sum_{\mathbf{k}} \sum_{\mathbf{G}\mathbf{G}'} e^{i(\mathbf{k}+\mathbf{G})\cdot\mathbf{r}} V_{\mathbf{k}}(\mathbf{G}, \mathbf{G}') e^{-i(\mathbf{k}+\mathbf{G}')\cdot\mathbf{r}'}, \tag{2.49}$$

where

$$V_{\mathbf{k}}(\mathbf{G}, \mathbf{G}') = \langle \mathbf{k} + \mathbf{G} | \hat{V}_{\mathrm{x}} | \mathbf{k} + \mathbf{G}' \rangle$$
$$= -\frac{4\pi e^2}{\Omega} \sum_{m\mathbf{q}} w_{\mathbf{q}} f_{\mathbf{q}m} \sum_{\mathbf{G}''} \frac{c_{\mathbf{q}m}^*(\mathbf{G}' - \mathbf{G}'') c_{\mathbf{q}m}(\mathbf{G} - \mathbf{G}'')}{|\mathbf{k} - \mathbf{q} + \mathbf{G}''|^2} \tag{2.50}$$

is the representation of the Fock exchange potential in reciprocal space [63].

For calculations at the Γ point, Eq. (2.50) becomes

$$V_{\mathbf{k}}(\mathbf{G}, \mathbf{G}') = \langle \mathbf{G} | \hat{V}_{\mathrm{x}} | \mathbf{G}' \rangle$$
$$= -\frac{4\pi e^2}{\Omega} \sum_{m} \sum_{\mathbf{G}''} \frac{c_m^*(\mathbf{G}' - \mathbf{G}'') c_m(\mathbf{G} - \mathbf{G}'')}{|\mathbf{G}''|^2} \tag{2.51}$$

At $\mathbf{G}'' = 0$, Eq. (2.51) has a divergent term, which can be replaced by a finite term which ensures the convergence of the sum [63, 28].

Pseudopotentials

When plane-waves are used as basis functions, it become necessary to use them in a pseudopotential approach. The electrons of an atom can be separated in core and valence electrons. The core electrons are strong bound to the nucleus and are usually not affected by chemical reactions. The valence electrons are more weakly bound and responsible for forming chemical bonds to other atoms. The idea of the pseudopotenial approach, is to reduce the complexity of the system by treating the core electrons in an average potential together with the nucleus of the atom. Thus, the atom reduces to an ionic core, that interacts with the valence electrons. This leads to a dramatic reduction of the number of electrons in the system, which speeds up the calculations or enables the treatment of bigger systems. Valence states are smoother than core states and need therefore less basis functions for a proper description. Usually, the pseudo valence states are nodeless, which allows a further reduction of the basis set size.

To construct an *ab initio* pseudopotential, one solves the radial Schrödinger equation of an atom with nuclear charge Z in a chosen electronic configuration:

$$\left[-\frac{1}{2} \frac{d^2}{dr^2} + \frac{l(l+1)}{2r^2} + v_{\mathrm{KS}}^{\mathrm{AE}}[n^{AE}](r) \right] R_{nl}^{\mathrm{AE}} = \epsilon_{nl}^{\mathrm{AE}} r R_{nl}^{\mathrm{AE}}. \tag{2.52}$$

The Kohn-Sham potential for the spherical atom can be written as

$$v_{\mathrm{KS}}^{\mathrm{AE}}[n^{AE}](r) = -\frac{Z}{r} + v_{\mathrm{ee}}[n^{AE}](r) + v_{\mathrm{xc}}[n^{AE}](r), \tag{2.53}$$

where relativistic effects are not considered and PP and AE stand for pseudopotential and all-electron, respectively.

In the next step, the pseudo wave functions are constructed. The pseudo wave functions are

forced to coincide with the all-electron valence wave functions beyond a certain distance r_c.

$$R_l^{\text{PP}}(r) = R_{nl}^{\text{AE}}(r), \quad \text{for} \quad r > r_c \tag{2.54}$$

where $R(r)$ is the radial part of the wavefunction. The subscript index labels the angular momentum. The norm of the pseudo wave functions is forced to be equal to the norm of the respective all-electron valence wave functions [65]:

$$\int_0^{r_c} dr |R_l^{\text{PP}}(r)|^2 r^2 = \int_0^{r_c} dr |R_{nl}^{\text{AE}}(r)|^2 r^2. \tag{2.55}$$

The cut-off radius, r_c depends on the angular momentum of the wave function. The pseudo energy eigenvalues should match the all-electron eigenvalues $\epsilon_l^{\text{PP}} = \epsilon_{nl}^{\text{AE}}$.

Troullier-Martins pseudopotentials

There exist various methods for the parametrization of the pseudo wave function. One of the first was introduced by Hamann [65]. Troullier and Martins proposed a different scheme [142]. For the wave function, they use the following ansatz:

$$R_l^{\text{PP}}(r) = \begin{cases} R_{nl}^{\text{AE}} & r > r_c \\ r^l e^{p(r)} & r < r_c, \end{cases} \tag{2.56}$$

where

$$p(r) = c_0 + c_2 r^2 + c_4 r^4 + c_6 r^6 + c_8 r^8 + c_{10} r^{10}, \tag{2.57}$$

is a polynomial function. The coefficients of the polynomial are adjusted by imposing norm conservation, the continuity of the wave function, and of its first four derivatives at $r = r_c$, and that the screened pseudopotential has zero curvature at the origin.

With the pseudo wave function and the valence electron density, one inverts the radial Schrödinger equation and gets the pseudopotential

$$w_{l,\text{scr}}(r) = \epsilon_l^{\text{PP}} - \frac{l(l+1)}{2r^2} + \frac{1}{2r R_l^{\text{PP}}(r)} \frac{d^2}{dr^2} [r R_l^{\text{PP}}(r)] \tag{2.58}$$

The resulting pseudopotential, $w_{l,\text{scr}}$, still contains screening effects due to valence electrons. These are subtracted out as follows:

$$w_l = w_{l,\text{scr}}(r) - v_{\text{ee}}[n^{\text{PP}}](r) - v_{\text{xc}}[n^{\text{PP}}](r). \tag{2.59}$$

Non-linear core-correction

For some elements, core and valence electron densities overlap. Because of the non linearity of the exchange correlation potential

$$
\begin{aligned}
v_{\mathrm{xc}}[n^{\mathrm{AE}}](r) &\equiv v_{\mathrm{xc}}[n^{\mathrm{core}} + n^{\mathrm{PP}}](r) \\
&\neq v_{\mathrm{xc}}[n^{\mathrm{core}}](r) + v_{\mathrm{xc}}[n^{\mathrm{PP}}](r)
\end{aligned}
\tag{2.60}
$$

the pseudopotential scheme, which assumes a strict separation of core and valence states has to be corrected. This can be done by introducing an additional partial core density $\tilde{n}^{\mathrm{core}}$, which replaces the true core density [93, 53]. Thus, the pseudopotential becomes

$$
w_l = w_{l,\mathrm{scr}}(r) - v_{\mathrm{ee}}[n^{\mathrm{PP}}](r) - v_{\mathrm{xc}}[\tilde{n}^{\mathrm{core}} + n^{\mathrm{PP}}](r).
\tag{2.61}
$$

Flow

Due to the functional dependence on the density $n(\mathbf{r})$, the Kohn-Sham equations (Eq. (2.21)) are a set of non-linear coupled equations. The standard procedure to solve this equation system is through iteration until selfconsistency is achieved. A schematic flow chart of this scheme is given in Fig. 2.1. Usually the staring charge density $n_0(\mathbf{r})$ is constructed by a superposition of atomic orbitals, but in principle a complete random configuration also leads to a selfconsistent wave function. In problematic cases, a random charge density can be necessary to find the real ground state of the system.

In the pseudopotential approximation, the external potential v_{ext}, which is part of the Kohn-Sham potential given in Eq. (2.23), is simply given by a sum over all atoms α in the system. This can be written as

$$
w(\mathbf{r}, \mathbf{r}') = \sum_{j,\alpha} = w_\alpha(\mathbf{r} - \mathbf{R}_j - \mathbf{r}_\alpha, \mathbf{r}' - \mathbf{R}_j - \mathbf{r}_\alpha),
\tag{2.62}
$$

where $\mathbf{r}_\alpha$ is the position of atom α in the unit cell, and $\mathbf{R}_j$ are the lattice vectors. The pseudopotential $w(\mathbf{r}, \mathbf{r}')$ appears in a nonlocal form.

In this work, normconserving Trouiller-Martins pseudopotentials were used [142]. For Ge, we also considered a non-linear core-correction in the pseudopotential. A wave function cutoff of 70 Ry was used. For solving the Schrödinger equation, we used the implementation provided in the Quantum-ESPRESSO package [56], and in the CPMD package [9].

Maximally localized Wannier functions

Kohn-Sham orbitals are localized in energy, but delocalized in space. The charged center of maximally localized Wannier functions (MLWF) provides a kind of classical correspondence for the location of an electron in a quantum-mechanical insulator [98]. The knowledge of

$$n_0(\mathbf{r})$$

$$v_{\text{KS}}(\mathbf{r})$$

$$H_{\text{KS}}\phi_i(\mathbf{r}) = \epsilon_i \phi_i(\mathbf{r})$$

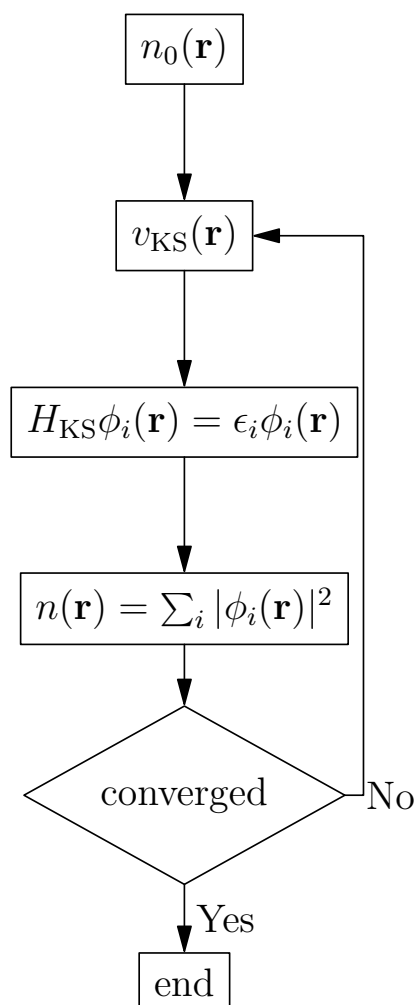$$n(\mathbf{r}) = \sum_i |\phi_i(\mathbf{r})|^2$$

converged

No

Yes

end

Figure 2.1 – Flow chart diagram for the iterative procedure to solve the Kohn-Sham equations.

the position of Wannier function centers (WFCs) and their spread can capture most of the chemistry in the system. This can be used to find bond definitions beyond the pure geometric description. A brief description of Wannier functions is given.

The most general operation that transforms Bloch orbitals $|\Psi_{m\mathbf{k}}\rangle$ into Wannier functions $|w_{n\mathbf{R}}\rangle$ is given by

$$|w_{n\mathbf{R}}\rangle = \frac{V}{(2\pi)^3} \int_{\text{BZ}} \left[\sum_{m=1}^{N} U_{mn}^{(k)} |\psi_{m\mathbf{k}}\rangle \right] e^{-i\mathbf{k}\cdot\mathbf{R}} d\mathbf{k} \qquad (2.63)$$

where $\mathbf{U}^{(\mathbf{k})}$ is a unitary matrix of dimension N [98].

Maximally localized Wannier functions are defined as the Wannier functions with the smallest spread. The goal is to find a set of matrices $\mathbf{U}^{(k)}$, one per $\mathbf{k}$-point, that minimize the total spread

$$\Omega = \sum_n \left[\langle \mathbf{O}_n | r^2 | \mathbf{O}_n \rangle - \langle \mathbf{O}_n | \mathbf{r} | \mathbf{O}_n \rangle^2 \right] = \sum_n \left[\langle r^2 \rangle_n - \tilde{\mathbf{r}}_n^2 \right] \qquad (2.64)$$

of the Wannier functions $|\mathbf{O}_n\rangle$ in real space, where $\langle r^2 \rangle_n$ and $\langle \mathbf{r} \rangle_n$ are the expectation values of $\langle \mathbf{O}_n | r^2 | \mathbf{O}_n \rangle$, and $\langle \mathbf{O}_n | \mathbf{r} | \mathbf{O}_n \rangle$, respectively [98].

For our purpose, the Brillouin was sampled only at Γ-point. This reduces the problem, and only one matrix U has to be found.

The expectation value of the Hamiltonian for a Wannier function can obtained in the following way

$$
\begin{aligned}
\langle w_n | H | w_n \rangle &= \langle w_n | \Psi_p \rangle \langle \Psi_p | H | \Psi_q \rangle \langle \Psi_q | w_n \rangle \\
&= \langle \Psi_p | w_n \rangle^* \langle \Psi_q | w_n \rangle \langle \Psi_p | H | \Psi_q \rangle \\
&= \langle \Psi_p | w_n \rangle \langle \Psi_p | w_n \rangle \epsilon_p \\
&= \left[\langle \Psi_p | \sum_{m=1}^{N} U_{mn} | \Psi_m \rangle \right]^2 \epsilon_p \\
&= \sum_{m=1}^{N} U_{mn}^2 \epsilon_m
\end{aligned}
\qquad (2.65)
$$

To perform the rotation from Bloch to Wannier functions, we used the implementation in the wannier90 code [103].

2.3 Defect Formation Energies

Native defects due to imperfect growth conditions are playing an important role in semiconductor materials. While experimental methods for the identification and characterization of defects often probe only specific defect properties, as accessible by the respective spectro-

scopic method, theoretical studies of defects play an important role to complete the picture. The pivotal quantity is the defect formation energy E_f, from which one can calculate the defect concentrations and the electrical and optical transition levels [160, 146, 87].

Definition

The defect formation energy of an impurity X in the charge state q is defined as

$$E_f[X^q] = E_{tot}[X^q] - E_{tot}[\text{bulk}] - \sum_i n_i \mu_i + q[E_F + E_v + \Delta V]. \tag{2.66}$$

Where $E_{tot}[X^q]$ is the total energy of a supercell with an impurity X in the charge state q, $E_{tot}[\text{bulk}]$ is the corresponding total energy of the supercell without the impurity, n_i is the number of atoms i which is added or removed form the bulk system to form the defect, and μ_i is the chemical potential of atom type n_i. If the defect is charged ($q \neq 0$) the energy of adding ($q > 0$) or removing ($q < 0$) q electrons from the Fermi level (E_F) to the defect has to be added. The Fermi level is usually located between the valence band maximum and the conduction band minimum E_c, $E_v < E_F < E_c$. Therefore, the Fermi level is usually defined with respect to the valence band maximum ($E_v = 0$) of the bulk supercell. ΔV is needed to align the valence bands in the bulk and defected supercells. This is needed because the reference levels in the bulk and defected supercells are not equal. Therefore, one inspects the electrostatic potential far away from the defect and aligns it with the electrostatic potential in bulk. The difference is given by ΔV [146].

Chemical potential

The growth conditions are reflected in the chemical potential μ_i of the atoms removed ($n_i = -1$) or added ($n_i = +1$) to the host crystal when the defect is formed. For the chemical potential, one can give a minimal and maximal value. For example, in an extremely Ge-rich environment,

$$\mu_{Ge} = \mu_{Ge}[\text{bulk}] = \frac{1}{2} E_{tot}[\text{Ge}] \tag{2.67}$$

where $E_{tot}[\text{Ge}]$ is the total energy of a two-atom primitive Ge cell. For higher values of μ_{Ge} only bulk germanium would be grown. The maximum value for the O chemical potential can similarly be defined with the O_2 molecule as reference system. For the lower bounds of μ_{Ge} and μ_O, one can use the total energy of the native Ge oxide, GeO_2:

$$\mu_{Ge} + 2\mu_O = \frac{1}{N} E_{tot}[GeO_2], \tag{2.68}$$

where $E_{tot}[GeO_2]$ is the total energy of a bulk GeO_2 supercell with N fragments of GeO_2. The lower limit of μ_{Ge} is than given by the upper limit of μ_O, and vice versa.

Most defects and impurities exist in different charge states. Thus, defect formation energies have to be evaluated for all possible charge states. The stable charge state is then the one which has the lowest formation energy for a given electron chemical potential.

Charged defects

To estimate the total energy of a charged defect subject to periodic boundary conditions, one has to remove spurious electrostatic interactions between the defect and its periodic images and between the defect and the neutralizing background.

Makov and Payne proposed a method to correct the electrostatic energy in charged supercells. Essentially, it corresponds to the Madelung energy of a lattice of screened point charges in a dielectric environment:

$$E = E_0 - \frac{q^2 \alpha}{2L} + \frac{2\pi q Q}{3L^3} + O(L^{-5}) \tag{2.69}$$

where E_0 is the desired total energy of the isolated system, α is the Madelung constant, L is the length of the cubic simulation cell, and Q is the quadrupole moment of the defect charge distribution. The first term corrects the interaction between screened monopoles, whereas the second term corrects the defect charge distribution interacting with the background charge. The Makov-Payne correction works well for atomic or molecular systems. For defects in solids, it has been found to often overestimate the required correction [87]. However, when the charge is very localized the first-order Makov-Payne term has been found to give very reliable corrections [83].

3 Crystalline models of GeO$_x$

Silicon and germanium are elements in the carbon group of the periodic table. All elements in this group (carbon (C), silicon (Si), germanium (Ge), tin (Sn), and lead (Pb)) are chemically similar. With increasing mass the reactivity of the elements in this group decreases. Silicon and germanium crystallize in the diamond cubic crystal structure. Unlike silicon, germanium does not exist in its pure form on earth. Both elements like to form oxides. Silicon dioxide is one of the most common compounds on earth. It exists in crystalline and amorphous phases. Its natural crystalline structure is α-quartz. Germanium dioxide also forms crystalline and amorphous phases. Unlike silicon dioxide it is soluble in water. In contact with pure germanium, germanium monoxide is formed.

This chapter is organized as follows. First, we compare the stability of silicon and germanium in its diamond cubic crystal structure. Therefore, we optimize the lattice constant of both materials within the PBE functional and the PBE0 functional. With the optimized total energy, we calculate the cohesive energy for both semiconductors and compare it to experimental values. Second, we study the stability of silicon and germanium dioxide in different crystal phases. Therefore, we fully optimize the primitive cells of the α-quartz, α-cristobalite, β-cristobalite, and rutile structures for both SiO$_2$ and GeO$_2$. The total energies are given with respect to the oxygen molecule O$_2$ and to the corresponding bulk energies of silicon and germanium, respectively. Third, we study the energetics of substoichiometric SiO$_x$ and GeO$_x$. We determine the energetics of these oxides in terms of penalty energies which describe deviations with respect to a bond-energy picture [64, 22]. For this scope, we use crystalline models of substoichiometric oxides and address their energetic, structural, and electronic properties for varying oxidation state. For Ge, the calculated penalty energies are found to be significantly lower than for Si, implying higher stability of the substoichiometric oxide phase. This result supports a higher concentration and a more extended distribution of the substoichiometric phase at Ge/GeO$_2$ interfaces compared to Si/SiO$_2$ interfaces. In the last part of this chapter, we investigate the thermodynamics of oxygen vacancies in Ge-GeO$_2$-HfO$_2$ stacks. We find the oxygen vacancies to be most stable in the germanium oxide layer, thus supporting the formation of a GeO$_x$ transition layer in accord with experimental observations.
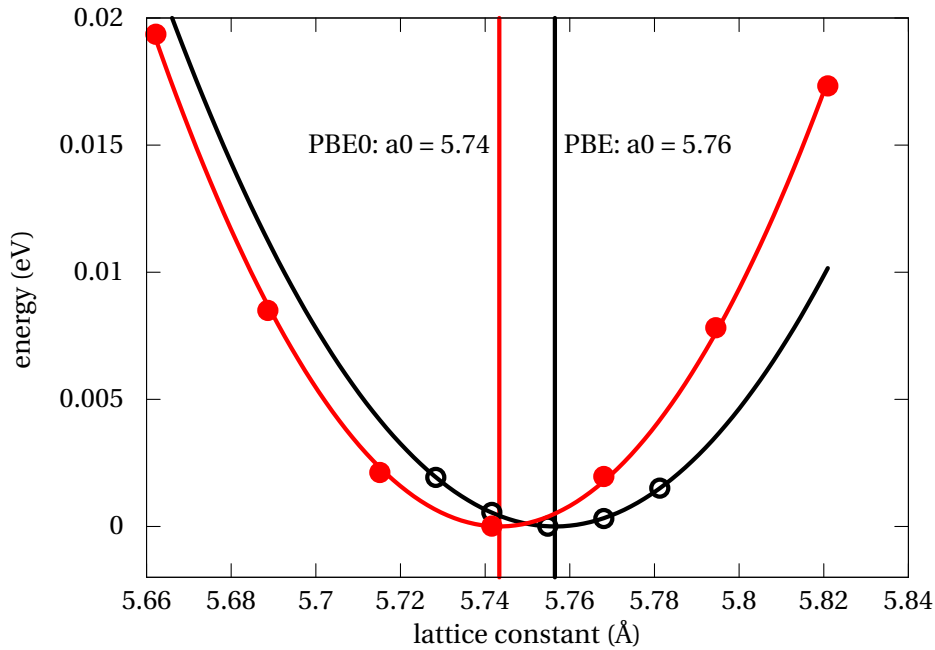
Figure 3.1 – Murnaghan equation of state for bulk germanim within the PBE functional and with the PBE0 functional.

This chapter contains the contents of previously published papers [16, 32].

3.1 Stability of germanium and of its native oxide

In this section, we discuss the stability of bulk silicon and germanium, as well as of their main crystalline oxides. For the pure semiconductor, the cohesive energy will by used to quantify the energetics of the diamond solid phase. The formation energy of the oxides, is used to quantify the stability of the oxide. For the oxide, we consider different crystalline phases.

Stability of the semiconductor

In this part, we compare the cohesive energies of bulk silicon and germanium. First, we quantify the lattice constant for silicon and germanium in their bulk structure. Figure 3.1 shows the Murnaghan equation of state for germanium obtained within the semi-local PBE description and within the hybrid description provided by the PBE0 functional. The PBE0 lattice constant is only slightly smaller (5.74 Å) than the PBE lattice constant (5.76 Å). This small difference should be attributed to the use of the pseudopotential scheme. Indeed, a larger reduction is achieved in the hybrid functional calculation, when the $3d$ semi-core states are considered explicitly [74]. We included a non-linear core correction to account for the overlap between valence and core states. In the following, we will focus on the PBE description.

Table 3.1 – Calculated and experimental lattice constant as well as cohesive energies for bulk Si and Ge, respectively. Lattice constants are in Å. Energies are in eV. Experimental data are taken from [94].

	lattice constant		cohesive energy	
	PBE	expt.	PBE	expt.
Si	5.46	5.43	4.52	4.63
Ge	5.76	5.66	3.67	3.85

Table 3.2 – Stability of GeO$_2$ and SiO$_2$ in different crystalline structures evaluated with the PBE functional. As oxygen chemical potential, half of the total energy of the oxygen molecule O$_2$ in the gas phase is used. The Ge and Si chemical potentials are taken from their bulk structures.

	α-quartz	α-cristobalite	β-cristobalite	rutile
Si	8.33	8.42	8.14	7.75
Ge	4.84	4.83	4.87	4.83

The cohesive energy of a solid is the energy required to break the atoms of the solid into isolated atomic species, one can write

$$E_{\mathrm{coh}} = E(\mathrm{solid}) - \sum_i E_i(\mathrm{isolated}), \tag{3.1}$$

where i labels the different atoms that constitute the solid. Calculated values of the cohesive energy are compared with experimental results which can be obtained by measuring the latent heat of sublimation at various low temperatures, and extrapolating to zero Kelvin.

For the atomic calculations, the ground-state spin configurations was used. For silicon and germanium the spin ground-state has parallel spins for the two highest occupied electron states. These correspond to two $3p$ electrons for silicon, and to two $4p$ electrons for germanium. The energy associated with the bulk solid is evaluated at the PBE optimised lattice constant. For the atomic calculations, a supercell with a side 10 Å is used. This is sufficiently large, to estimate the atomic ground state energy within 1 meV. The calculated cohesive energies are presented in Table 3.1 together with experimental values from Ref. [94]. Both calculated cohesive energies are in good agreement with experimental values. For silicon, the energy required for breaking bonds is 20% larger than for germanium.

Stability of the oxide

Compared to the bulk semiconductor, the oxide is more complex. At the semiconductor/oxide interface, the oxide is in a amorphous phase. The amorphous phase is discussed in the next Chapter 4. Here, we discuss a set of crystalline phases of silicon dioxide and germanium

dioxide. Therefore, we calculate the formation energy (E_f) per GeO$_2$ unit required to form the semiconductor oxide from the bulk semiconductor and the oxygen molecule.

$$E_f = E_{oxide}/N - \mu(O_2) - \mu(semiconductor) \tag{3.2}$$

where N is the number of germanium atoms per unit cell, $\mu(O_2)$ is the oxygen chemical potential given by the total energy of the oxygen molecule in its ground state, and $\mu(semiconductor)$ indicates the chemical potential of silicon or germanium given by their bulk energies. To obtain the formation energy of silicon dioxide and germanium dioxide in their α-quartz, α-cristobalite, β-cristobalite, and rutile structures, we fully optimize their structures and determine their total energies. The formation energies are calculated and presented in Table 3.2. On average, E_f of silicon dioxide is ∼ 70% higher than their germanium dioxide counterpart, indicating a higher stability of silicon dioxide compared to germanium dioxide. Compared to silicon dioxide, E_f of germanium dioxide is almost independent of the studied phase. Even in the high-pressure rutile structure, where germanium atoms are sixfold coordinated and oxygen atoms are threefold coordinated, E_f is of equal stability as in the more common phases. This suggests that overcoordinated Ge and O atoms might form more easily in disordered phases. One can infer the semiconductor bond energy from the semiconductor cohesive energy and the oxide bond energy from E_f. The ratio between oxide bond and semiconductor bond energy is different for silicon (1.85) and germanium (1.30). This result suggests that the Si/SiO$_2$ interface is more abrupt than the corresponding Ge/GeO$_2$ interface.

3.2 Stability of substoichiometric GeO$_x$

Models

To describe substoichiometric Ge oxides, we used crystalline models following previous work for Si [64]. In these models, all the Ge atoms are fourfold coordinated but with a varying number of O nearest neighbors. The oxidation state of Ge varies between 0 (Ge^0) of bulk Ge and 4 (Ge^{+4}) of GeO$_2$. For a better comparison, we also considered the analogous structures for Si within our setup. The models were constructed from ideal β-cristobalite GeO$_2$, which has a diamond structure with an O atom in each Ge-Ge bond. The Ge-O-Ge angles were systematically enforced to be 180°. The unit cell of the Ge^{+4} oxidation state has thus cubic symmetry with a lattice constant determined by the Ge-O bond length. The Ge^{+3} structure was constructed by removing the O atom in the [1 1 1]-directed bonds and by allowing the formation of a Ge-Ge bond. The relaxed structure results from the optimization of two external parameters and one internal parameter. For the Ge^{+2} model, we additionally removed the O atom in the [$\bar{1}\,\bar{1}$ 1]-directed bonds. The resulting structure shows Ge-Ge zigzag chains in one lattice direction and Ge-O zigzag chains in the other. The structure depends on three internal parameters and one external parameter. The Ge^{+1} model has only one O atom in the [1 1 1]-directed bond. This structure has the same degrees of freedom as the Ge^{+3} structure. The degrees of freedom enabled in the structural relaxation were sufficient for allowing concurrent
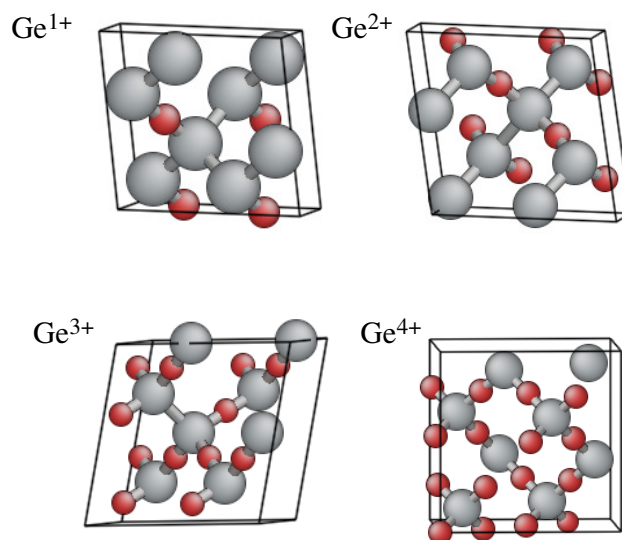
Figure 3.2 – Structurally relaxed substoichiometric oxide models.

optimization of the Ge-Ge and Ge-O bond lengths in each model.

The structurally optimized models are shown in Fig. 3.2. The resulting bond lengths are reported in Table 3.3 and illustrated in Figs. 3.3 and 3.4. The results for the bond lengths in the Si models are very similar to those found by Hamann [64]. For the Ge models, the relaxed Ge-O and Ge-Ge bonds are slightly longer but show similar trends. The Ge-O bonds monotonously elongate with decreasing oxidation state (cf. Fig. 3.3), reaching bond lengths for Ge^{+1} that are 3.5% longer than in the stoichiometric oxide. This result suggests that Ge-O bond lengths involving intermediate oxidation states at Ge/GeO$_2$ interface are longer than in bulk GeO$_2$, in analogy to observations for Si/SiO$_2$ interfaces [58, 57, 22]. The Ge-Ge bonds elongate for the

Table 3.3 – Bond lengths (in Å) for the substoichiometric Ge and Si oxide models generated in this work. Results for Si models obtained by Hamann [64] are also given.

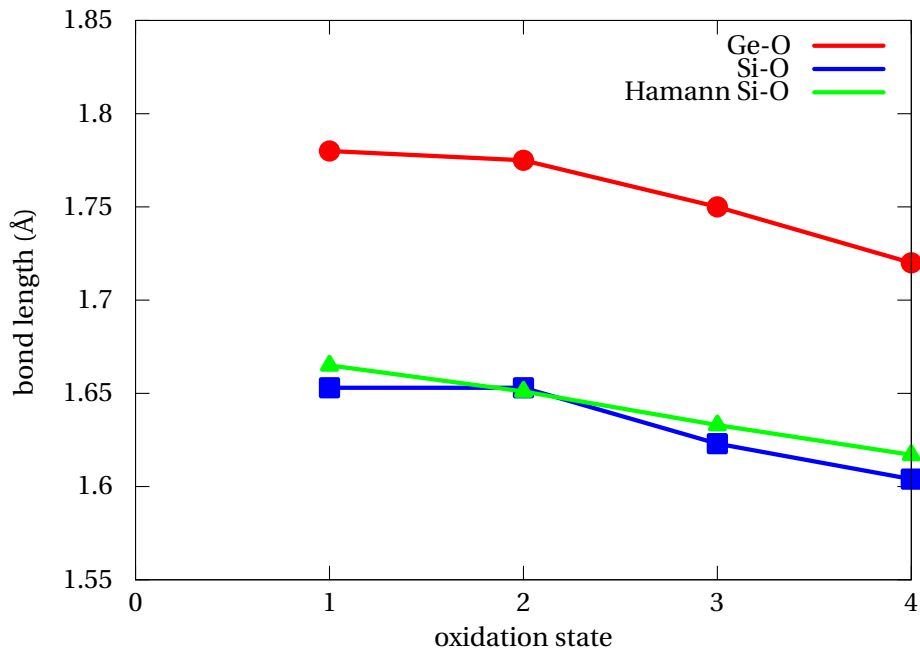| Model	Ge		Si		Hamann	
	Ge-Ge	Ge-O	Si-Si	Si-O	Si-Si	Si-O
0	2.500		2.366		2.367	
+1	2.550	1.780	2.381	1.663	2.416	1.665
+2	2.575	1.775	2.370	1.653	2.383	1.651
+3	2.430	1.750	2.318	1.623	2.338	1.633
+4		1.720		1.604		1.617

Figure 3.3 – Ge-O (Si-O) bond lengths vs oxidation state. Results for Si obtained by Hamann [64] are also given.
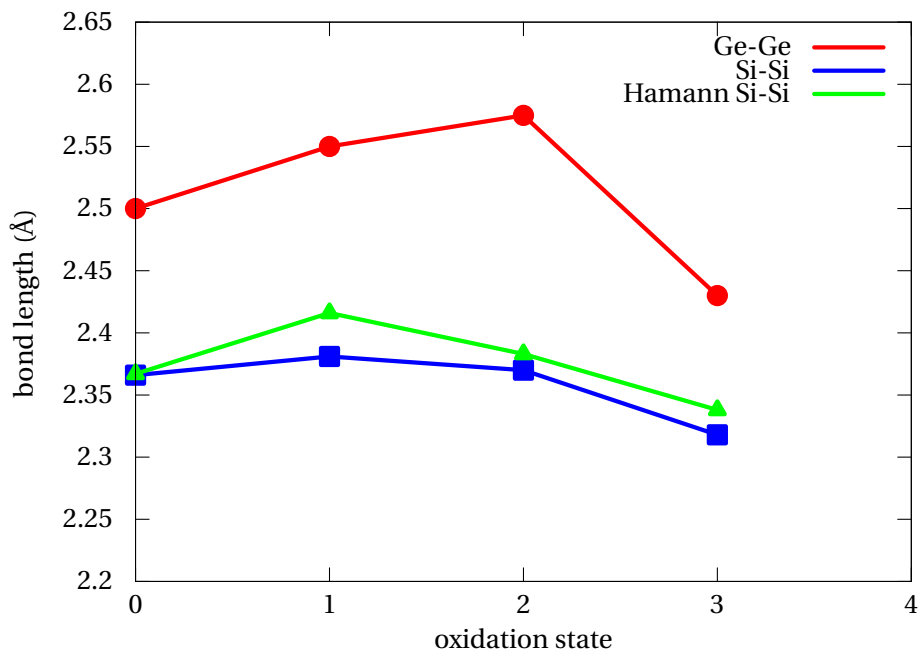

Figure 3.4 – Ge-Ge (Si-Si) bond lengths vs oxidation state. Results for Si obtained by Hamann [64] are also given.
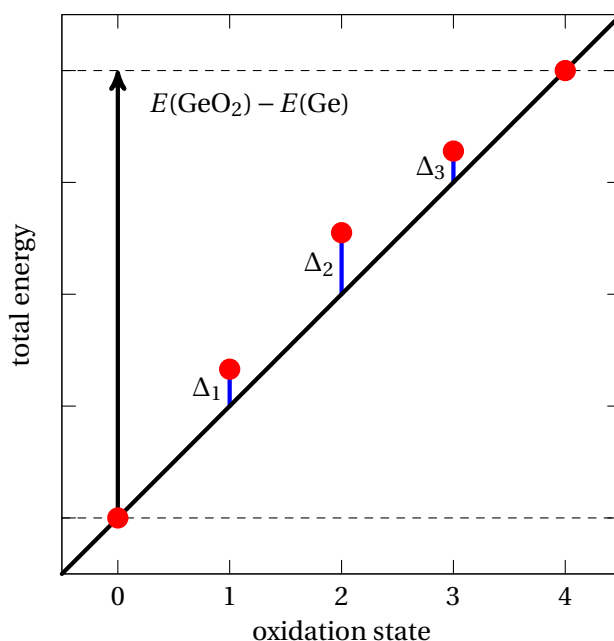
Figure 3.5 – Illustration of the penalty energies.

Table 3.4 – Penalty energies per Ge (Si) atom for the intermediate oxidation states of Ge (Si). Penalty energies for Si as obtained by Hamann [64] are also given. Energies are in eV.

Model	Ge	Si	Hamann
+1	0.18	0.53	0.47
+2	0.07	0.54	0.51
+3	0.01	0.26	0.25

low oxidation states up to 2.575 Å but are found to be shortest (2.430 Å) for the oxidation state +3 (cf. Fig. 3.4).

Penalty energies

Penalty energies Δ_i ($i = 1, 2, 3$ for Ge^{+1}, Ge^{+2}, Ge^{+3}) are derived from the total energies of the substoichiometric oxide models, and define the deviations with respect to a description given in terms of bond energies.

$$\Delta_i = \left(E_i - i\frac{E(\text{GeO}_2) - E(\text{Ge})}{4} \right), \tag{3.3}$$

where E_i is the total energy in oxidation state i. Figure 3.5 illustrates the penalty energy concept. The calculated penalty energies for the three intermediate oxidation states are given
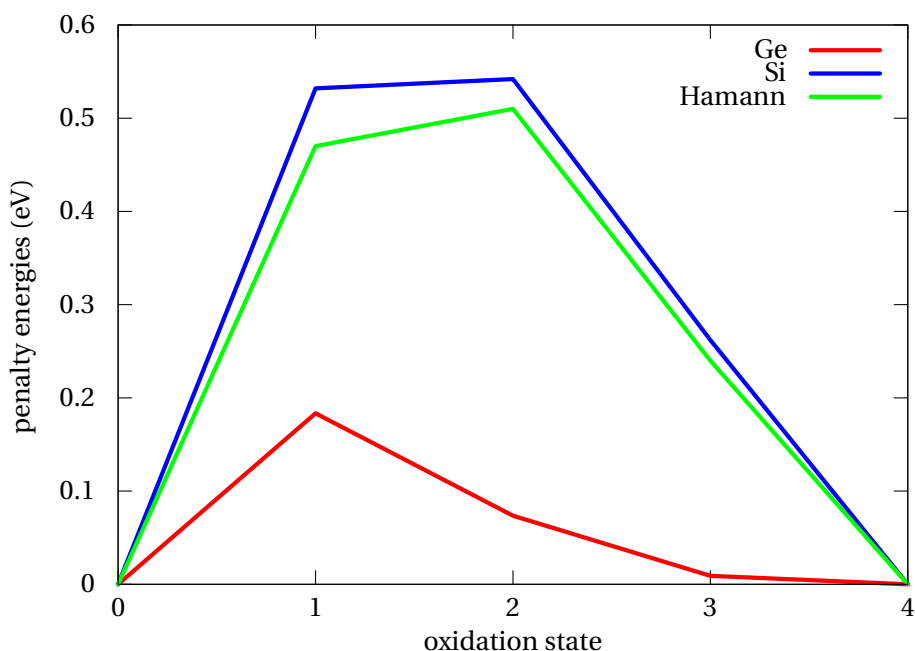
Figure 3.6 – Penalty energies per Ge (Si) atom. Results for Si obtained by Hamann [64] are also given.

in Fig. 3.6 and are summarized in Table 3.4. For the Si oxidation states, we found penalty energies which confirm the values obtained by Hamann [64]. The calculated values also agree with the energies derived from molecular clusters through an alternative derivation [22]. For the Ge oxidation states, penalty energies are found significantly lower than for the respective Si states. This implies that a pure bond-energy picture performs better for a system with Ge-Ge and Ge-O bonds than for an analogous one with Si replacing Ge. The dependence on oxidation state also differs between Si and Ge. For Si, the +1 and +2 oxidation states are the most unfavorable ones with similar penalty energies, whereas for Ge the penalty energy of the +1 state is almost three times larger than that of its main contender, the +2 state. In particular, we point out that the calculated values imply that two Ge^{+2} transform endothermically to a Ge^{+1} and a Ge^{+3}, while this reaction was exothermic for the respective Si states. Hence, these results indicate a higher stability of partially oxidized Ge atoms at Ge/GeO$_2$ interfaces, and suggest that, unlike at Si/SiO$_2$ interfaces, there is no energetic driving force towards the reduction of their concentration and of their spatial extent.

Electronic density of states

The electronic density of states (DOS) of the substoichiometric Ge and Si oxide models are shown in Figs. 3.7 and 3.8, respectively. In the +1 and +2 models, the energy scale is referred to the valence band maximum. The DOSs of the other structures are aligned through their O 2s levels, which are assumed to remain unchanged across the substoichiometric transition region
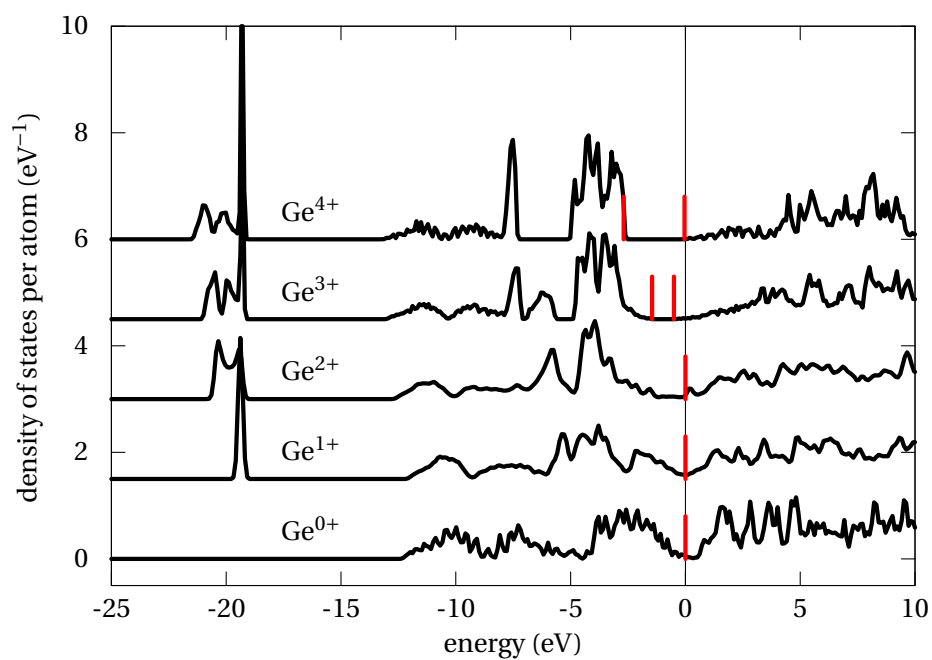
Figure 3.7 – Electronic density of states (DOS) of the (sub)stoichiometric Ge oxide models. The DOSs of the Ge^0 and Ge^{+1} models are referenced with respect to the Fermi energy; the other DOSs are aligned through the O 2s levels. The band edges are indicated. A Gaussian broadening of 0.1 eV is used.
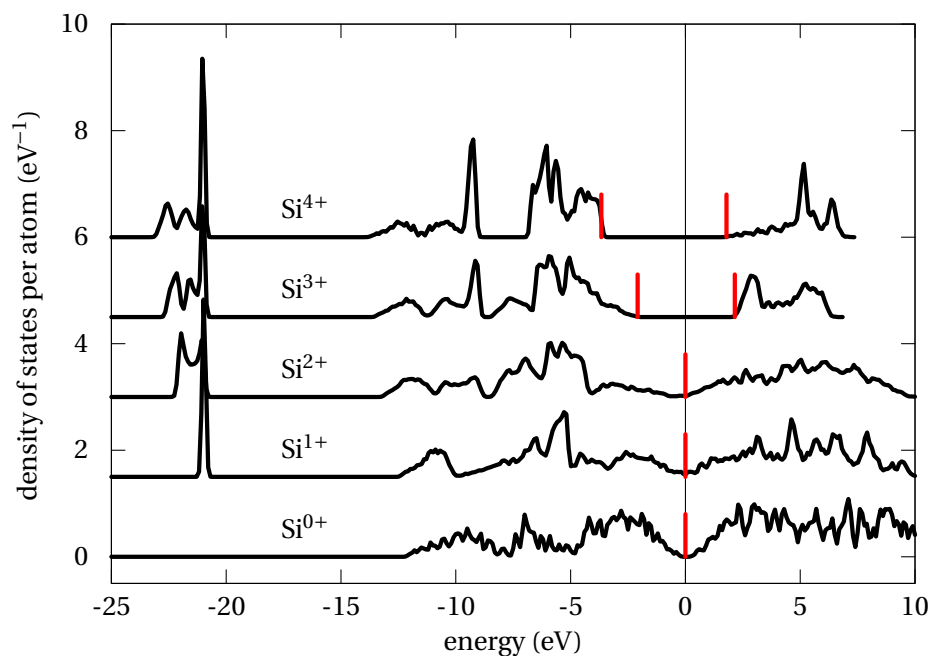

Figure 3.8 – Same as in Fig. 3.7, but for the (sub)stoichiometric Si oxide models.

of the respective interfaces. For the +1 and +2 models of both Si and Ge, we found vanishing band gaps, in accord with the findings of Hamann [64]. This unrealistic result appears to relate to the value of 180° artificially enforced upon the Ge-O-Ge bond angle in our calculations. Indeed, when we relaxed this condition for the Ge^{+2} model, we achieved a band gap of 0.60 eV while observing a negligible variation of the penalty energy. The negligible effect of the band gap is consistent with the fact that periodic and molecular models yield very close penalty energies for Si oxidation states [22]. For the band gaps of the Si^{+3} and Si^{+4} models we obtained 4.23 eV and 5.45 eV, respectively. For the respective Ge models, we also found finite values, viz. 0.95 eV and 2.65 eV.

3.3 Formation of substoichiometric GeO$_x$ at the Ge-HfO$_2$ interface

In this section, we investigate the thermodynamics of oxygen vacancies in Ge-GeO$_2$-HfO$_2$ stacks. We find the oxygen vacancies to be most stable in the germanium oxide layer, thus supporting the formation of a GeO$_x$ transition layer in accord with experimental observations.

We first focus on the semiconductor side of the interface, where a germanium oxide layer inevitably occurs [42]. We first consider the oxygen vacancy in GeO$_2$, where the stable charge state is the neutral one for all chemical potentials bound within the semiconductor band gap. A good estimate for the formation energy of the vacancy can be derived from the decomposition energy per oxygen atom of bulk α-quartz (ΔH^0). In this way, we obtained a ΔH^0 of 2.4 eV for GeO$_2$. It should be noted that this value is significantly lower than for SiO$_2$, for which our calculations give 4.1 eV.

More generally, the germanium oxide is substoichiometric [42]. To estimate the formation energies of oxygen vacancies, we then rely on the validity of a bond-energy picture that includes a penalty energy Δ_i (Eq. (3.3)) for each intermediate oxidation state of germanium [64, 22]. The penalty energies define the deviations with respect to the ideal bond-energy picture. We use the values calculated in the previous section.

In this bond-energy picture, the total reduction reaction can be decomposed into a set of reactions involving sequentially all the suboxide states:

$$\text{Ge}^n\text{-O-Ge}^n \rightarrow \text{Ge}^{n-1}\text{-Ge}^{n-1} + \tfrac{1}{2}\text{O}_2, \tag{3.4}$$

for which the reaction energy ΔH^n is given by:

$$\Delta H^n = \epsilon_{\text{GeGe}} - 2\epsilon_{\text{GeO}} + 2\Delta_{i-1} - 2\Delta_i + \tfrac{1}{2}\mu(\text{O}_2), \tag{3.5}$$

where $\mu(\text{O}_2)$ is the oxygen chemical potential corresponding to the O$_2$ molecule, and ϵ_{GeGe} and ϵ_{GeO} are the Ge-Ge and Ge-O bond energies, respectively. In this scheme, the decomposition
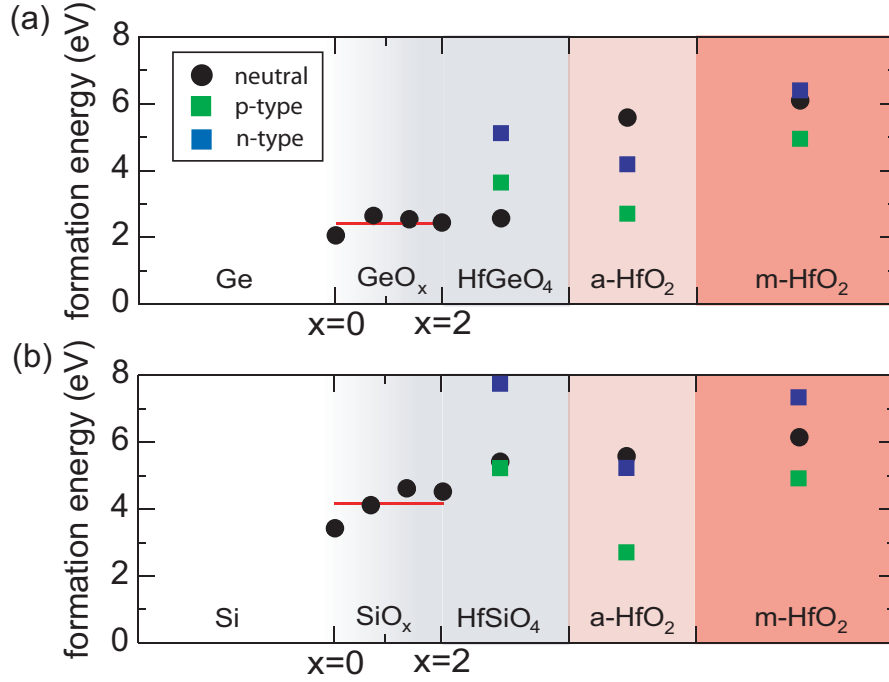
Figure 3.9 – Oxygen vacancy formation energies at (a) the Ge-HfO$_2$ and (b) Si-HfO$_2$ interface
The interfaces are modeled by considering bulk models of Ge(Si)O$_x$, Ge(Si)O$_2$, HfGe(Si)O$_4$, amorphous HfO$_2$, and monoclinic HfO$_2$. The red line in GeO$_x$ corresponds to the decomposition energy per oxygen atom ΔH^0 of Ge(Si)O$_2$. Filled black circles indicate the neutral charge state, and result from ΔH^n in the suboxide region. Filled blue and green squares correspond to the +2 charge state for p-type and n-type germanium, respectively.

energy ΔH^0 reads

$$\Delta H^0 = \epsilon_{\text{GeGe}} - 2\epsilon_{\text{GeO}} + \tfrac{1}{2}\mu(\text{O}_2). \tag{3.6}$$

The calculated ΔH^n are given on the left-hand side of Fig. 3.9. The deviations of ΔH^n from ΔH^0 are found to be very small. This is a direct consequence of the small penalty energies and signifies that the accumulation of oxygen vacancies in the germanium oxide does not require a higher energy expense as the reduction proceeds. By contrast, reaction energies at Si interfaces undergo more significant variations and contribute to enhancing the barrier for suboxide formation.

Next, we focus on the high-κ oxide side of the interface, where monoclinic HfO$_2$ (m-HfO$_2$) is the dominating phase. The oxygen vacancy in m-HfO$_2$ has extensively been studied through hybrid density-functional calculations [157, 54, 35, 26]. For electron chemical potentials ranging within the semiconductor band gap, the neutral (V^0) and the doubly positive (V^{+2}) are the relevant charge states [26]. The formation energy of the neutral vacancy is found at 6.1 eV (Fig. 3.9) and does not depend on the electron chemical potential μ. At variance, the forma-
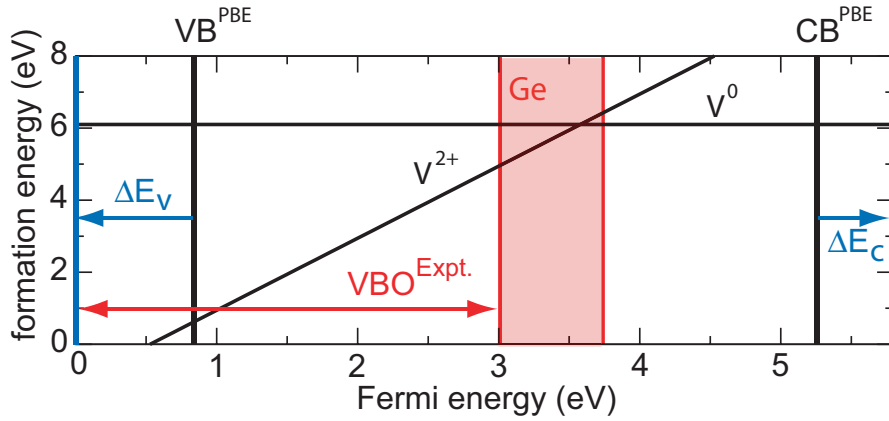
Figure 3.10 – Schematics of the applied alignment scheme for oxygen vacancies in m-HfO$_2$. The defect formation energies vs electron chemical potential and the valence and conduction band edges (E_v and E_c) are first obtained at the PBE level (black). The valence and conduction band shifts (ΔE_v and ΔE_c) are derived from hybrid functional calculations (hPBE, blue). The Ge band edges are positioned through the use of the experimental valence band offset (VBO$^{Expt.}$, red).

tion energy E_f^{+2} of the +2 charge state depends on μ. To address p-type and n-type doping conditions, μ is fixed in correspondence of the Ge band edges, which need to be determined with respect to the electronic structure of m-HfO$_2$.

For this alignment, we first use the hybrid functional to open the band gap to its experimental value, which for m-HfO$_2$ is achieved with a mixing parameter α=15% [5]. We determine the band edge shifts of m-HfO$_2$ (ΔE_v=−0.89 eV and ΔE_c=0.54 eV) by referring the electronic structures in the semilocal and hybrid functional calculation to the average electrostatic potential [5]. We note that on this scale, the +2/0 charge transition level remains essentially unmodified [6]. For the band alignment between Ge and m-HfO$_2$, we finally use the experimentally determined valence band offset (VBO$^{Expt.}$=3.0 eV) [2, 120]. The adopted alignment procedure is illustrated in Fig. 3.10. The formation energies of the +2 charge state are found at 5.3 and 6.8 eV for μ fixed at the valence and conduction band, respectively. Comparison with GeO$_x$ (Fig. 3.9) shows that all charge states of the oxygen vacancy are unstable in the m-HfO$_2$ component of the interface.

In the close vicinity of the interface, specific effects might be operative that cannot be captured by the m-HfO$_2$ model studied so far. These comprise *(i)* structural effects related to disordered HfO$_2$ which ensures the connection to the incommensurate m-HfO$_2$, *(ii)* chemical effects resulting from the composition grading, and *(iii)* polarization effects due to the dielectric discontinuity. While these effects could in principle be investigated at Ge-HfO$_2$ interface models, current computational limitations would prevent a satisfactory statistical treatment. We therefore pursue a more reliable approach based on appropriate bulk models with aligned electronic structures [26, 45].

To account for the disordered nature of the HfO$_2$ layer in the vicinity of the interface, we consider a model of amorphous HfO$_2$ [36]. The formation energy of the neutral oxygen vacancy is found at 5.6 eV [26, 37]. For the +2 state, we align the electronic structure through the Hf 5s states [26] and find formation energies at 2.7 and 4.1 eV for p- and n-type germanium, respectively. As shown in Fig. 3.9, these formation energies are significantly lower than for m-HfO$_2$, but higher than in GeO$_x$. In particular, we note that even in p-type conditions the formation energy in the +2 state still slightly exceeds that of the neutral vacancy in GeO$_x$ (by 0.3 eV). This strongly contrasts with Si-HfO$_2$ interfaces, where a similar analysis shows that the vacancy in the disordered HfO$_2$ layer is favored by 1.6 eV with respect to the vacancy in SiO$_x$ [26].

In the interfacial transition region, the chemical environment of the oxygen atoms is characterized by the simultaneous occurrence of Ge and Hf atoms in the first neighbor shell. Upon vacancy formation, there are two electrons localized on the defect in the neutral state. Because of the higher electronegativity of Ge, these electrons reside in a dangling bond on the Ge atom [156]. Hence, for estimating the formation energies of such vacancies, it is sufficient to adopt a model which reproduces the very local chemical environment. We use crystalline HfGeO$_4$ [135], in which the O atoms bond to both Ge and Hf atoms. For the neutral vacancy, we calculated a formation energy of 2.6 eV, only slightly higher than that of GeO$_x$. In the +2 state, the two electrons residing in the doubly occupied Ge dangling bond are removed. Upon alignment to the interface band diagram through the Hf 5s states [26], we find formation energies of 3.7 and 5.2 eV for p- and n-type germanium, respectively (Fig. 3.9). This indicates that the charged state is not favored when a Ge atom faces the vacancy. For comparison, we also give the corresponding values at the Si-HfO$_2$ interface in Fig. 3.9b.

Polarization effects are negligible because the dielectrics constants of Ge and HfO$_2$ are very close. Taking values of 16 and 17 (Ref. [36]) for Ge and HfO$_2$, respectively, we estimate through classical electrostatics that the oxygen vacancy on the HfO$_2$ side of the interface is destabilized by less than 0.05 eV at a distance of 2 Å from the interface.

In both p-type and n-type Ge devices, the neutral oxygen vacancy located in the GeO$_x$ layer is found to be the most stable state of the defect. This higher stability holds for any intermediate oxidation state of germanium (Fig. 3.9). In the interfacial transition region, the neutral vacancy in a mixed Ge-Hf oxide environment and the doubly positive vacancy in disordered HfO$_2$ are at comparable energies, though slightly higher. At variance, the vacancy formation in m-HfO$_2$ is highly disfavored. Given the low barrier for oxygen vacancy migration in m-HfO$_2$ [40], these results indicate that there is no thermodynamic obstacle for the growth of a substoichiometric GeO$_x$ interlayer. This conclusion is consistent with experimental observations [2, 131, 42, 158], and supports the suggestion that the low valence band offsets measured at Ge-HfO$_2$ stacks correspond to the interface between germanium and substoichiometric GeO$_x$ [2, 131, 158].

3.4 Conclusions

We studied energetic aspects associated to the GeO$_x$ phase at Ge/GeO$_2$ interfaces through an approach based on density functional calculations and crystalline models of various substoichiometric oxides. We found that a pure bond-energy description performs more accurately for substoichiometric Ge oxide systems rather than for analogous Si ones. Furthermore, unlike for Si, our calculations indicate that there is no energetic driving force towards the disproportionation of the intermediate oxidation states of Ge. The higher stability of the GeO$_x$ phase suggests that the partially oxidized Ge atoms at Ge/GeO$_2$ interfaces are more numerous and broadly distributed than respective Si atoms at Si/SiO$_2$ interfaces.

Furthermore, we studied the thermodynamics of oxygen vacancies across Ge/HfO$_2$ interfaces. Oxygen vacancies show a preference for accumulating in the interfacial germanium oxide layer, in strong contrast with the Si/HfO$_2$ interface, where the vacancies tend to be trapped in the interfacial HfO$_2$ layer [26]. This behavior provides an explanation for the formation of substoichiometric GeO$_x$ layers at Ge/HfO$_2$ interfaces [2, 131, 42, 158].

4 Disordered Ge oxides

The electrical performance of Ge-based electronic devices is generally assigned to the quality of the germanium oxide and/or its interface with the germanium substrate [49]. Indeed, improved electrical properties have recently been achieved through the control of the oxidation process of germanium [89]. As seen in the previous chapter, the relative stability of substoichiometric germanium oxides is higher than that of respective silicon oxides, which might lead to different atomic structures in the transition region.

We generate disordered atomistic model structures of GeO_2 and GeO through *ab initio* molecular dynamics in order to achieve a realistic description of the stoichiometric and substoichiometric regions at the Ge/GeO_2 interface. We found that substoichiometric GeO modeled through *ab initio* molecular dynamics shows an unexpected atomic structure formed mainly by threefold coordinated Ge and threefold coordinated O atoms forming valence alternation pairs [76]. Hence, we generated a set of disordered GeO structures with the structure expected from SiO, through a Monte Carlo bond switching approach. Both structures are energetically equivalent, suggesting a mixture of both structure types at the $Ge/GeO_x/GeO_2$ interface.

This chapter is organized as follows. First, we describe the model generation procedure based on molecular dynamics. This technique is then applied to generate one GeO_2 and several GeO models. For GeO, we investigate the influence of different densities by generating a structure with a mass density of 3.95 g/cm^3 and one with a mass density of 4.5 g/cm^3. To avoid possible errors associated with the use of the semilocal PBE functional, we also generate a smaller model within the HSE functional finding no dramatic differences. The resulting structures and their intrinsic defects are analysed. Next, we generate a set of regularly bonded GeO structures through Monte Carlo bond switching and compare them energetically with the structures generated via molecular dynamics.

This chapter contains the contents of previously published papers [17, 18, 19].

4.1 Model generation and structural properties

Model generation via molecular dynamics is computationally very expensive. Usually one starts with classical molecular dynamics and random atomic positions. The classical approach is orders of magnitudes faster than a quantum-mechanical description. This allows to generate a reasonable starting configuration for the *ab initio* molecular dynamics run, in which the different atomic species are homogeneously distributed over the simulation cell. To obtain a reasonable disordered structure via molecular dynamics, one first applies a high temperature to the system. Thus, atoms diffuse inside the model structure and are able to overcome barriers. Through a slow quench, bonds start to freeze and atoms find their equilibrium positions. When the quenching is too fast, atoms get stuck in an unfavoured high-temperature configuration. To guaranty a significant energy separation between filled and empty electronic states, which is important in a Car-Parrinello molecular dynamics [114], the initial structure should show a low defect density. When these conditions are fulfilled, *ab initio* molecular dynamics can overcome some limitations of the classical description and improve the structural properties of a material.

GeO$_2$

The model generation procedure adopted for the germanium dioxide model is based on a sequential process. First, classical molecular dynamics simulations are used for generating a starting configuration [61]. Therefore, a pair potential of the following form is used

$$V(r_{ij}) = \frac{q_i q_j}{r_{ij}} - \frac{A_{ij}}{r_{ij}^6} + B_{ij} e^{-C_{ij} r_{ij}} \tag{4.1}$$

which represents Coulomb, van der Waals, and repulsion energies, respectively. Here r_{ij} is the interatomic distance between atom i and atom j. The effective charge q_i is $q_{Ge} = 1.5$ and $q_O = -0.75$. The van der Walls coefficients A_{ij}, the softness parameter B_{ij}, and the repulsive radii C_{ij} are taken from Ref. [61]. Our model consists of 126 atoms at the experimental density of 3.65 g/cm^3 [155]. The classical molecular dynamics is performed with the MOLDY program [77].

In the next step, *ab initio* molecular dynamics is used to improve the germanium dioxide model. The coordinates obtained through classical molecular dynamics are taken as initial configuration. A time step of 0.175 fs is used. The structure is heated for 4 ps with a Nosé thermostat up to 1500°C, and then quenched in a step-wise fashion to a non-diffusive state. The molecular dynamics run lasted for about 10 ps. A final structural relaxation, until the average atomic force drops below 10^{-3} Ry/bohr, is performed.

In the following, structural properties of the germanium dioxide model are given, and compared to experimental properties. The partial pair correlation functions $g_{\alpha\beta}(r)$ are experimentally available through neutron and x-ray scattering experiments. These functions give the
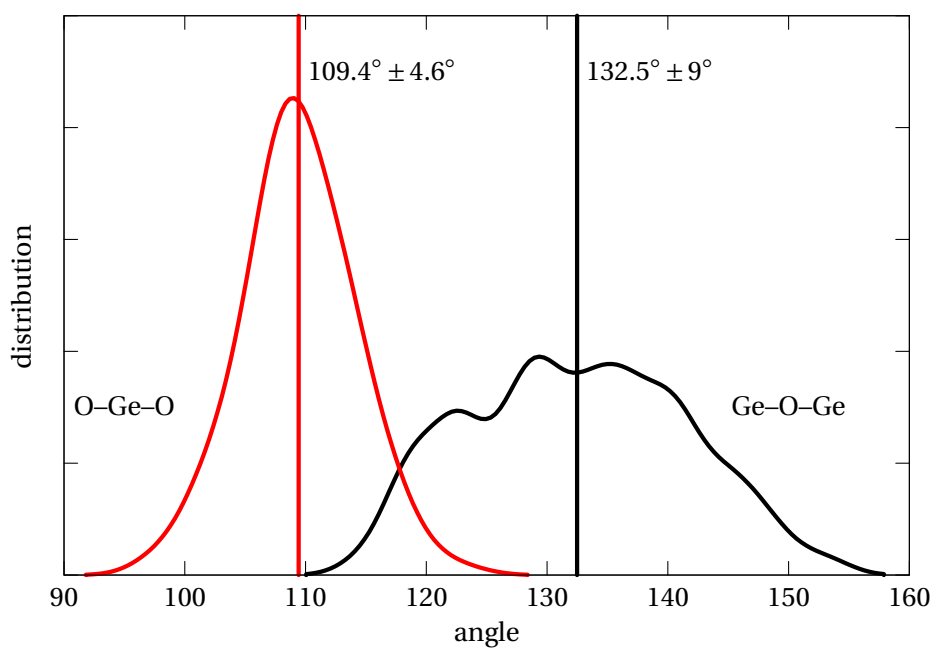
Figure 4.1 – Angle distribution for the amorphous GeO_2 model with 126 atoms. The angles around the germanium atom are characterized by a distribution with an average of 109.4° and standard deviation of 4.6°. For the distribution of Ge–O–Ge angles, the average is 132.5° and the standard deviation is 9°.

density probability for an atom of the α species to have a neighbor of the β species at a given distance r.

$$g_{\alpha\beta}(r) = \frac{dn_{\alpha\beta}(r)}{4\pi r^2 dr \rho_\alpha} \tag{4.2}$$

with $\rho_\alpha = V/N_\alpha$. For calculating $dn_{\alpha\beta}(r)$ one counts the number of atoms β in a shell of thickness Δr at a distance r from atoms of type α. Δr is a free parameter and should be reasonably small.

The average Ge–O bond length (1.78 Å) corresponds to the first maximum of g_{GeO} and is found to be only slightly larger than the experimental one (1.73 Å[125]) in accord with the general tendency of the PBE functional to overestimate bond lengths [46]. The shortest distance between two oxygen atoms or two germanium atoms can be seen from the partial pair correlation function g_{OO} and g_{GeGe}, respectively (Fig. 4.2a). The first maximum of g_{OO} is at 2.88 Å whereas that of g_{GeGe} is at 3.22 Å. This is consistent with the fact that Ge–O–Ge angles are generally larger than O–Ge–O angles.

Figure 4.1 shows the angle distributions in the model of amorphous germanium dioxide. The angles around the germanium atom are close to the tetrahedral angle. The standard deviation of this angle distribution is $\sim 5°$. The Ge–O–Ge angle distribution has an average angle of 132.5° and a standard deviation of $\sim 9°$, in excellent agreement with Ge–O–Ge angle of 132° inferred from experiment [155].

The topology of disordered network-forming materials is usually described through the ring statistics [62]. A series of atoms and bonds connected sequentially without overlay is called a path. Following this definition, a ring is a closed path. Each atom of this network can be involved in numerous rings, each ring being characterized by its size. There exist several definitions for counting rings in a network topology. The best known are the criteria of King [78] and the shortest path criteria [62]. A good overview of the different definitions is given in Ref. [126]. Crystal structures have a small number of equally long rings. Quartz, for example, has 12 and 16 membered rings following the King's criteria. Our amorphous GeO_2 model shows a distribution of rings of various sizes. The three smallest rings are six membered rings, in accord with experimental observations on amorphous GeO_2 [100]. Such six-membered rings are quasiplanar, as can be inferred from the sum over all bond angles in the ring. The average angle over the six-membered rings in this model structure is 694°, only slightly lower than the ideal value of 720°. But the structure has also rings of other length (8, 10, 12, 14, 16, 18 membered rings following the King criteria).

The formation energy of the amorphous germanium dioxide model is 4.74 eV per GeO_2 unit, when referred to bulk germanium and the oxygen molecule as done in chapter 3.1. This is ~ 0.1 eV smaller than for the considered crystalline models (compare with chapter 3.1). This comparison indicates that the amorphous model shows a high stability.

Substoichiometric GeO

We took GeO as a representative composition of substoichiometric germanium oxide. We generated various models with a size of 120 atoms by *ab initio* molecular dynamics. One at a density of 3.95 g/cm^3 and two at a higher density of 4.50 g/cm^3. These densities correspond to linear interpolations between amorphous GeO$_2$ and either crystalline or amorphous germanium [148]. Empiric pair potentials for classical molecular dynamics are not available for GeO, therefore we started the model generation from random atomic positions. We relaxed the positions of the atoms for a set of ten model structures at a mass density of 3.95 g/cm^3 within our density functional scheme. The model with the lowest total energy was selected as starting configuration for the Car-Parrinello molecular dynamics. The model generation through molecular dynamics was done through a cook and quench procedure. The systems were equilibrated for at least 10 ps at a temperature of 1000 K. The quench to 300 K was achieved at a rate of 200 K/ps. All final structures were relaxed until the average atomic force was lower than 10^{-3} Ry/bohr. We obtained starting coordinates for the high-density model, through rescaling of the final coordinates of the low density model. The molecular dynamics procedure was than similar to the low-density model. The second high-density model was made within the HSE hybrid density functional scheme. Hybrid density functionals are computationally extremely expensive. Therefore, we generated a model with only 72 atoms. After molecular dynamics at the PBE level, 2 ps of HSE molecular dynamics at 1000 K were performed. Afterwards, we quenched the structure in 5 ps to 500 K. This was followed by a final structural relaxation similar to the other models.

Figure 4.2b shows the partial pair correlation functions for the low-density model. No significant differences with respect to the high-density model (Fig. 4.2c) are visible. g_{GeO} has an isolated first peak [1] with a maximum at $r = 1.91$ Å. In GeO, the Ge–O bonds appear to be slightly larger than in GeO$_2$, with the first maximum in g_{GeO} at 1.91 Å compared to 1.78 Å for GeO$_2$. The average Ge-O bond length of the model obtained through the HSE functional (Fig. 4.2d) is 1.85 Å. Table 4.1, summarizes the average Ge-O bond length and the average O-Ge-O angle for the generated model structures and compares them with those of the amorphous GeO$_2$ structure.

The partial pair correlation function between germanium atoms has no isolated peak. It assumes a finite value at $r = 2.45$ Å, and does not fall back to zero. The first maximum of g_{GeGe} is at 2.64 Å. The following minimum, which overlaps already with the second nearest-neighbors peak is at $r = 2.8$ Å. No distinct distance between two germanium atoms defining a Ge–Ge bond is distinguishable.

Thus, the purely geometric analysis of the distances between two Ge atoms is not sufficient to define a Ge–Ge bond. The geometric analysis is completely blind to the actual electronic charge distribution, which is important in any description of chemical bonds.

---

1. For smaller and larger values of r g_{GeO} gets to zero.
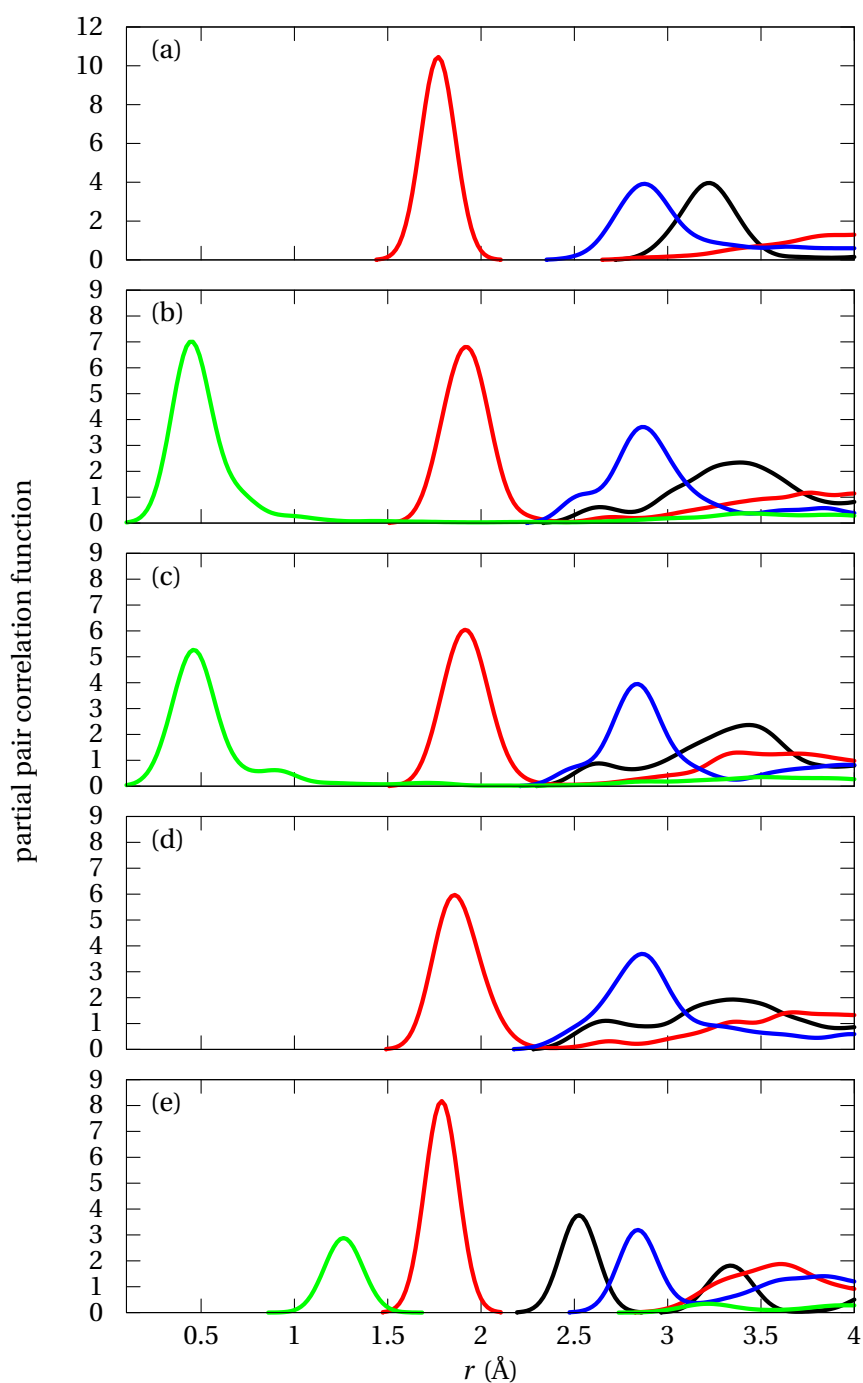
Figure 4.2 – Partial pair correlation functions for different GeO$_x$ structures. (a) GeO$_2$ model, (b) low-density model generated via molecular dynamics, (c) high-density model generated via molecular dynamics model, (d) high-density model generated via hybrid functional molecular dynamics, (e) low-density model generated with a Monte Carlo bond switching method. A color coding was used to indicate the different PCFs: g_{GeO} (red), g_{OO} (blue), g_{GeGe} (black), and g_{GeWFC} (green). g_{GeWFC} was scaled down by a factor of 5. For a better view, a Gaussian smearing of 0.09 Å was used.

Table 4.1 – Properties of the GeO models generated by *ab initio* molecular dynamics (MD) and by bond switching Monte Carlo (MC), compared to a model of amorphous GeO$_2$: the number of atoms N, the density ρ (in g/cm^3), the average Ge-O bond length (in Å), the average O-Ge-O angle, and the bandgap E_g (in eV).

		Funct.	N	ρ (g/cm^3)	$d_{\text{Ge-O}}$ (Å)	$\angle$ O-Ge-O
Model M1	GeO MD	PBE	120	3.95	1.92	95.0°
Model M2	GeO MD	PBE	128	3.95	1.93	94.1°
Model M3	GeO MC	PBE	128	3.95	1.79	106.3°
Model M4	GeO MD	PBE	120	4.50	1.93	96.0°
Model M5	GeO MD	HSE	72	4.50	1.87	97.6°
Model M6	GeO$_2$	PBE	126	3.64	1.76	109.4°
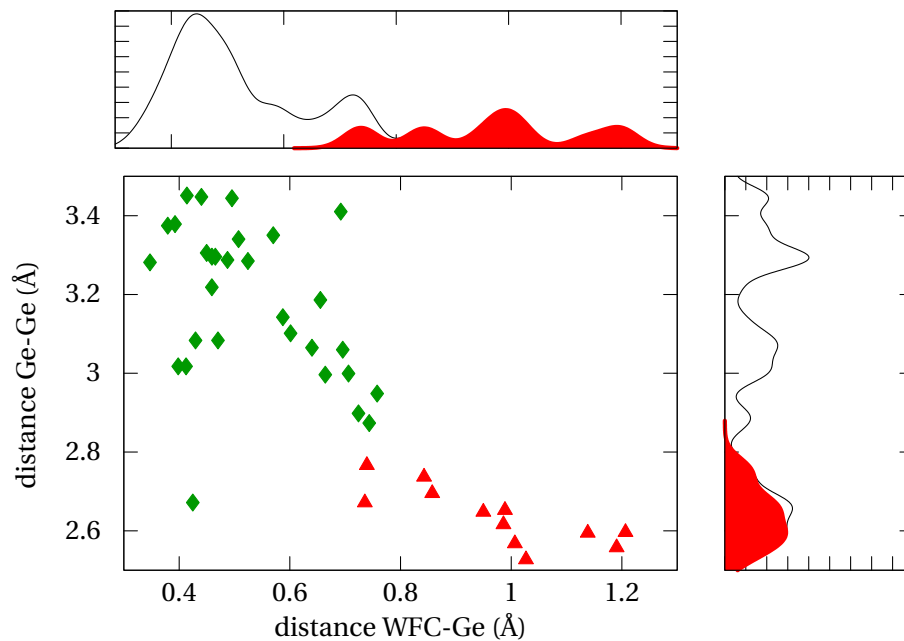
Figure 4.3 – Ge–Ge bond analysis with Wannier function center (WFC) for a GeO model generated via molecular dynamics. On the y-axis, the distance between two Ge atoms which potentially form a bond. Their distance distribution is given in the separate graph on the right hand side. On the x-axis the distance between one of the Ge atoms and a MLWF center along the possible bond. The projected distribution is given in a second graph above. WFCs belonging to a Ge dangling bond and to a Ge–Ge bond are labelled with green diamonds and red triangles, respectively.

Table 4.2 – Percentage of ℓ-fold coordinated Ge and O atoms in the low-density (3.95 g/cm^3) and high-density (4.50 g/cm^3) GeO models generated by molecular dynamics. Cutoff radii of 2.8 and 2.15 Å were used for Ge-Ge and Ge-O bonds.

GeO model	Ge				O	
	$\ell=2$	$\ell=3$	$\ell=4$	$\ell=5$	$\ell=2$	$\ell=3$
low-density	20.2	57.3	22.5	0	43.0	57.0
high-density	6.7	56.7	30.0	6.7	34.4	65.6

For a better criterion for identifying bonds between two germanium atoms, we calculated Wannier functions center for the GeO models. We used the occupied Kohn-Sham orbitals and transformed them to the same number of maximally localized Wannier functions. Sorting the MLWFs by their spread, it was possible to group them in two types. The MLWFs with larger spread (> 1.5 Å^2) are located around germanium atoms. The second group with spread < 1.0 Å^2 are located close to oxygen atoms. For an ideal Ge–Ge bond, the MLWFs are expected to be centered between the two Ge atoms. In Figure 4.3 we show on the y-axis, the distance between two Ge atoms which potentially form a bond. Their distance distribution is given in the separate graph on the right hand side.

On x-axis the distance between one of the Ge atoms and a MLWF center along the possible bond is given. The projected distribution is given in a separate graph above. For the definition of a Ge–Ge bond two criteria have to be satisfied (i) the distance between two Ge atoms should be not too large, and (ii) the bond related WFC should be not too close to one of the Ge atoms. We consider that a Ge–Ge bond forms when the Ge–Ge bond distance is characterized by a distance lower than 2.8 Å and, concurrently, the Ge-WFC distance is larger than 0.6 Å. The selected Ge–WFC distances are colored in red. The selected distances are indicated by the distributions shaded in red. This confirms that the value of 2.8 Å is indeed appropriate for identifying Ge-Ge bonds.

The average coordination number at a specific distance, can be calculated from the radial distribution function $g_{\alpha\beta}(r)$. From Eq. (4.2), one gets

$$n_{\alpha\beta}(r) = 4\pi\rho_\beta \int_0^r g_{\alpha\beta}(r')r'^2 dr' \tag{4.3}$$

where $n_{\alpha\beta}(r)$ is the running coordination number. The average coordination number of particles β in the first shell of particles α is just the value of the running coordination number function at the position of the first minimum in the $g(r)$ function. The average coordination number of the oxygen atoms at the cutoff distance of 2.15 Å in the model structure generated by molecular dynamics is ~ 2.6. Taking 2.8 Å as the cutoff radius for the Ge–Ge bond, the low-density model shows an average coordination between Ge atoms of ~ 0.4, whereas in the high density model this value is ~ 0.7.
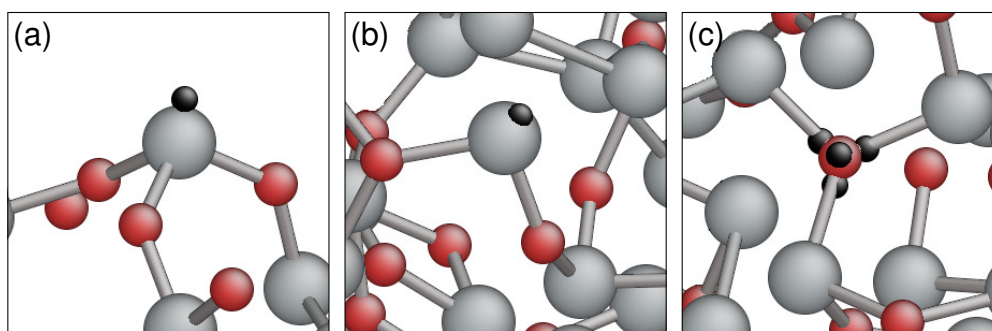
Figure 4.4 – Representative atomic configurations of GeO structures: (a) the negatively charged threefold coordinated Ge atom (large grey balls), (b) the charge neutral twofold coordinated Ge atom, and (c) the positively charged threefold coordinated O atom (medium-size red balls). The electronic structure is illustrated through the centers of maximally localized Wannier functions (small black balls).

Through a coordination number analysis for each atom in the model structure, we show, that the O coordination is predominantly threefold rather than twofold. The Ge coordination is also predominantly threefold, but shows fractions of twofold, fourfold, and fivefold coordinations. By comparing the low-density and high-density models, one recognizes that the average coordination of Ge atoms increases with density. However, even in the high-density model, a sizeable fraction of twofold coordinated Ge atoms occurs. We summarized the ℓ-fold coordination of the atoms in Tab. 4.2. Evidence for the occurrence of twofold coordinated Ge atoms in O-deficient GeO_2 has previously been inferred from photoluminescence studies [134].

The observed coordinations are indicative of valence alternation pairs associated to the creation of charge centers [76]. To identify the positive and negative charge centers, we used maximally localized Wannier functions [98]. The positive charge centers consist of threefold coordinated O atoms (Fig. 4.4c), while the negatively charged centers are formed by threefold or fivefold coordinated Ge atoms. In case of threefold Ge atoms, the negative charge results from doubly occupied dangling bonds (Fig. 4.4a). The twofold coordinated Ge atoms carry an empty and a doubly-occupied dangling bond, and are thus charge neutral (Fig. 4.4b).

4.2 Monte-Carlo

We also generated models of substoichiometric germanium oxide through a bond switching Monte Carlo method [144, 154], based on a limited list of bond switching rules, which keep the Ge atoms fourfold coordinated and the O atoms twofold coordinated. After every bond switch the atomic structure is relaxed. For this purpose, a Hamiltonian which depends on

bond length and bond angles is used [144]:

$$E_{\{r\}} = \frac{1}{2}\sum_i k_b (b_i - b_0)^2 + \frac{1}{2}\sum_{i,j} k_\theta (\cos\theta_{ij} - \cos\theta_0)^2. \tag{4.4}$$

The first term represents the cost of the bond length. The second term is responsible for the bond-angle distortions. Here $\{r\}$ is the set of atomic positions, $E_{\{r\}}$ is the total energy for a given network topology and given $\{r\}$, i represents the ith bond with its length b_i, and θ_{ij} is the angle between bonds i and j to a common neighboring atom. The material parameters depend implicitly on the type of atom: b_0 is the preferred bond length, θ_0 is the preferred bond angle, and k_θ and k_b are spring constants. The parameters used for the model generation of GeO are tabulated in table 4.3.

In the following, the forces corresponding to the energy expression (4.4) are expressed separately for the distance and angle dependent contributions. The bond dependent contribution is expressed in terms of atomic coordinates as

$$F_a^x = 2 k_b \sum_i (x_i - x_a) \frac{(b_i - b_0)^2}{b_i}, \tag{4.5}$$

where F_a^x is the x component of the distance dependent force component between atom a and its neighbouring atoms i.

The force component in the x direction of atom a resulting from the angular part of Eq. (4.4) reads:

$$F_a^x = 2 \sum_{i,j} \left(\frac{2(x_i - x_a)\langle \mathbf{r}_{ia}, \mathbf{r}_{ja} \rangle}{b_i^4 b_j^2} + \frac{2x_a - x_j - x_i}{b_i^2 b_j^2} + \right.$$
$$\left. + \frac{2(x_j - x_a)\langle \mathbf{r}_{ia}, \mathbf{r}_{ja} \rangle}{b_i^2 b_j^4} \right) \cdot \left(\cos\theta_{ij} - \cos\theta_0 \right), \quad (4.6)$$

where x_a, x_i, and x_j are the x components of the positions of atom a, i, and j, respectively. $\mathbf{r}_{ia}$ is the vector which connects the positions of atom i and atom a, d_{ia} is the distance between atom i and atom a.

Regularly bonded GeO

We generated a set of regularly bonded GeO models through the above described procedure. Starting from a β-cristobalite structure of 128 atoms at a mass density of 3.95 g/cm^3, we first applied a high temperature to induce disorder in the system. Than the temperature was quenched and an equilibrium structure was reached. Finally, the atomic positions of 34 different model structures of this type were relaxed within our density functional scheme.

The pair correlation function of a regularly bonded GeO model is given in Fig. 4.2e. The Ge-O bond length is slightly smaller than in the molecular dynamics models. The Ge–Ge bond is

Table 4.3 – Parameters used for the model generation through Monte Carlo bond switching. The energies are taken from Ref. [144]. Distances are in Å.

	k_b (eV/Å^2)	b_0 (Å)	$k_\theta (eV)$	$\cos\theta_0$
Ge–Ge	9.08	2.55	-	-
Ge–O	27.0	1.80	-	-
Ge–Ge–Ge	-	-	3.58	$-1/3$
Ge–O–Ge	-	-	0.75	-1
O–Ge–O	-	-	4.32	$-1/3$

well defined at a distance of 2.53 Å. The WFC falls exactly in the middle of the Ge–Ge bond. All oxygen atoms are twofold coordinated and all germanium atoms are fourfold coordinated by construction.

Figure 4.5 shows a ball and stick model for a model generated through molecular dynamics and for a regularly bonded GeO structure. Through a color coding the different coordinations are visualized.

Figure 4.6 shows the total energy distribution of the 34 regularly bonded GeO structures after structural relaxation. The structure made by Monte Carlo bond switching with the lowest total energy (Tab. 4.1) exceeds by only 19 meV per Ge atom the total energy of the most stable structure achieved by *ab initio* molecular dynamics. Two other MD structures are also given in Fig. 4.6 showing similar energies. For comparison, the figure also shows the energy per GeO unit of two crystalline structures: the β-cristobalite-like structure used for the penalty energies in chapter 3, and a fully optimized α-cristobalite like structure. The similar energies suggest that the two kinds of structural organizations are competitive in substoichiometric germanium oxide.

4.3 Electronic density of states

The alignment of the electronic structures of the different bulk models (GeO$_2$, GeO modeled with molecular dynamics, GeO modeled with Monte Carlo bond switching) is achieved through the O $2s$ state. For silicon it has been shown, that the oxygen $2s$ state is constant across the Si/SiO$_2$ interface [45]. We show that this also holds for the Ge/GeO$_2$ interface. For this purpose, we generate a model interface between GeO$_2$ and GeO. For the GeO$_2$ region of the interface we take the previously generated GeO$_2$ model. Then, we add a GeO region, and perform a few ps of molecular dynamics before relaxing the atomic positions of the structure. For this test, it is not critical that the interface has a very high quality.

In the generated GeO$_2$/GeO interface model, the oxygen coordination thus evolves from predominantly twofold in GeO$_2$ to predominantly threefold in GeO. In the upper panel of Fig. 4.7, the atomistic structure of this interface is illustrated. The coordinations of the oxygen
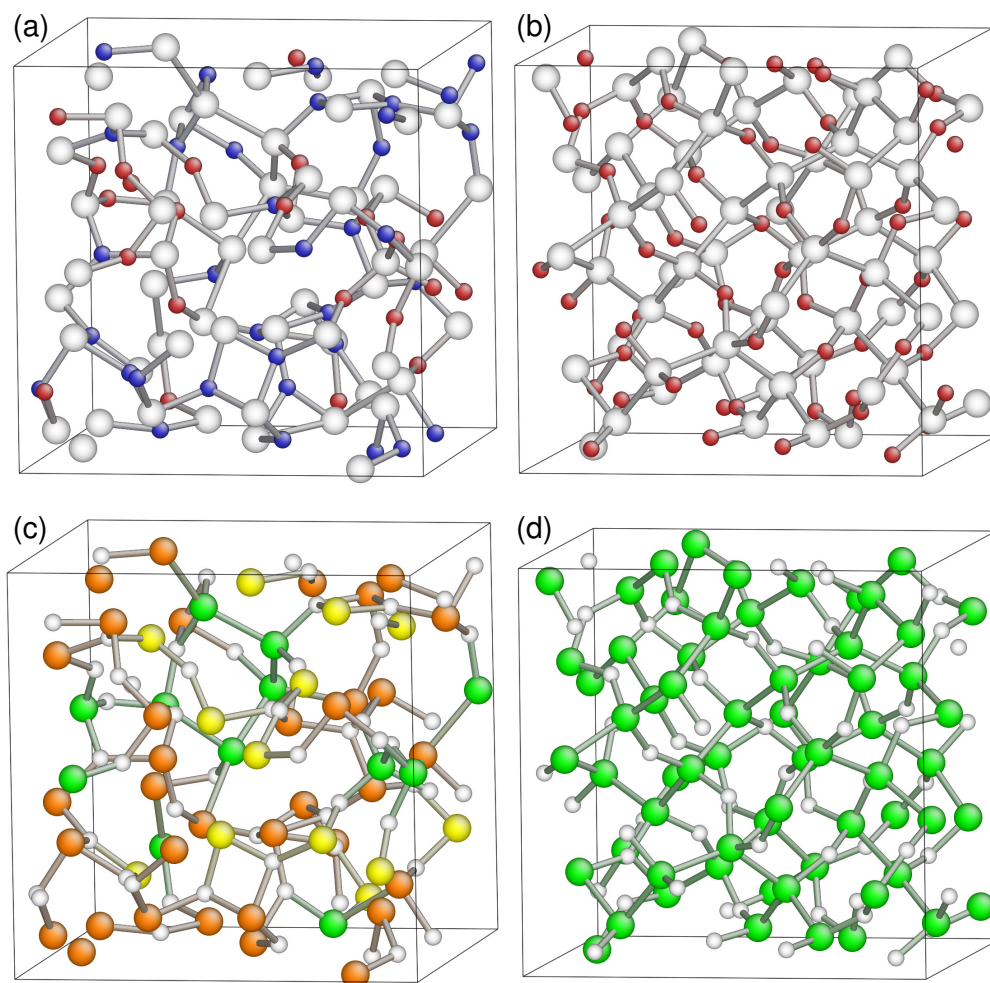
Figure 4.5 – Atomistic models of GeO generated through *ab initio* molecular dynamics [(a) and (c)] and Monte Carlo bond-switching simulations [(b) and (d)]. In (a) and (b), the O atoms are highlighted in red (light gray) for twofold and in blue (dark gray) for threefold coordination, while the Ge atoms are white. In (c) and (d), the Ge atoms are highlighted in yellow (light gray), orange (gray), and in green (dark gray) for twofold, threefold, fourfold coordination, respectively, while the O atoms are white.

atoms are highlighted through the same color code used in Fig. 4.5(a) and (b). We investigated the behavior of the O $2s$ states across the interface. The electronic density of states was projected on the WFC for every WFC close to an oxygen atom (cf. chapter 2 Eq. (2.65)). From this, we obtained an average O $2s$ level. In Fig. 4.7, we plot these energies as the oxygen atom varies across the interface. Individual levels are quite scattered, but their planar average remains remarkably constant. This result indicates that the electronic structures of GeO and GeO$_2$ can be drawn on a common scale through the alignment of the average O $2s$ level.

Through this alignment, the electronic density of states (DOS) of the two GeO models can

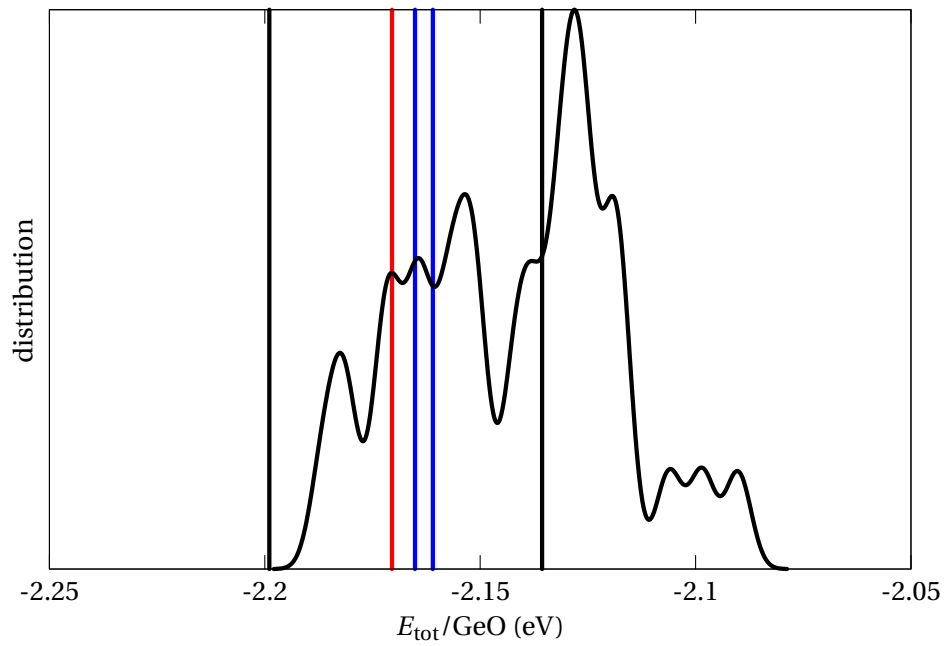Figure 4.6 – Distribution of total energies for the 34 regularly bonded GeO models. A Gaussian smearing of 3 meV was used. The total energies of the two low-density models (black) and of the single high-density model (red) generated via molecular dynamics are given for comparison. We also show the total energies of crystalline α- and β-cristobalite-like structures (blue). The total energies are given per GeO unit.
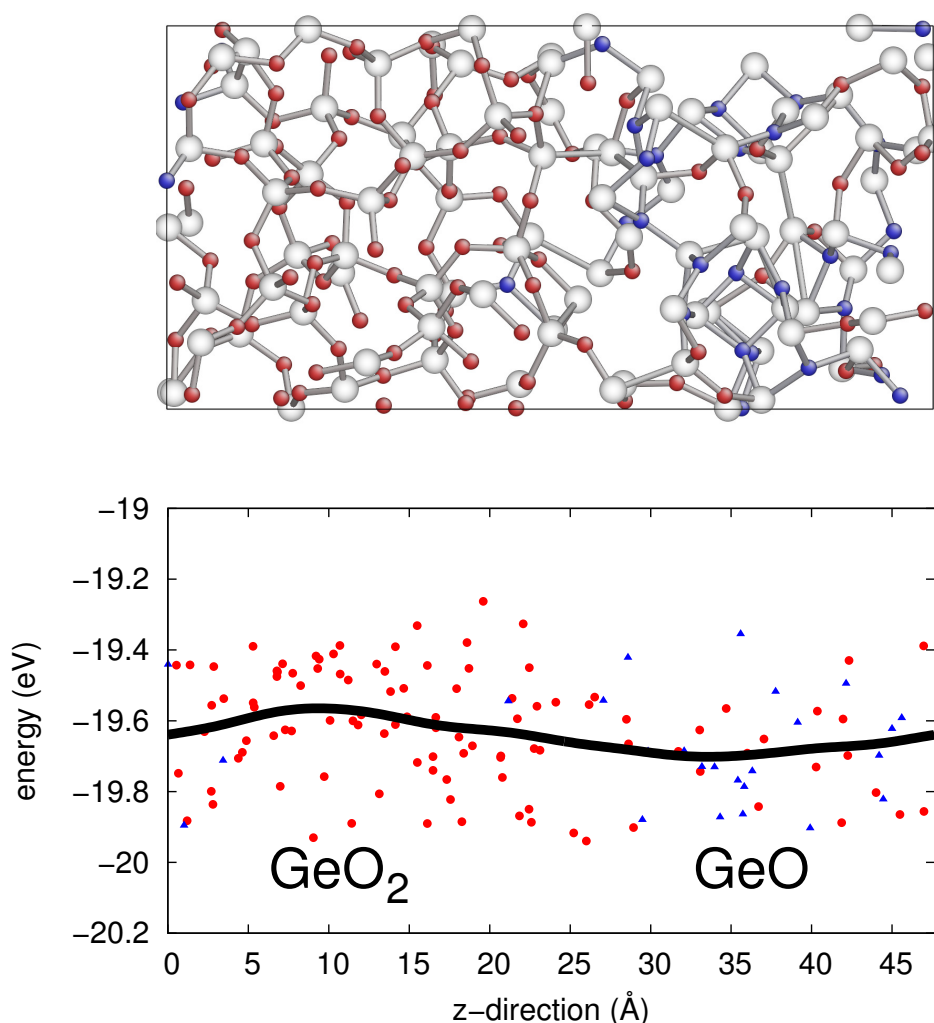
Figure 4.7 – Upper panel: Atomistic model of the GeO/GeO$_2$ interface generated by *ab initio* molecular dynamics. The O atoms are highlighted with the same color code as in Figs. 4.5(a) and (b), while the Ge atoms are white. Lower panel: Individual O 2s levels for twofold coordinated oxygen atoms (disk symbols), and for threefold coordinated oxygen atoms (triangles). Their planar average (solid curve) across the GeO/GeO$_2$ interface is also shown.

be compared to that of amorphous GeO$_2$ (Fig. 4.8). Through the choice of the fraction of exact exchange in the hybrid functional ($\alpha = 25\%$), the band gap of the amorphous GeO$_2$ model coincides with the experimental value of 5.6 eV [86]. The band gaps of the GeO models obtained with the same hybrid functional are noticeably smaller. The calculations give very similar band gaps for the structure obtained by molecular dynamics (2.8 eV) and that obtained by Monte Carlo (2.8 eV). As seen in Fig. 4.8, the band-gap reduction with respect to that of GeO$_2$ is mainly due to an upward shift of the valence band edge for both GeO models. We
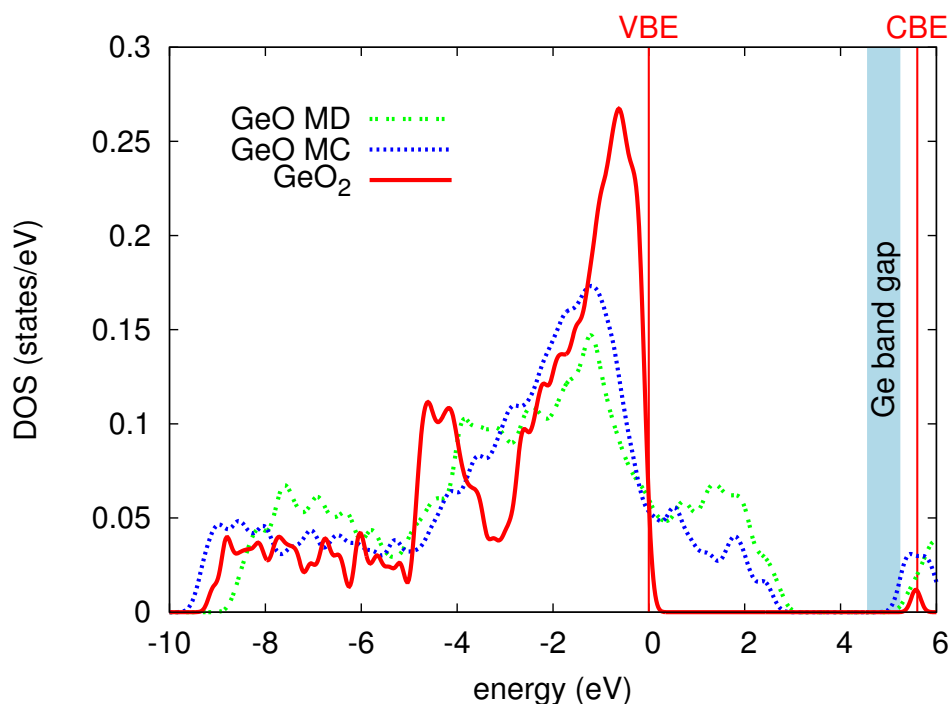
Figure 4.8 – Electron densities of states (DOS) for the GeO models generated by *ab initio* molecular dynamics (MD) (green, double-dotted) and Monte-Carlo bond-switching (MC) (blue, dotted) simulations, compared to that of amorphous GeO_2 (red, solid). The alignment is achieved through the O $2s$ states. A Gaussian broadening of 0.15 eV is used. The indicated position (shaded) of the germanium band gap is obtained from the experimental value of 4.5 eV for the valence band offset between Ge and GeO_2 (Ref. [119]). The band edges (VBE and CBE) of GeO_2 are also indicated.

calculated valence band offsets of 2.7 and 2.5 eV for the GeO structures obtained by molecular dynamics and Monte Carlo, respectively. The GeO valence-band states falling into the GeO_2 band gap correspond to dangling bonds of threefold coordinated Ge atoms or to Ge-Ge bonds, which are found in the same energy range. Hence, despite the important structural differences between the two GeO models, their electronic densities of states do not differ significantly.

Focusing on the electronic DOS of the valence band, we note that the main peaks of the GeO models shift to lower energies compared to that of GeO_2. This observation agrees with photoemission data obtained for substoichiometric germanium oxide films [14] and confers support to our description. Furthermore, it is interesting to position the Ge band gap in Fig. 4.8. Experimental values for the Ge/GeO_2 valence band offset show considerable indetermination, with values ranging between 3.6 and 4.6 eV [106, 97, 119, 158]. We here take the value of 4.5 eV for this offset, which appears consistent with the most recent measurements [119, 158]. With this value, the states of the suboxide models do not fall within the Ge band gap (the nonvanishing DOS in Fig. 4.8 results from the adopted broadening). Furthermore, this leads to a valence band offset of 1.8 eV (2.0 eV) between Ge and GeO when we consider the structure

obtained by molecular dynamics (Monte Carlo), in good agreement with the value of 2.2 eV measured for Ge/HfO$_2$ stacks [131]. Therefore, this accord supports the occurrence of an interlayer composed of substoichiometric germanium oxide in such stacks.

4.4 Conclusion

We studied the atomic and electronic structure of substoichiometric germanium oxide models of GeO generated by *ab initio* molecular dynamics. The analysis of the structure reveals the occurrence of high proportions of valence alternation pairs [76] consisting of occupied dangling bonds at threefold coordinated Ge atoms and of threefold coordinated O atoms. The structure also reveals a significant fraction of twofold coordinated Ge atoms, previously identified as defects in oxygen deficient GeO$_2$ [134]. For comparison, we also generated a GeO model structure through a Monte Carlo bond switching procedure, which by construction preserves coordinations obeying the $8 - N$ rule. The energetics of the two kinds of structures were found to be very close suggesting that they are competitive.

The electronic structures of the two bulk models of GeO and that of GeO$_2$ were aligned through the O $2s$ levels which were found to remain constant across a GeO/GeO$_2$ interface model. The electronic densities of states of both GeO models showed a similar reduction of the GeO$_2$ band gap, mostly resulting from a significant upward shift of the valence band edge. The valence band offsets between Ge and GeO agree with measured offsets between Ge and the interlayer in Ge/HfO$_2$ stacks, lending support to an interlayer composition of substoichiometric germanium oxide.

5 Valence alternation pairs

In this chapter, we discuss possible consequences of the formation of valence alternation pairs at the Ge/GeO$_2$ interface. To investigate whether the coordination defects in GeO$_x$ identified in chapter 4 could be responsible for electron and hole trapping, we have studied the addition and removal of electrons, respectively. In the case of electron trapping, two electrons were added to the GeO$_x$ model. The added electrons were trapped in a state formed by the overlap between two unoccupied Ge dangling bonds. Upon negative charging, the Ge–Ge distance decreased, leading to the formation of a Ge–Ge bond. In contrast, upon electron removal, the hole formation corresponds to the breaking of an existing Ge–Ge bond leading to the formation of two positively charged threefold coordinated O atoms. Thus, it appears that the addition and removal of electrons directly correlates with the number of Ge–Ge bonds. Another process in which VAPs might play a role is hydrogen passivation. One reason for the good performance of the Si/SiO$_2$ interface is the possibility to passivate silicon dangling bonds at the interface. This process does not work at the Ge/GeO$_2$ interface. We will show that this might also related to the occurrence of valence alternation pairs (VAPs). At low VAP densities, like in the silicon case, hydrogen passivation is feasible, with increasing densities the stabilisation of the dangling bonds prevents the passivation through atomic hydrogen.

This chapter contains the contents of previously published papers [17, 18, 20].

5.1 Charge trapping

To investigate electron (hole) trapping in the GeO structures, we add (remove) electrons to (from) the system and perform complete structural relaxations. Formation energies of the neutral and charged systems were determined as a function of the electron chemical potential. For reference, we first considered the MC models which present a structure analogous to that of substoichiometric silicon oxides. For these models, no charge trapping is observed. The addition of electrons gives extra electrons in the conduction band of the GeO band structure [17], while added holes go to the GeO valence band. The situation is very different for models generated by molecular dynamics, for which we found trapping levels for both electrons and

$$\ce{>Ge^0} + \ce{Ge^0<} \xrightarrow{2e^-} \ce{>Ge^{-1}} \ce{Ge^{-1}<}$$

$$\ce{>Ge^0} + \ce{Ge^n - O^{+1}<} \xrightarrow{2e^-} \ce{>Ge^{-1}} \ce{Ge^n} + \ce{O^0<}$$

$$\ce{>O^0} + \ce{Ge^n - Ge^n} + \ce{O^0<} \xrightarrow{2h^+} \ce{>O^{-1}} \ce{Ge^n} + \ce{Ge^n - O^{+1}<}$$
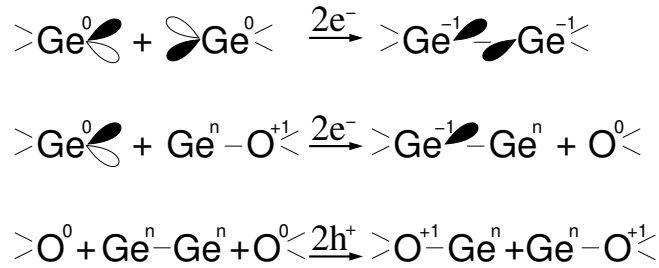
Figure 5.1 – Mechanisms for Ge-Ge bond formation (first and second reactions) and Ge-Ge bond breaking (third) upon electron and hole trapping in GeO, respectively. The superscripts indicate the charge states. The lobes indicate either occupied (filled) or unoccupied (open) dangling bonds. Ge atoms with one occupied dangling bond and one unoccupied dangling bond indicate twofold coordinated Ge atoms.

holes. The addition and removal of a pair of electrons was found to give more stable states than the respective single electron transitions.

The addition of two electrons to the MD model M1 (cf. chapter 4.1) leads to the net formation of a new Ge–Ge bond [17]. Two mechanisms involving twofold coordinated Ge atoms have been observed (Fig. 5.1). In the first mechanism, the two added electrons form a Ge-Ge bond between two nearby twofold coordinated Ge atoms (first reaction in Fig. 5.1). The bond formation results from the overlap between the two unoccupied dangling bonds carried by the twofold coordinated Ge atoms. The second mechanism (observed in MD model M2) involves a twofold and a threefold coordinated Ge atom (second reaction in Fig. 5.1). Also in this case, the net result of the charging process corresponds to a Ge–Ge bond formation. In this process, the threefold coordinated Ge atom is bonded to a threefold coordinated oxygen atom prior to charging. Upon charging the Ge-O bond is broken and a Ge-Ge bond is formed. Similarly, although not explicitly observed in our simulations, one could imagine a Ge–Ge bond formation between two threefold coordinated Ge atoms (reverse of the third reaction in Fig. 5.1).

The removal of two electrons (observed in MD model M1 and M2) causes the breaking of a Ge-Ge bond and the formation of two threefold coordinated O atoms, as illustrated in the third reaction in Fig. 5.1. Thus, it appears that the addition and removal of electrons directly correlates with the number of Ge-Ge bonds. We note that the processes described here involve two-electron transitions and are therefore undetectable by electron-spin resonance. However, single-electron transitions could give transient Ge–Ge bonds with singly occupied bonding orbitals, which correspond to paramagnetic states.

The calculated defect levels $\epsilon(2+/0)$ and $\epsilon(0/2-)$ occur in the GeO band gap. These defect levels are found at 1.3 eV from the GeO valence band and at 0.6 eV from the GeO conduction band. Next, we aligned the GeO band edges to the band edges of GeO_2 as described in chapter 4. The alignment with respect to the Ge band edges could be achieved through the Ge/GeO_2
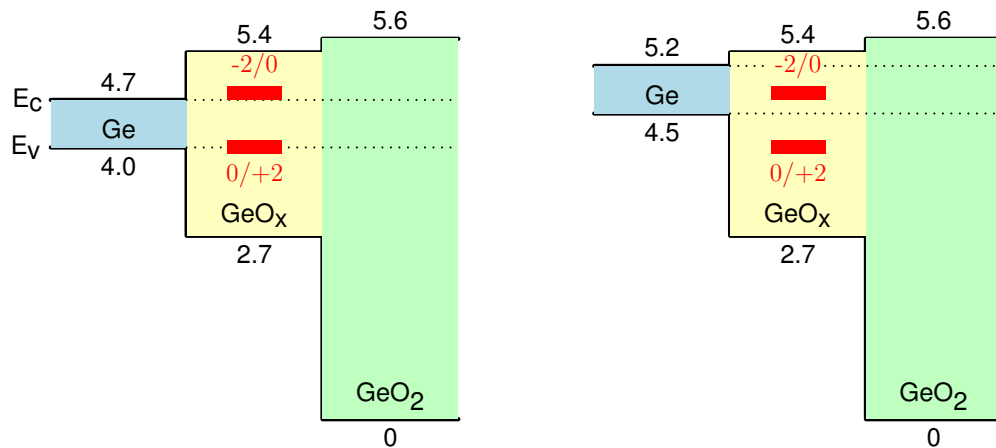
Figure 5.2 – Calculated 0/-2 and 0/+2 charge transition levels corresponding to the trapping of electrons and holes in GeO. The Ge band edges are obtained through the use of experimental values of 4.0 eV [106] (left) and 4.5 eV (right) [119, 158] for the valence band offset of the Ge/GeO$_2$ interface.

band alignment. However, this second step is more problematic because of the large range of experimental values for the band offsets available in the literature. The origin of this variability is unknown but might result from different growth procedures [106, 119, 158]. Oxides grown by thermal O$_2$ oxidation yield a valence band offset of 4.0 eV [106], while valence band offset values close to 4.5 eV have been reported for samples grown with oxidizing agents such as O$_3$ [119] and atomic O [158]. We therefore discuss our findings considering two different band alignments (Fig. 5.2), corresponding to values of 4.0 eV [106] and 4.5 eV [119, 158] for the valence band offset of the Ge/GeO$_2$ interface.

The location of these trapping levels with respect to the Ge band edges depends on the adopted valence band offset between Ge and GeO$_2$. For a valence band offset of 4.0 eV [106], corresponding to an oxide grown by thermal oxidation, the defect levels fall in the vicinity of the Ge band edges, and the accuracy of our calculations does not allow us to conclude whether these defect states are electrically active. For a valence band offset of 4.5 eV, corresponding to oxidation by ozone [119] or atomic O [158], only the electron trapping level falls within the Ge band gap. The close vicinity of the $\epsilon(0/2-)$ level to the conduction band edge might be at the origin of the experimental difficulties of realizing a working n-type Ge-based device. The hole trapping mechanism is electrically inactive provided the valence band offset is larger than 4.0 eV.
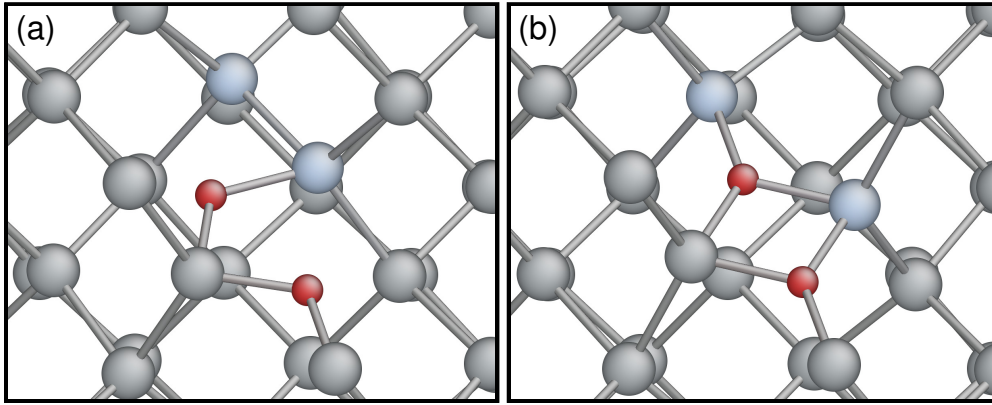
Figure 5.3 – Atomic structure (a) before and (b) after reaction (5.1) in bulk Ge containing two O atoms. Red and grey balls correspond to O and Ge atoms, respectively. Blue balls indicate Ge atoms which undergo a coordination change in the reaction.

5.2 Stability of VAPs accross the interface

Hole trapping through atomistic models

Using various atomistic models showing different O concentrations, we investigate the energetics of the hole trapping reaction,

$$\text{Ge-Ge} + 2\text{h}^+ + 2\Delta E^h \rightarrow 2\text{O}_{\text{III}}^+, \tag{5.1}$$

where h^+ indicates a positively charged hole, O_{III}^+ a threefold coordinated O atom, and ΔE^h the reaction energy cost per involved Ge atom. In writing Eq. (5.1), we adopt the convention that non-explicitly mentioned species on either side of the equation assume regular bonding configurations, viz. O atoms are twofold coordinated with Ge atoms and Ge atoms are fourfold coordinated with O atoms. The case of low O concentration is addressed through a 64-atom model of crystalline germanium, in which two interstitial O atoms have one Ge atom as common nearest neighbor (Fig. 5.3(a)). Upon hole trapping, a nearby Ge-Ge bond breaks and two new Ge-O bonds are formed, giving rise to two O_{III}^+ (Fig. 5.3(b)). For a Fermi level fixed at the valence band edge (*p*-type Ge), our calculations indicate that this reaction proceeds without any energy cost, resulting in a charge transition level that coincides with the valence band edge (Fig. 5.4). For the high O concentration, we used a previously generated model of amorphous GeO_2 model [31], in which we created an O vacancy by omitting one O atom. In the neutral charge state, the formation of a Ge-Ge bond is observed. The removal of two electrons generally causes the system to relax into a structure with two O_{III}^+. The resulting charge transition level occurs at 2.5 eV above the valence band edge of GeO_2. The energy window in Fig. 5.4 results from a statistical study at the semilocal level [116] involving 80 different O vacancies. We also added in Fig. 5.4 the charge transition level corresponding to the intermediate O concentration of GeO, as obtained in the previous section (cf. Fig. 5.2).
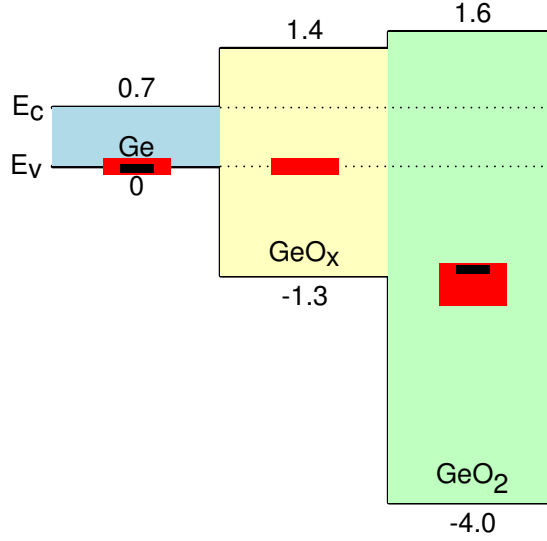
Figure 5.4 – Band diagram of the Ge/GeO$_2$ interface. Charge transition levels as calculated through atomistic models (red) and as estimated through the analysis in elemental steps (black) are indicated. The band structure of GeO is aligned to that of GeO$_2$ through the O $2s$ level [19]. The experimental value of 4 eV [106] is used for the valence band offset between Ge and GeO$_2$. Energies are given in eV.

Hole trapping through a sequence of elemental steps

In this section, we break down the hole trapping reaction in elemental steps. First, we consider the breaking of a Ge-Ge bond into two singly occupied Ge dangling bonds (DB$_{Ge}^0$):

$$\text{Ge-Ge} + 2\Delta E_1 \rightarrow 2\text{DB}_{Ge}^0. \tag{5.2}$$

To estimate the strength of a Ge-Ge bond, we used molecular models as in Ref. [107]. We found that the breaking of a Ge–Ge bond cost 2.50 eV, i.e. $\Delta E_1 = 1.25$ eV. This result is consistent with the experimental value of 3.85 eV for the cohesive energy of germanium [10], from which we infer $\Delta E_1 \sim 1$ eV. Using molecular models as in Ref. [107], we investigated the dependence on the Ge oxidation state finding variations of ΔE_1 of at most $\sim$0.1 eV. We therefore assume in the following that ΔE_1 does not depend on O concentration.

The second elemental step concerns the hole trapping in dangling bonds, resulting in unoccupied dangling bonds (DB$_{Ge}^+$) that are positively charged :

$$2\text{DB}_{Ge}^0 + 2\text{h}^+ + 2\Delta E_2 \rightarrow 2\text{DB}_{Ge}^+. \tag{5.3}$$

Charge transition levels for Ge dangling bonds in Ge were studied previously [27] and can be used to estimate the energy of reaction (5.3) for low O concentrations. The charge transition level $\epsilon(+/0)$ and $\epsilon(0/-)$ of the Ge dangling bond, was found at 0.05 eV and 0.11 eV from the Ge valence band edge, respectively [27]. For p-type Ge, we thus find that reaction (5.3) is
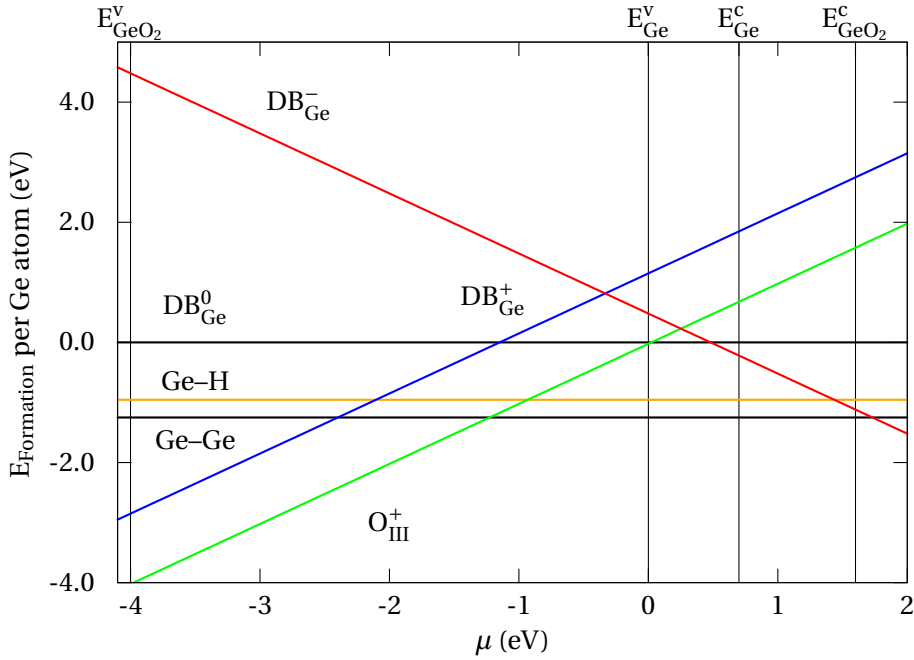
Figure 5.5 – Formation energies vs. electron chemical potential for the Ge dangling bond in α-quartz GeO_2. The formation energies are referred to the respective singly-occupied dangling bonds. The horizontal line labeled Ge-Ge corresponds to the formation energy of a Ge-Ge bond. The formation energy of O_{III}^+ is also shown. The electron chemical potentials are given with respect to the valence band edge in Ge through the band alignment given in Fig. 5.4. The band edges of Ge and GeO_2 are indicated by vertical lines.

exothermic by 0.1 eV, i.e. $\Delta E_2 = -0.05$ eV.

To evaluate the same reaction in the limit of high O concentration, we adopt a model structure of α-quartz GeO_2 relaxed at the density of 3.64 g/cm^3, corresponding to the experimental density of amorphous GeO_2 [155]. Indeed, it has been shown that the electronic structure of such a model is comparable to that of amorphous GeO_2 [31]. We created a Ge dangling bond by first omitting one of the O atoms and by then flipping one of the Ge atoms across the plane of its three O neighbors prior to passivation with hydrogen. For the remaining dangling bond, we calculated relative formation energies in three different charge states (Fig. 5.5). To estimate the energy of reaction (5.3), we aligned the band structure of GeO_2 to that of Ge using the experimental valence band offset of 4 eV [106]. For a Fermi level fixed at the Ge valence band edge, reaction (5.3) is then endothermic by 2.3 eV, i.e. $\Delta E_2 = 1.15$ eV.

The third elemental step concerns the stabilization of an unoccupied Ge dangling bond which forms a bond with a regularly bonded twofold-coordinated O atom giving rise to an O_{III}^+:

$$2DB_{Ge}^+ + 2\Delta E_3 \rightarrow 2O_{III}^+ \tag{5.4}$$

Table 5.1 – Energies ΔE_1, ΔE_2, and ΔE_3 associated to the elemental reactions (see definitions in text) leading to charge trapping in Ge and in GeO$_2$, together with the total reaction energy $\Delta E^h = \Delta E_1 + \Delta E_2 + \Delta E_3$ and the corresponding charge transition level $\varepsilon(+/0)$ referred to the valence band edge of Ge. The Fermi level is set at the valence band edge of Ge. Energies are given in eV.

	ΔE_1	ΔE_2	ΔE_3	ΔE^h	$\varepsilon(+/0)$
Ge	1.25	−0.05	−1.17	0.03	−0.03
GeO$_2$	1.25	1.15	−1.17	1.23	−1.23

Table 5.2 – Energy ΔE^e associated to the electron trapping reaction in Ge and GeO$_2$ for Fermi levels set at the conduction band edge (CBE) and at the valence band edge (VBE) of germanium, corresponding to n-type and p-type germanium, respectively. ΔE^e is obtained from the sum of elemental reaction energies ΔE_1 and ΔE_4 (see definitions in text). The associated $0/-$ charge transition level $\varepsilon(0/-)$ referred to the VBE is also given. Energies are given in eV.

	ε_F	ΔE_1	ΔE_4	ΔE^e	$\varepsilon(0/-)$
Ge	CBE	1.25	−0.59	0.66	1.36
GeO$_2$	CBE	1.25	−0.22	1.03	1.73
Ge	VBE	1.25	0.11	1.36	1.36
GeO$_2$	VBE	1.25	0.48	1.73	1.73

To estimate the energy of this reaction, we again have recourse to α-quartz with an O vacancy. The two Ge atoms facing the vacancy are not equivalent by symmetry. Depending on the Ge atom, the flipping of the Ge atom across the plane of its O neighbors either leads to an isolated dangling bond or to an O$_{\mathrm{III}}^+$ in the positive charge state [21], the other Ge atom being passivated with hydrogen. Through energy differences, we derive a stabilization energy of 2.34 eV for reaction (5.4), i.e. $\Delta E_3 = −1.17$ eV (cf. Fig. 5.5). This value is consistent with a previous study of protons at Si/SiO$_2$ interfaces, where a stabilization of ~1 eV was found upon the formation of O$_{\mathrm{III}}^+$ [60]. Since reaction (5.4) is dominated by the formation of a chemical bond, we assume it does not depend on O concentration.

The energies associated to the three elemental reactions are summarized in Table 5.1 and the corresponding charge transition levels for the total reaction (5.1) have been added in Fig. 5.4. We note that at low O concentrations the hole trapping reaction can occur without implying any energy cost. On the contrary, the reaction is disfavored in the stoichiometric oxide. The charge transition levels resulting from this analysis correspond closely to those calculated for the atomistic models, lending support to the energies derived for the individual elemental reactions.

Table 5.3 – Energy ΔE^{VAP} associated to the formation of a valence alternation pair in Ge and GeO$_2$. ΔE^e is obtained from a sum of elemental reaction energies as given in Eq. (5.8). ΔE^{VAP} does not depend on Fermi level. Energies are given in eV.

	$2\Delta E_1$	$\Delta E_2 + \Delta E_4$	ΔE_3	ΔE^{VAP}
Ge	2.50	0.06	−1.17	1.39
GeO$_2$	2.50	1.63	−1.17	2.96

Electron trapping

Relying on the energies of the elemental reactions identified in the previous section, we now estimate the energy associated to the electron trapping reaction:

$$\text{Ge-Ge} + 2\text{e}^- + 2\Delta E^e \rightarrow 2\text{DB}_{\text{Ge}}^-. \tag{5.5}$$

The reaction energy can be obtained by considering the breaking of a Ge-Ge bond (5.2), followed by the electron charging of a singly occupied Ge dangling bond:

$$2\text{DB}_{\text{Ge}}^0 + 2\text{e}^- + 2\Delta E_4 \rightarrow 2\text{DB}_{\text{Ge}}^-. \tag{5.6}$$

The respective energies are summarized in Table 5.2 for both n-type and p-type germanium. The energy values found for ΔE^e indicate that reaction (5.5) is not convenient at the Ge/GeO$_2$ interface. The corresponding charge transition levels $\varepsilon(0/-)$ occur above the conduction band edge of germanium.

Stability of valence alternation pairs

By combining reactions (5.1) and (5.5), we obtain

$$\text{Ge-Ge} + \Delta E^{\text{VAP}} \rightarrow \text{O}_{\text{III}}^+ + \text{DB}_{\text{Ge}}^- \tag{5.7}$$
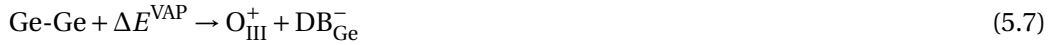
which corresponds to the breaking of a Ge-Ge bond in favor of the formation of a valence alternation pair consisting of a doubly occupied dangling bond and a threefold coordinated O atom, as observed in molecular dynamics simulations of GeO$_x$ [17]. The reaction energy can be obtained from the elemental reaction energies as follows:

$$\Delta E^{\text{VAP}} = 2\Delta E_1 + \Delta E_2 + \Delta E_3 + \Delta E_4. \tag{5.8}$$

Since this reaction does not involve any charge variation, its energy ΔE^{VAP} does not depend on Fermi level.

The energies for the formation of a valence alternation pair in Ge and in GeO$_2$ together

with their decomposition in elemental contributions are given in Table 5.3. The calculated values indicate that the formation of a valence alternation pair starting from a Ge–Ge bond is unfavorable both in Ge and in GeO_2. However, the involved energy cost in Ge is considerably lower than in GeO_2. The lowest energy cost for the formation of a valence alternation pair at the Ge/GeO_2 interface is estimated to be 1.4 eV. As can be seen in Table 5.3, this value mainly results from the cost of breaking of a Ge-Ge bond ($2\Delta E_1 = 2.50$ eV) and from the subsequent energy gain associated to the formation of an O_{III}^+ ($\Delta E_3 = -1.17$ eV).

This energy estimate has to be confronted with other computational results. In chapter 4, a molecular dynamics simulation revealed a structure of GeO_x with more than half of the atoms participating in valence alternation pairs, giving rise to a structure composed primarily of threefold coordinated Ge and O atoms. It was further shown that the total energy of this structure was competitive with alternative structures for GeO_x in which all Ge atoms are fourfold coordinated and all O atoms are twofold coordinated [17, 19]. Moreover, we show in chapter 6, a valence alternation pair created in the proximity of the Ge/GeO_2 interface. The cost for the creation of this valence alternation pair was found to be 0.45 eV [33], considerably lower than the estimates achieved with our present analysis.

These comparisons suggest that the present estimate of 1.4 eV might be excessively high. There are several reasons that could be invoked for this. Our analysis mainly rests on the description of chemical energies and might not account properly for strain effects. For instance, we took the Ge–Ge bond energy from a fully relaxed molecule, finding an energy which likely overestimates the stability of a strained Ge–Ge bond at the Ge/GeO_2 interface. [1] Furthermore, the stabilization energy used for the O_{III}^+ is taken from an α-quartz GeO_2 model in which the atoms around the O_{III}^+ cannot relax fully [21], as would be the case in the amorphous environment of GeO_x. While the creation of a valence alternation pair preserves the overall number bonds, the structural organization of the network is severely modified and might give global strain effects which are not captured by our analysis. In addition, our analysis provides estimates for the creation of isolated charges, but does not account for the electrostatic energy resulting from the interaction between the positively and negatively charged moieties of the valence alternation pair. Assuming a dielectric constant of 10 for GeO_x and a separation of 10 bohr between the charged moieties, we estimate an interaction energy of 0.3 eV, which further stabilizes the valence alternation pair.

5.3 Hydrogen passivation

Dangling bond defects disturb the performance of electrical devices. At the Si/SiO_2 interface, Si dangling bonds are generated through the lattice mismatch between Si and its native oxide. Hydrogen is used to passivate the Si dangling bonds [38, 136]. For the Ge/GeO_2 interface, it is not clear whether hydrogen can reduce the number of electrically active defects [1, 99, 3].

---

1. Using an α-quartz model with an O vacancy, we obtain an estimate of ~ 2 eV for the Ge–Ge bond

First, we study H passivation of a Ge dangling bond in GeO_2. We use the Ge dangling bond model of the previous section and passivate the dangling bond with a H atom. The resulting formation energy is added in Fig. 5.5.

The formation energy depends on the charge carried by the Ge dangling bond. Coming from the neutral charge state, one gains ~ 1 eV through H passivation. Coming from the negatively charged dangling bond, the gain depends on the Fermi level μ. For $\mu = E_{Ge}^{v}$, the gain is 0.48 eV larger than ~ 1 eV, while for $\mu = E_{Ge}^{c}$ the gain is 0.22 eV smaller (cf. ΔE_4 in Tab. 5.2). In all cases, the passivation with H stabilizes the Ge dangling bond. The achieved energy gain is similar to the formation of a Ge–Ge bond (ΔE_1). This is also similar to the dangling bond passivation in Si [29].

We further created a valence alternation pair in one of our regularly bonded GeO structures obtained by Monte Carlo bond switching. This was done by breaking a Ge–Ge bond and switching one of the Ge atoms across the plane of its three O neighbors, where it formed a new Ge–O bond with a twofold coordinated O atom. Using hybrid functionals and the alignment scheme of chapter 4 with a valence band offset of 4.0 eV between Ge and GeO_2 and $\mu = E_{Ge}^{v}$, we obtained a formation energy of -0.7 eV for H^+ passivation. This indicates, that dangling bond passivation is energetically favoured for all electron chemical potentials inside the band gap of Ge. We obtain a similar picture for dangling bonds in GeO_2 and in regularly bonded GeO obtained by Monte Carlo bond switching.

Next, we study the energetics of dangling bond passivation with H in our GeO model structure generated via molecular dynamics. Since Ge dangling bonds are always negatively charged, we study the passivation through the addition of a proton (H^+). First, we place the H^+ at the position of a Ge related WFC (see chapter 4) and relax the Ge–H bond length. Then, we allow all atoms to optimize their positions. Because of the large number of undercoordinated Ge atoms, the structure is flexible and can easily reorganize its bonds locally. To determine formation energies, it is necessary that the structure switches between two given configurations upon H addition/removal. To achieve such a situation, the H is added and removed in a sequential manner until the formation energy could be properly defined [37]. The configuration with the lowest formation energy is represented through a reaction where the Ge dangling bond is passivated with the H^+. A negatively charged Ge dangling bond is passivated through a H^+ and becomes charge neutral. To evaluate the formation energies for reasonable Fermi levels, we perform calculations at the hybrid functional level for the most favourable case, and align the Ge valence band through the experimental valence band offset of 4.0 eV. The other formation energies are aligned to this value preserving the energy differences found at the semilocal level. Figure 5.6 shows the normalized formation energy spectrum for the Fermi level at the valence band edge of germanium ($\mu = 0$). The formation energy increases with μ reaching values which are higher by ~ 0.7 eV than those in Fig. 5.6 when μ attains the conduction band edge. In the MD structure, the passivation of a Ge-DB through a H^+ and the formation of a Ge–H bond is not favoured for μ inside the band gap of Ge (cf. Fig. 5.6, red line), in agreement with experiment [1]. We also considered other locations for H^+ in our GeO model. When the
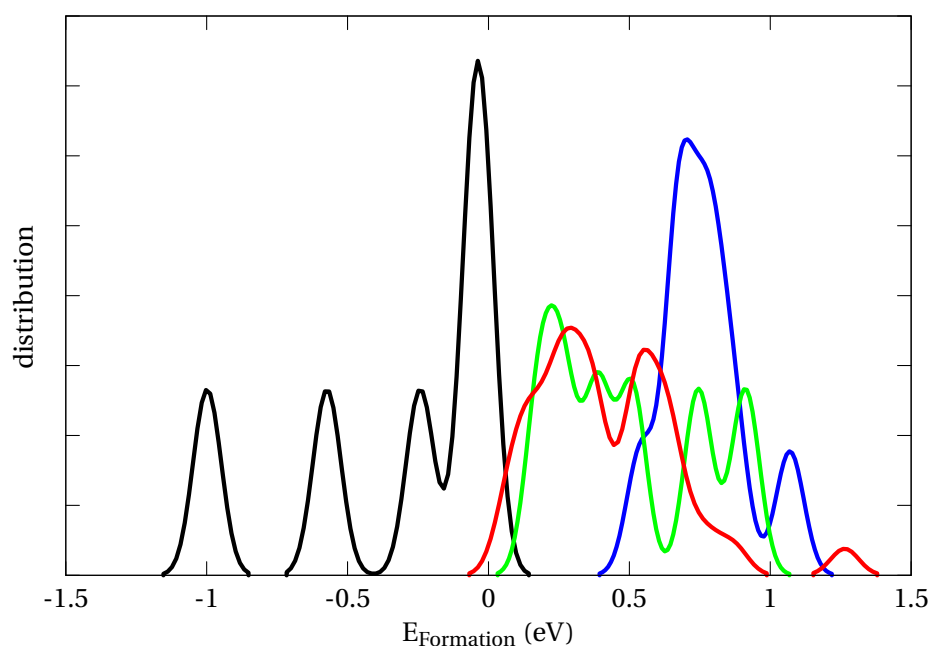
Figure 5.6 – Distribution of formation energies for a proton in different positions in substo-ichiometric GeO generated via MD (black line at a twofold O atom, red line at a threefold coordinated Ge dangling bond, green line at a twofold coordinated Ge atom, and blue line at the center of a Ge–Ge bond). The energy distribution is obtained through semilocal function-als. The energy alignment is done through a determination of formation energies at a hybrid density functional level for two selected cases. Through the O $2s$ level, the GeO band edges are align to those of GeO_2. The band gap of Ge is aligned through the experimental valence band offset of 4.0 eV.

H^+ is positioned close to twofold coordinated Ge atoms (green line), the formation energies (cf. 5.6) are similar to those obtained for threefold coordinated Ge atoms (red line). The H^+ inside a Ge–Ge bond is less favoured by 0.5 eV (blue line).

Furthermore, we considered H^+ positions close to twofold coordinated O atoms. Following the same procedure as for the Ge-DB passivation, we get formation energies which are favoured over the whole Fermi level region (cf. Fig. 5.6 black line). In this case, neutral twofold coor-dinated O atoms transforms to Ge–O–H complexes and the hole gets trapped on a threefold coordinated O atom.

When neutral H is considered, the process can be decomposed in the passivation by a H^+ as discussed above and in the charging of the system with an extra electron. As we discussed in the beginning of this chapter 5.1. Figure 5.7 shows the charge transition levels for this process. Since, the process is neutral, it does not depend on Fermi level and is also independent of the adopted VBOs. The blue lines show the two limits given by the energy distribution of the H^+ attached to a twofold coordinated O atom (black distribution in Fig. 5.6). The red line shows the charge transition level from electron trapping as studied in chapter 5.1. The formation
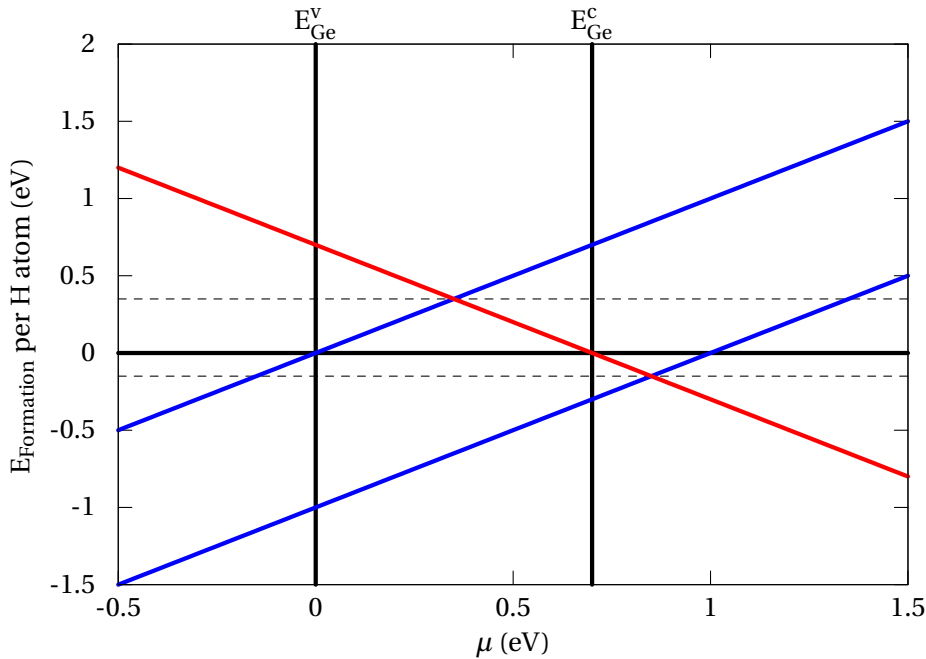
Figure 5.7 – Hydrogen interaction with GeO. The charge transition levels for proton trapping correspond to the OH formation in Fig. 5.6. The electron trapping level is taken from chapter 5.1. The formation energy of a neutral H atom is obtained by considering separately those of the proton H^+ and of an additional electron e^-.

energy for the combined process can be obtained by summing up the negative and positive charge transition levels. This is indicated by the two dashed horizontal lines. The line slightly below the reference level would allow the interaction with H through the discussed process. However, the energy gain is small. In almost all cases H passivation is not favoured when a GeO structure with VAPs is considered.

5.4 Conclusion

We determined the energy levels of electron and hole trapping in the substoichiometric germanium oxide at the Ge/GeO_2 interface. These trapping states correspond to the formation and breaking of Ge-Ge bonds.

We studied the stability of valence alternation pairs in comparison to Ge-Ge bonds for various O concentrations occurring across the Ge/GeO_2 interface. In our analysis, hole and electron trapping are considered separately. We found that, at low O concentrations, hole trapping proceeds at essentially no energy cost for p-type germanium, mainly because of the energy gain due to the formation of threefold coordinated O atoms. At variance, electron trapping is found to be unfavorable in all circumstances. The present analysis leads to an estimate of 1.4 eV for the formation energy of a valence alternation pair, which likely corresponds to an

overestimation because strain and electrostatic effects are neglected.

Furthermore, we studied the interaction of H atoms with GeO_x. We found passivation mechanisms similar to the silicon counterpart, when a silicon like bond structure is considered. With increasing number of valence alternation pairs, the passivation mechanism changes, and the formation of Ge–O–H bonds is favoured. This mechanism is not able to reduce the defect density at the Ge/GeO_2 interface. Further studies are needed to get a better understanding of H at the Ge/GeO_2 interface.

6 The Ge/GeO$_2$ interface

In this chapter we investigate the valence band offset (VBO) of the Ge/GeO$_2$ interface. First, we generate an atomistic Ge/GeO$_2$ interface model structure by rescaling the topology of a previously generated model structure of the Si/SiO$_2$ interface. The constructed interface model shows a smooth transition region where all Ge atoms are fourfold coordinated and all O atoms are twofold coordinated. The structural parameters agree corresponds very well with experimental values. The calculated VBO is found to be significantly smaller than experimental VBOs. Next, we study the effect of valence alternation pairs (VAPs) on the VBO. We modify the interface structure and generate a VAP in the interfacial region of the Ge/GeO$_2$ interface. Then, we determine the interface dipole as well as the VBO. The presence of VAPs lead to a decrease of the interface dipole and to an ensuing increase of the VBO.

This chapter contains the contents of previously published papers [30, 31, 34, 33].

6.1 Structural properties

For the interface model, we adopted a 217-atom superlattice model of the Si/SiO$_2$ interface generated previously [58, 24, 23] and replaced Si with Ge. The $\sqrt{8} \times \sqrt{8}$ interfacial repeat unit was rescaled to match the equilibrium lattice constant of Ge (5.76 Å) [27], and a structural relaxation of the atomic positions was carried out. This procedure results in an oxide density of ~3.5 g/cm^3 in the middle of the oxide layer, in good agreement with the experimental density of 3.6 g/cm^3 of vitreous GeO$_2$ [155]. The connection between Ge and GeO$_2$ is achieved through a substoichiometric oxide region of 6 Å.

Our model interface is illustrated in Fig. 6.1. Ge-Ge and Ge-O bond lengths as they evolve across the interface are shown in Figure 6.2(a). We report Ge-Ge distances corresponding to nearest Ge atoms, which correspond to next nearest neighbors in the oxide. In the central part of the oxide layer, the average Ge-O bond length is found to be 1.78 ± 0.02 Å, to be compared with the experimentally measured value of 1.73 Å for vitreous GeO$_2$ [128] (cf. Table 6.1). In Fig. 6.2(b), the average O-Ge-O and Ge-O-Ge bond angles are given as they evolve
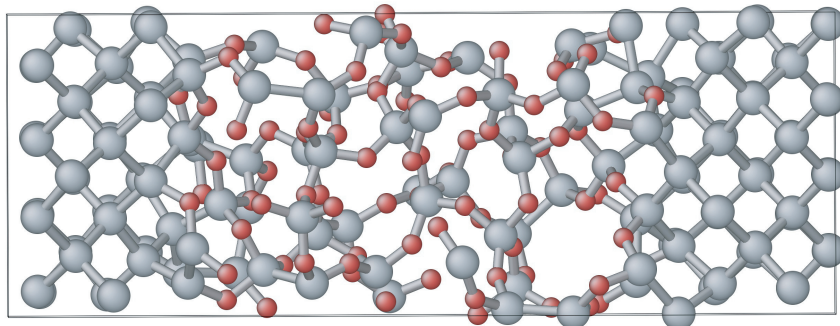
Figure 6.1 – Ball-and-stick model of the Ge-GeO$_2$ interface. Red balls are indicating oxygen atoms and grey balls are indicating germanium atoms.
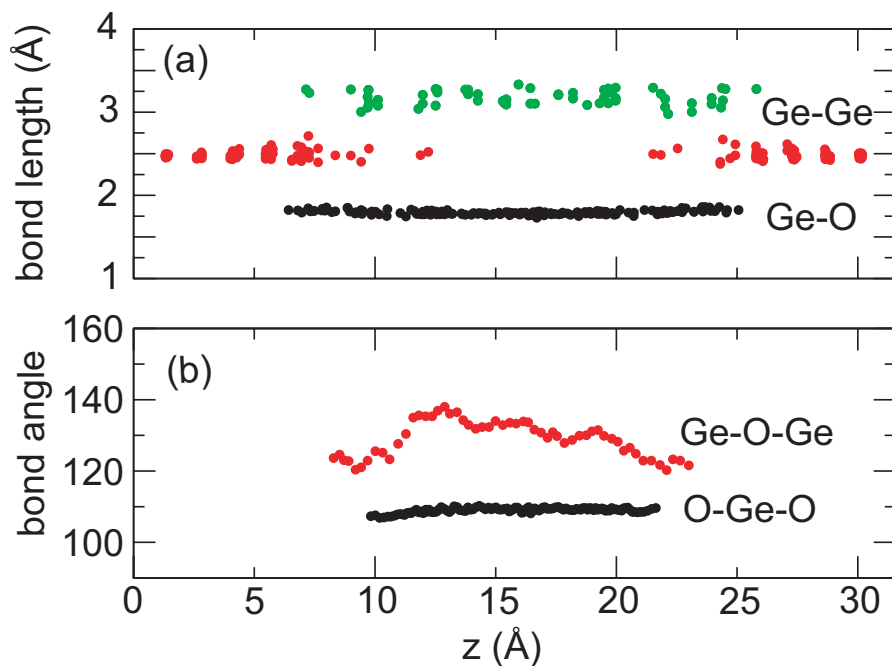

Figure 6.2 – (a) Ge-Ge bond lengths (red), next-nearest neighbor Ge-Ge distances (green), and Ge-O bond lengths (black) across the Ge-GeO$_2$ interface. (b) Average O-Ge-O (black) and Ge-O-Ge (red) bond angles across the Ge-GeO$_2$ interface.

Table 6.1 – Mass density (ρ), bond length (d_{GeO}), and bond angles for amorphous GeO$_2$ in the bulk and interface models, compared to experimental values. Experimental values for the density, bond lengths, and bond angles are taken from Refs. [155], [128], and [125], respectively.

	Bulk	Interface	Expt.
ρ (g/cm^3)	3.6	3.5	3.6
d_{GeO} (Å)	1.76 ± 0.05	1.76 ± 0.05	1.73
$\angle$ O-Ge-O	$109° \pm 5°$	$109° \pm 3°$	$109.4°$
$\angle$ Ge-O-Ge	$133° \pm 10°$	$133° \pm 7°$	$133°$

across the interface. In the central part of the oxide layer, the distributions of these angles are characterized by values of $109.6° \pm 9.2°$ and $131° \pm 7.0°$, respectively. The average O-Ge-O angles, which characterize the tetrahedra centred on Ge atoms, are found to be rather constant throughout the oxide and do not indicate any significant variation in the close vicinity of the interface. The Ge-O-Ge angle describes the connection between tetrahedra and therefore the medium-range correlations in the oxide [55]. This bond angle is found to be slightly smaller in the transition region than in the middle of the oxide layer, cf. Fig. 6.2(b). The average Ge-O-Ge angle found in the central part of the oxide layer is close to values for vitreous GeO$_2$ derived from diffraction data ($133°$, [125]) or inferred from the analysis of Raman spectra ($135°$, [55]). Furthermore, the structural parameters of the oxide component are also in good agreement with those of an amorphous GeO$_2$ model generated through molecular dynamics (cf. chapter 4) (Table 6.1). Hence, we infer that our interface model provides a smooth structural transition between crystalline germanium and amorphous GeO$_2$.

6.2 Band offsets at the Ge/GeO$_2$ interface

The alignment scheme used to obtain the valence band offset at the Ge/GeO$_2$ interface, requires representative bulk models of the two main interface compounds. For bulk GeO$_2$, we considered both crystalline and amorphous structures. A quartz structure was fully relaxed, resulting in lattice parameters exceeding experimental values by only 2%. As the density of quartz-like GeO$_2$ (4.3 g/cm^3) differs significantly from that of the amorphous oxide (3.6 g/cm^3) [155], we also searched for a crystalline structure of lower density. We rescaled the lattice parameters of the quartz structure to match the density of the amorphous oxide prior to the structural relaxation. In this way, we achieved a locally stable quartz-like structure with a density of 3.5 g/cm^3.

We also used amorphous GeO$_2$ structure modeled through *ab initio* molecular dynamics. A 126-atom model with a density fixed at the experimental value of 3.6 g/cm^3 was generated. The structural properties of this model were given in Tab. 6.1 and in chapter 4.

For the three bulk models of GeO$_2$, the electronic densities of states were calculated at the
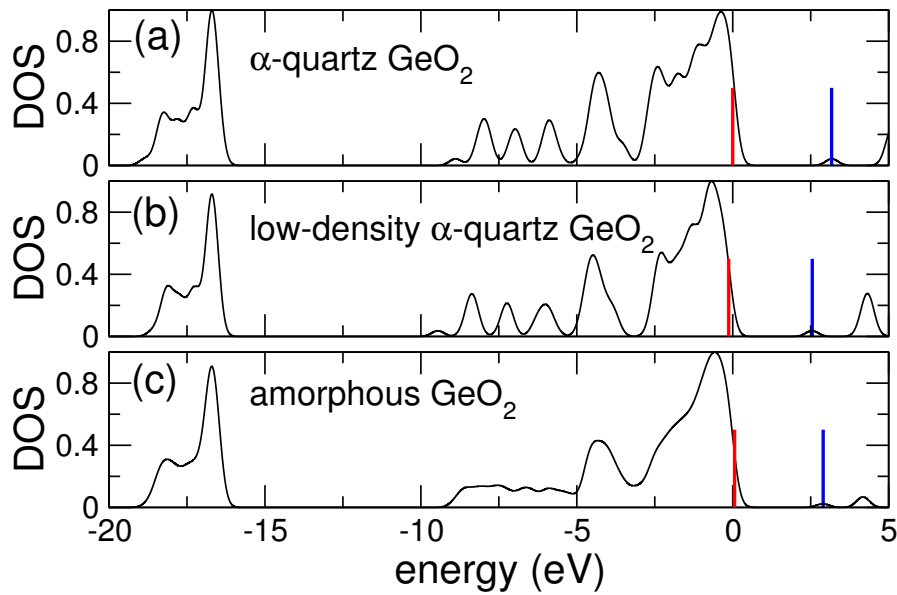
Figure 6.3 – Electronic density of states (DOS) of GeO$_2$: (a) quartz structure, (b) low-density quartz-like structure, (c) amorphous GeO$_2$. The energy is referred to the valence band maximum of the quartz structure. The other scales are aligned through the O 2s states. The band edges are marked. A Gaussian broadening of 0.2 eV was used.

PBE level of theory (cf. Fig. 6.3). The spectra of the different models were aligned through the deep O 2s states, which are assumed to be least affected by density variations and structural disorder (cf. chapter 4.3). For quartz GeO$_2$, our calculations gave a band gap of 3.2 eV [Fig. 6.3(a)]. For the low-density quartz-like structure, the calculated band gap reduced to 2.7 eV [Fig. 6.3(b)]. For the amorphous model, we found a band gap of 2.8 eV. The band gap reduction by ~0.4 eV with respect to quartz GeO$_2$ is consistent with both experimental observations [86] and previous calculations [138]. From the comparison in Fig. 6.3, it appears clearly that band gap variations mainly originate from shifts of the conduction band minima. Irrespective of the considered model, the valence band maximum is found at the same energy within 0.1 eV, suggesting that this level is not affected by the indetermination of the oxide structure.

We derived the evolution of the band edges across the semiconductor-oxide interface from the local electronic density of states within the PBE scheme (Fig. 6.4). The band edges are determined by integrating the broadened local density of states up to a threshold value, which recovers the correct band edges for bulk GeO$_2$ (cf. Ref. [48]). On the semiconductor side, we obtained a band gap of 0.4 eV. We checked that the origin of the band gap opening results from the quantum confinement due to the finite thickness of the Ge layer rather than from the finite **k**-point sampling used in the interface model [59]. In the oxide component, we obtained a band gap of 2.6 eV, close to the band gap of the bulk model (2.8 eV). Such small differences are typical for finite-size amorphous models and should be attributed to the structural disorder [55]. The transition region extends over ~6 Å and is mainly determined by the evolution of the
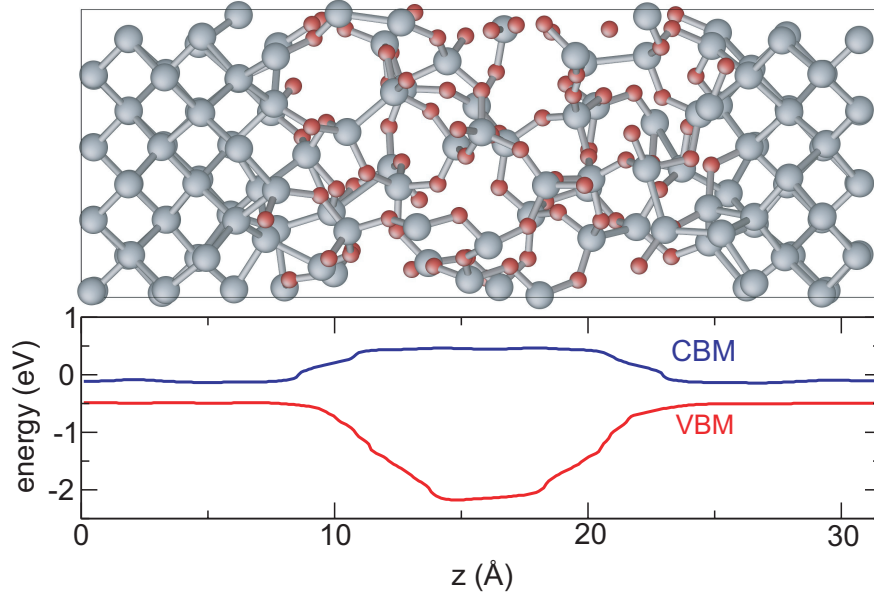
Figure 6.4 – Evolution of the valence band maximum (VBM) and conduction band minimum (CBM) along a direction orthogonal to the interface plane (bottom), obtained at the PBE level.

Table 6.2 – Band gaps of Ge (E_g^{Ge}) and amorphous GeO$_2$ ($E_g^{GeO_2}$), and valence (ΔE_v) and conduction (ΔE_c) band offsets at the Ge/GeO$_2$ interface, calculated at the PBE level, at the PBE0 level, and through the use of the mixed scheme (Ref. [26, 5]). Energies are given in eV.

	E_g^{Ge}	$E_g^{GeO_2}$	ΔE_v	ΔE_c
PBE	0	2.8	2.0	0.8
PBE0	1.2	5.6	3.1	1.3
Mixed	0.74	5.6	3.4	1.5

valence band maximum. To extract reliable offsets from our calculations, we aligned the bulk band edges of the interface components through a reference potential calculated across the interface [145]. As reference potential, we used the local potential in germanium and the deep O 2s states in the oxide. In the PBE scheme, this gave a valence band offset of 2.0 eV (Table 6.2), in fair agreement with a previous calculation (1.8 eV) [72]. However, this result suffers from the band gap underestimation of semilocal density functionals [132, 5].

To overcome this limitation, we turned to hybrid density functionals. We first used the PBE0 functional which corresponds to a fraction of Hartree-Fock exchange $\alpha = 0.25$ [117]. Applying the same procedure as in the PBE scheme, we obtained a valence band offset of 3.5 eV (Table 6.2), significantly larger than in the PBE (2.0 eV). The PBE0 scheme overestimates the band gap of germanium (1.2 eV vs 0.74 eV), but provides a good estimate for the band gap of GeO$_2$. Hence, it is not possible to describe the band gaps of the two interface components through

the use of single hybrid density functional.

We therefore also calculated the band offsets through a mixed scheme, which reproduces the experimental band gaps of the two interface components and which has provided a good description of various semiconductor-oxide systems [5, 26]. For each interface component, the scheme consists in determining the optimal fraction α of Hartree-Fock exchange that brings the calculated band gap in accord with the experimental one. For germanium, we used $\alpha = 0.15$ which gives a band gap of 0.74 eV (Table 6.2, cf. Ref. [27]). For GeO$_2$, we used $\alpha = 0.25$ (PBE0). We determined the latter value by matching the band gap of quartz GeO$_2$ (6 eV, Ref. [86]), which is not subject to structural ambiguity. For this value of α, the calculated band gap of our amorphous GeO$_2$ model is 5.6 eV (Table 6.2), in very good agreement with experimental observations (5.6 eV) [86]. The scheme further relies on the fact that the offset between the local potentials on each side of the interface only weakly depends on the fraction α [5]. For our interface model, we found that this offset varies by less than 0.2 eV when going from PBE to PBE0. For the alignment, we used the offset pertaining to the intermediate $\alpha = 0.2$ [5]. Thus, for α's varying within the window between 0.15 (pertaining to Ge) and 0.25 (pertaining to GeO$_2$), the residual ambiguity is about ± 0.05 eV, which should be taken as the intrinsic error of the calculated band offset [5]. The mixed scheme gives a valence band offset between germanium and amorphous GeO$_2$ of 3.4 eV, which is slightly smaller than experimental values(3.6–4.5 eV) [106, 97, 119]. Our results are given in Table 6.2.

6.3   Valence alternation pairs

In this part, we investigate to what extent different bonding patterns at Ge/GeO$_2$ interfaces could account for the large variation of measured band offsets. In particular, we consider the role of valence alternation pairs (VAPs) [76] which have been suggested to occur intrinsically in substoichiometric germanium oxide (cf. chapter 4 and chapter 5. These pairs consist of charged moieties, viz. positively charged threefold-coordinated O atoms and negatively charged Ge dangling bonds, and could therefore significantly contribute to the interface dipole.

A new model is required to get extra flexibility which allows the formation of a VAP through bond switching. As an initial model structure, we constructed a 172-atom slab model of the Ge/GeO$_2$ interface on the basis of a superlattice structure introduced in chapter 6.1. The termination of the slab structure was achieved by hydrogen saturation. In this model, the transition from Ge to amorphous GeO$_2$ occurs through a substoichiometric region of 6 Å. In the directions parallel to the interface plane, the model shows a repeat unit of 11.5 Å × 11.5 Å. In this model, all the Ge atoms are fourfold coordinated and all the O atoms are twofold coordinated. The structural and electronic properties of the interface are in good agreement with those of the original superlattice model (cf. chapter 6.1). The model interface is illustrated in Fig. 6.5(a), where the atomic coordination numbers are indicated by a color code.

For comparison, we also considered a Ge/GeO$_2$ interface with a crystalline oxide phase [108,

Table 6.3 – Calculated valence band offsets for model structures of the Ge/GeO$_2$ interface without and with a valence alternation pair (VAP), as calculated at the PBE level, at the PBE0 level, and within a mixed hybrid-functional scheme [5]. The interface models involve either amorphous or crystalline oxide phases.

Ge/GeO$_2$ interface	PBE (eV)	PBE0 (eV)	Mixed (eV)
without VAP			
Amorphous oxide	2.2	3.2	3.5
Crystalline oxide	2.1	3.2	3.5
model chapter 6.2	2.0	3.1	3.4
with VAP			
Amorphous oxide	2.9	3.9	4.2

112, 111]. We adopted model I of Ref. [111] showing an oxide layer in the tridymite phase. The lattice was rescaled to fit the germanium lattice constant and a full optimization of the ionic positions was carried out. The system consists of a slab model comprising 92 atoms, with an interfacial repeat unit of 2×2 substrate Ge atoms. The bond-density reduction across the interface occurs via a suboxide region of ~5 Å in which all Ge atoms are fourfold coordinated and all O atoms are twofold coordinated. The slab extrema were terminated by hydrogen atoms.

To calculate band offsets, we also need bulk structures of the interface components. For this, we rely on models of Ge and amorphous GeO$_2$ described in chapter 6.2

Band offsets

Before discussing the results, we conceptually describe the procedure for obtaining band offsets at the interface between two materials [145]. The band offsets can be determined by aligning the bulk band structures of the interface components to a reference potential that varies across the interface. Thus, when different interface structures are considered, only the variation of the offset of the reference potential affects the change in the determined band offsets. These changes result from variations in the interface dipole.

In our density-functional calculation of the interface, we therefore monitored the offset of the local electrostatic potential to evidence variations in the interface dipole. The evolution of the local electrostatic potential across the interface model showing an amorphous oxide without VAP is given in Fig. 6.6(a). Despite the amorphous nature of the oxide, one clearly observes the offset across the interface. The offset originates from differences in electronegativity between Ge and O atoms causing a charge polarization within the Ge-O bonds at the interface. As a result, the Ge atoms become positively charged and the O atoms become negatively charged, as illustrated schematically in Fig. 6.7.
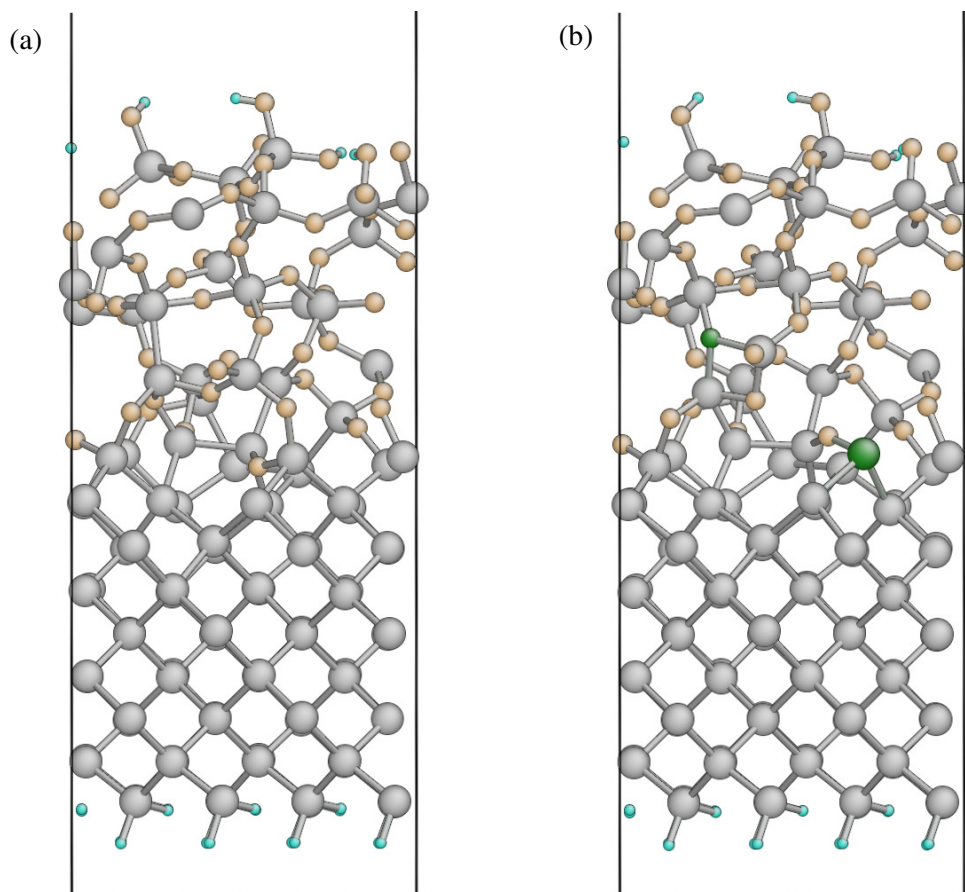
Figure 6.5 – Ball and stick models of the Ge/GeO$_2$ interface structures showing an amorphous oxide, (a) without and (b) with a valence alternation pair. Grey balls are fourfold coordinated Ge atoms and white balls are twofold coordinated O atoms. The smaller and the larger green balls correspond to a threefold coordinated O atom and to a threefold coordinated Ge atom carrying a doubly occupied dangling bond, respectively. The small turquoise balls correspond to the terminating hydrogen atoms. We used cutoff distances of 2.8 Å and 2.2 Å for Ge-Ge and Ge-O bonds, respectively.
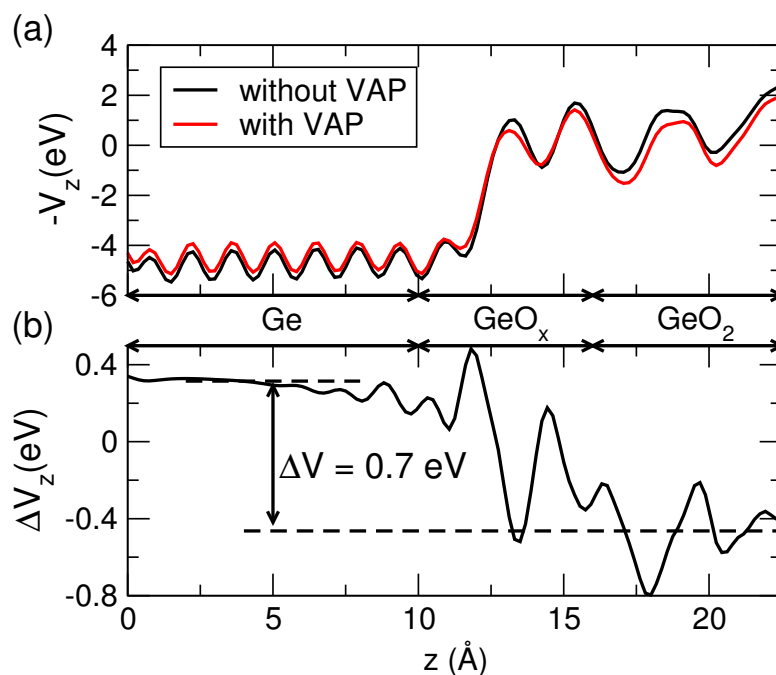
Figure 6.6 – (a) Planar-averaged local electrostatic potential across the interface for the Ge/GeO$_2$ model showing an amorphous oxide, without (black) and with (red) a valence alternation pair (VAP). (b) Difference between the local electrostatic potentials in the two models, ΔV.

From the offset of the local electrostatic potential, we calculated the valence band offset for the Ge/GeO$_2$ model interface showing an amorphous oxide. At the PBE level, we obtained a value of 2.2 eV, in good agreement with previous semilocal density functional calculations [72, 31, 30]. The calculated value for the valence band offset increases to 3.2 eV at the PBE0 level of theory. However, while the band gap of GeO$_2$ is well described at the PBE0 level, that of Ge is overestimated by 0.5 eV [31]. We therefore had recourse to the mixed hybrid-functional scheme to evaluate band offsets [26, 5].

The results obtained with the various functionals and with the mixed scheme are given in Table 6.3. In the following, the discussion is based on the values obtained in the mixed scheme, which are considered most reliable.

Within the mixed scheme, we calculated a valence band offset of 3.5 eV for the present slab model of the Ge/GeO$_2$ interface showing an amorphous oxide, in very good agreement with the previously reported value of 3.4 eV for its parent superlattice model (cf. chapter 6.2). For the Ge/GeO$_2$ interface with a crystalline oxide component, we calculated a band offset of 3.5 eV. Thus, to the extent that all the Ge atoms and all the O atoms are fourfold and twofold coordinated, respectively, the interface dipole density is constrained by the experimental mass densities of the two interface components and the offset of the local electrostatic potential undergoes only minor variations for different interfacial bonding patterns. This observation
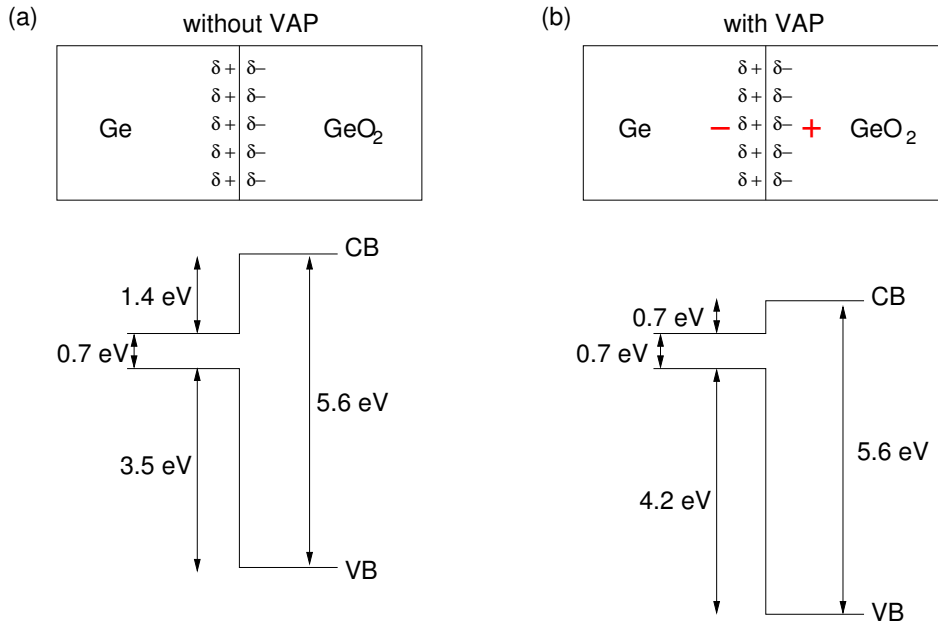
Figure 6.7 – Band diagrams for the Ge/GeO$_2$ interface model showing an amorphous oxide, (a) without and (b) with a valence alternation pair (VAP). The illustrated shift corresponds to a VAP concentration of 0.75×10^{14} cm^{-2}. The upper panels schematically illustrate the charge distribution, distinguishing the charge polarization in the Ge-O bond due to the electronegativity difference ($\pm\delta$) from the fixed charge associated to the VAP ($\pm$, red).

similarly holds for the analogous Si/SiO$_2$ interfaces [57]. Thus, it appears that a different origin needs to be found to account for the large variation of the valence band offset observed in experiments [106, 119, 158].

Role of valence alternation pairs

As we saw in chapter 4, the structure of substoichiometric germanium oxide was found to comprise sizeable concentrations of positively charged threefold coordinated O atoms and negatively charged Ge dangling bonds [17]. To examine the effect of these charged moieties on the interface dipole, we introduced a single valence alternation pair in the transition region of the Ge/GeO$_2$ interface model showing an amorphous oxide. We proceeded by breaking a Ge-Ge bond in the suboxide region and by moving one of the Ge atoms across the plane of its three neighboring O atoms, as in the puckered configuration of the E'_1 defect in SiO$_2$ [127]. The displaced Ge atom is stabilized by the formation of a threefold coordinated O atom [21]. Upon structural relaxation, we achieved in this way a model structure with a negatively charged Ge dangling bond on the substrate side of the interface and a positively charged O atom located higher up in the suboxide, as illustrated in Fig. 6.5(b). The location of the charge in this valence alternation pair was checked through an analysis based on maximally localized Wannier functions [98]. The total energy of the modified model structure exceeds that of the initial one by only ~0.45 eV. This value is low, in agreement with the fact that valence

alternation pairs are competing structural arrangements in GeO_x (cf. chapter 4). The local electrostatic potential of the interface model with the valence alternation pair is given in Fig. 6.6(a) and the variation of the offset with respect to the defect-free interface model is shown in Fig. 6.6(b). The extra interface dipole is found to change the offset by ~0.7 eV.

The introduction of the valence alternation pair concurrently increases the valence band offset of the model interface from 3.5 eV to 4.2 eV, as schematically illustrated in Figs. 6.7(a) and 6.7(b). The latter valence band offset agrees well with experimental ones, which range between 4.0 and 4.5 eV [119, 158]. Furthermore, the size of the observed shift might provide an explanation for the range of experimental values, which would reflect the dependence of the interface dipole on the varying concentration of VAPs achieved with different growth procedures. The shift of the valence band offset depends on the areal density of VAPs, which in our model corresponds to 0.75×10^{14} cm^{-2}. This density of VAPs appears high compared to defect densities measured at Ge/GeO_2 interfaces [1]. However, VAPs do not directly lead to defect states in the Ge band gap and rather act as fixed charges [17].

6.4 Conclusions

We have derived an atomistic model of the $Ge(001)/GeO_2$ interface using first-principles methods. The interface model consists of amorphous GeO_2 which is connected to crystalline Ge through a suboxide transition region showing regular structural parameters in good agreement with experimental measurements. The model is free from coordination defects and does not show any electronic states in the band gap. The valence band offset determined within a mixed hybrid density functional scheme, is found to be smaller (3.4 eV) than experimentally determined offsets [106, 97, 119].

Moreover, we investigated to what extent the structural organization at the Ge/GeO_2 interface could affect the interface dipole and consequently the value of the valence band offset. We first considered model interfaces in which all Ge atoms are fourfold coordinated and all O atoms are twofold coordinated. For these models, our calculations yield a well defined value for the valence band offset, which underestimates the range of experimental values. Furthermore, this does not explain the large range of values found in different experiments. We then considered the role of valence alternation pairs by incorporating one of such pairs within a model of the Ge/GeO_2 interface. This yielded a larger value of the valence band offset which agrees well with the range of measured values. In this description, the increase in the valence band offset results from the contribution to the interface dipole coming from negatively charged Ge dangling bonds on the germanium side and positively charged threefold O atoms on the oxide side of the interface. It is proposed that the observed range of measured values results from different areal concentrations of valence alternation pairs as incorporated during oxide growth.

7 X-ray photoemission spectroscopy

In this chapter, we determine in an accurate way the Ge $3d$ core-level shift across the Ge/GeO$_2$ interface. The ultimate aim is to clarify the relation between measured core-level shifts and the underlying structural properties of the Ge/GeO$_2$ interface. For this purpose, it is important to achieve high quantitative accuracy in the calculated Ge core-level shifts. We begin our study by assessing the overall accuracy associated to our determination of Ge core-level shifts in molecules by comparison with experimental data. This study on molecules gives two main results: *(i)* it shows that calculated Ge core-level shifts generally differ from experiment by less than 0.1 eV with hybrid functionals achieving a small quantitative improvement with respect to semilocal functionals; *(ii)* it allows us to verify the validity of our pseudopotential approach when moving from an all-electron description to a pseudopotential one. As a side result, we also find that differences between Ge $3d$ and $2p$ shifts are negligible. The achieved level of accuracy enables a quantitative comparison with experiment for the Ge core-level shift across the Ge/GeO$_2$ interface. To model the interface, we use atomistic structures containing only fourfold-coordinated Ge atoms and twofold-coordinated O atoms. These models enable us to achieve a comprehensive description of electronic properties at Ge/GeO$_2$ interfaces, since calculated VBOs for these same models are already available and presented in Chapter 6. Since the core-level shift determination involves charged supercell calculations, the convergence due to finite-size effects needs to be carefully ensured. Thus, the core-level shift calculations at the interface are performed through the use of two different methods. In the first method, we adopt a two-step procedure in which the core-levels are seperately determined in bulk models of the two interface component and then aligned through a local reference potential determined at the interface. The second method is based on core-level shift calculations performed directly at the interface. To cope with the spurious effect of periodic boundary conditions, we correct our results for finite-size effects using classical electrostatics. The overall agreement between the two schemes allows us to assess whether the adopted interface model structures are consistent with experimental data.

7.1 Methods

Total energies are obtained from electronic structure calculations based on density functional theory. We used two different density functionals. The semilocal PBE functional and the hybrid PBE0 functional.

As we treat systems of increasing complexity, we adapt the applied electronic-structure calculation scheme. In this chapter we use three different schemes. The first scheme assumes spherical symmetry and is here only used for all-electron calculations at the PBE level for the Ge atom and its excited states. The radial Kohn-Sham equations are integrated numerically with different spin channels treated separately. Relativistic effects are included in the scalar approximation [81]. These calculations are performed with the ATOMIC code[46] provided in the QUANTUM-ESPRESSO package [56].

In order to extend the all-electron calculations to molecular systems and to hybrid functionals, we use an electronic-structure scheme based on local basis sets, as implemented in the ADF code [141]. The ADF code employs Slater-type orbitals as basis functions. The basis functions are extended to include diffuse functions to treat atomic excitations involving weakly bonded $4d$ states when appropriate. Relativistic effects are treated in the zeroth-order regular approximation [147]. The electronic-structure calculations on molecules are performed at the all-electron level with triple-ζ (TZ2P) basis sets. In the structural optimizations, the convergence criteria are set at 1 mHa for the total energy and at 1 mHa/Å for the remaining maximal force. The molecular structures are relaxed within this structural relaxation scheme.

To address the Ge/GeO_2 interface system, we use our plane-wave density functional approach in which core-valence interactions are described by normconserving pseudopotentials [142]. The structural optimizations are performed at the PBE level.

We model the core-electron binding energy E_b measured in XPS experiments as the energy required to excite the electron from its core-level to the vacuum level:

$$E_b = E^+ + V_{vac} - E^0, \tag{7.1}$$

where E^+ is the final-state energy of the system in the presence of a core hole, V_{vac} the reference vacuum potential for the extracted electron, and E^0 the energy of the initial state. We assume the vertical approximation which implies that the atomic structure is not modified in the final state and that polarization effects are described by the high-frequency dielectric constant. In our all-electron schemes, the final state energy E^+ is obtained through a calculation in which the occupation of the core state is constrained. This corresponds to the evaluation of core-level binding energies through the ΔSCF method [50].

More specifically, we focus in this work on core-level shifts with respect to an adopted reference:

$$\Delta E_{\text{b}} = (E^+ - E^0) - (E^+_{\text{ref}} - E^0_{\text{ref}}). \tag{7.2}$$

Such core-level shifts then become also accessible in the pseudopotential scheme. For this purpose, a special pseudopotential is generated for describing the valence electrons in the presence of a core hole [115]. With respect to all-electron schemes, the pseudopotential approach does not account for the relaxation of core electrons. This approximation is generally very good, as demonstrated for the analogous Si/SiO_2 interface [159, 108, 112].

In the pseudopotential calculations, the presence of the core hole requires a uniform background charge to achieve charge neutrality in the periodically repeated simulation cell. Spurious interaction effects due to the periodic boundary conditions might affect the calculated results and need to be accounted for. For the molecular systems, we calculated core-level shifts using cubic simulation cells with sides increasing from 20 to 30 bohr. The desired shifts could then be obtained through extrapolation to infinite cell size [110, 112]. For the interface systems, the effect due to the dielectric discontinuity is less trivially determined. Special attention to the ensuing corrections will be given in Sec. 7.3.

7.2 Accuracy of adopted approach

Atom

The atom is the most simple case for which core-level shifts can be calculated and is therefore a suitable test case to perform comparison between different theoretical schemes. In particular, we are interested in validating the local basis sets used in the all-electron scheme. To this end, we here first validate the basis sets through comparisons with results obtained through numerical integration, which are not subject to basis set errors. Then, we compare core-level shifts calculated at the PBE and PBE0 levels of theory. The section concludes with a comparison between Ge $3d$ and Ge $2p$ core-level shifts.

To validate the local basis sets, we focus on Ge atoms imposing spherical symmetry. The core-level binding energies are given with respect to the ground state Ge atom in the electronic configuration $[\text{Ar}]3d^{10}4s^24p^2$. In Table 7.1, Ge $3d$ core-level shifts obtained through numerical integration are compared with those obtained with three different local basis sets for various electronic configurations of the outer valence shells. We consider the triple-ζ basis set with two polarization functions (TZ2P), the quadruple-ζ basis set with four polarization functions (QZ4P), and the even-tempered basis set augmented with three polarization functions and three diffuse functions (ETQZ3P-3diff). The calculations are performed at the PBE level of theory.

As seen in Table 7.1, the core-level shifts spread out over a range of more than 15 eV. For the s^1p^3, s²p¹, and s¹p² configurations, one notices that the results obtained with the TZ2P and

Table 7.1 – Calculated $3d$ core-level shifts for the Ge atom in various excited electronic configurations of the outer valence shells with respect to the ground-state configuration $[Ar]3d^{10}4s^2 4p^2$. The exact core-level shifts are obtained through numerical integration of the Kohn-Sham equations (ATOMIC code, Ref. [56]) and are compared to those obtained with three different local basis sets (ADF code, Ref. [141]). The calculations are performed at the PBE level of theory. Energies are in eV.

Configuration	Exact	TZ2P	QZ4P	ETQZ3P-3diff
$s^1 p^3$	1.666	1.671	1.668	1.671
$s^2 p^1 d^1$	4.689	1.252	4.229	4.672
$s^1 p^2 d^1$	6.113	3.032	5.757	6.100
$s^2 p^1$	10.230	10.239	10.226	10.223
$s^1 p^2$	11.862	11.869	11.859	11.868
$s^1 p^1 d^1$	15.568	13.932	15.601	15.553

Table 7.2 – Comparison between $3d$ core-level shifts for the Ge atom as calculated with the semilocal PBE and hybrid PBE0 functionals. The ADF code is used with the ETQZ3P-3diff basis set. The last column corresponds to the difference between the PBE0 and PBE shifts. Energies are in eV.

Configuration	PBE	PBE0	Diff.
$s^1 p^3$	1.671	1.814	0.143
$s^2 p^1 d^1$	4.674	4.959	0.285
$s^1 p^2 d^1$	6.102	6.543	0.441
$s^2 p^1$	10.224	10.115	0.109
$s^1 p^2$	11.869	11.938	0.069
$s^1 p^1 d^1$	15.553	15.791	0.238

QZ4P basis sets are both very accurate. For describing the excitations to states involving the weakly bound $4d$ level, even the large standard basis set (QZ4P) is not sufficient and a good agreement is only achieved through the use of the ETQZ3P-3diff basis set which includes diffuse functions.

Next, we compare in Table 7.2 atomic core-level shifts calculated with the PBE functional with those obtained with the hybrid PBE0 functional. In this comparison, we use the ETQZ3P-3diff basis set to account for the weakly bonded $4d$ levels. We note that the differences for the more localized configurations ($s^1 p^3$, $s^2 p^1$, and $s^1 p^2$) never exceed 0.15 eV. This result is in good agreement with the general behavior of charge transition levels of atomically localized defect states [6, 7]. More generally, calculations with the PBEh(α) functional show that the core-level shift dependence on α is linear, in agreement with previous calculations for both localized and extended states [27, 5]. The rate of change is specific to the considered electronic configuration.

Table 7.3 – Comparison between Ge $2p$ and Ge $3d$ core-level shifts calculated with the hybrid PBE0 functional. The ADF code is used with the ETQZ3P-3diff basis set. The difference between Ge $2p$ and Ge $3d$ core-level shifts is given in the last column. Energies are in eV.

Configuration	Ge $3d$	Ge $2p$	Diff.
$s^1 p^3$	1.814	1.831	0.017
$s^2 p^1 d^1$	4.959	4.907	−0.052
$s^1 p^2 d^1$	6.543	6.529	−0.014
$s^2 p^1$	10.115	10.314	0.199
$s^1 p^2$	11.938	12.150	0.212
$s^1 p^1 d^1$	15.791	16.099	0.308

The Ge $3d$ level is only slightly deeper than the valence electrons ($E_b \sim 30$ eV), while the Ge $2p$ level is much deeper ($E_b \sim 1218$ eV) [106]. It is therefore of interest to compare $2p$ and $3d$ core-level shifts as both are experimentally accessible. In Table 7.3, Ge $2p$ core-level shifts calculated with PBE0 functionals are compared with the respective Ge $3d$ shifts. Overall, Ge $3d$ and Ge $2p$ are remarkably similar for shifts up to ~6.5 eV and show deviations of at most 0.3 eV for larger shifts.

Molecules

The primary aim of this section is to assess the accuracy of Ge core-level shifts calculated within all-electron hybrid density functional schemes. We thus consider a set of molecules for which experimental data are available [11]. In particular, we determine the optimal value of the fraction α of non-local exchange to be used in the hybrid functional PBEh(α). We then switch to the pseudopotential scheme and quantify to what extent this approximation deteriorates the accuracy achieved with the all-electron scheme.

Structural properties

The relaxed structures of a set of Ge-based molecules are determined with the PBEh(α) hybrid functional for various values of α. We here use the all-electron ADF code with the TZ2P basis set, which is expected to give converged core-level shifts in the absence of diffuse d electrons (cf. Table 7.1). Table 7.4 shows relaxed structural parameters for the two extreme values $\alpha = 0$ (PBE) and $\alpha = 1$. Overall, the effect of α is small with bond lengths and bond angles differing by less than 0.1 Å and 2°, respectively.

To illustrate these calculations in more detail, we focus on the Ge(CH$_3$)$_4$, GeH$_4$, and GeF$_4$ molecules and give in Fig. 7.1 the evolution of three specific bond lengths with α. The bond lengths vary in an approximately linear way with α. For $\alpha = 0$ (PBE), they are slightly larger than their experimental counterparts, while the opposite behavior is found for $\alpha = 1$. The best

Table 7.4 – Bond lengths and bond angles for a set of Ge-based molecules obtained with PBEh(α) functionals for $\alpha = 0$ (PBE) and $\alpha = 1$. The all-electron ADF code is used with the TZ2P basis set.

| Molecule	Parameter	$\alpha = 0$	$\alpha = 1$
Ge(CH$_3$)$_4$	d(Ge-C)	1.979 Å	1.931 Å
(CH$_3$)$_3$GeH	d(Ge-H)	1.551 Å	1.517 Å
	d(Ge-C)	1.975 Å	1.926 Å
	∠ H-Ge-C	108.3°	108.0°
(CH$_3$)$_2$GeH$_2$	d(Ge-H)	1.546 Å	1.513 Å
	d(Ge-C)	1.970 Å	1.922 Å
	∠ C-Ge-C	111.7°	112.7°
	∠ H-Ge-C	109.4°	109.2°
	∠ H-Ge-H	107.4°	107.3°
(CH$_3$)GeH$_3$	d(Ge-H)	1.541 Å	1.508 Å
	d(Ge-C)	1.964 Å	1.918 Å
	∠ H-Ge-C	110.6°	110.6°
	∠ H-Ge-H	108.4°	108.3°
GeH$_4$	d(Ge-H)	1.533 Å	1.503 Å
GeH$_3$Br	d(Ge-H)	1.534 Å	1.499 Å
	d(Ge-Br)	2.332 Å	2.258 Å
	∠ H-Ge-H	111.4°	111.5°
	∠ H-Ge-Br	107.4°	107.3°
GeH$_3$Cl	d(Ge-H)	1.533 Å	1.499 Å
	d(Ge-Cl)	2.175 Å	2.108 Å
	∠ H-Ge-H	111.7°	111.7°
	∠ H-Ge-Cl	107.1°	107.2°
(CH$_3$)GeHF$_2$	d(Ge-H)	1.534 Å	1.495 Å
	d(Ge-C)	1.939 Å	1.888 Å
	∠ H-Ge-C	121.5°	119.7°
	∠ F-Ge-C	108.5°	109.0°
(CH$_3$)GeCl$_3$	d(Ge-Cl)	2.162	2.083 Å
	d(Ge-C)	1.949	1.889 Å
	∠ H-C-Ge	108.5°	109.2°
	∠Cl-Ge-C	111.2°	111.7°
GeBr$_4$	d(Ge-Br)	2.316 Å	2.226 Å
GeCl$_4$	d(Ge-Cl)	2.143 Å	2.065Å
GeF$_4$	d(Ge-F)	1.713 Å	1.639Å
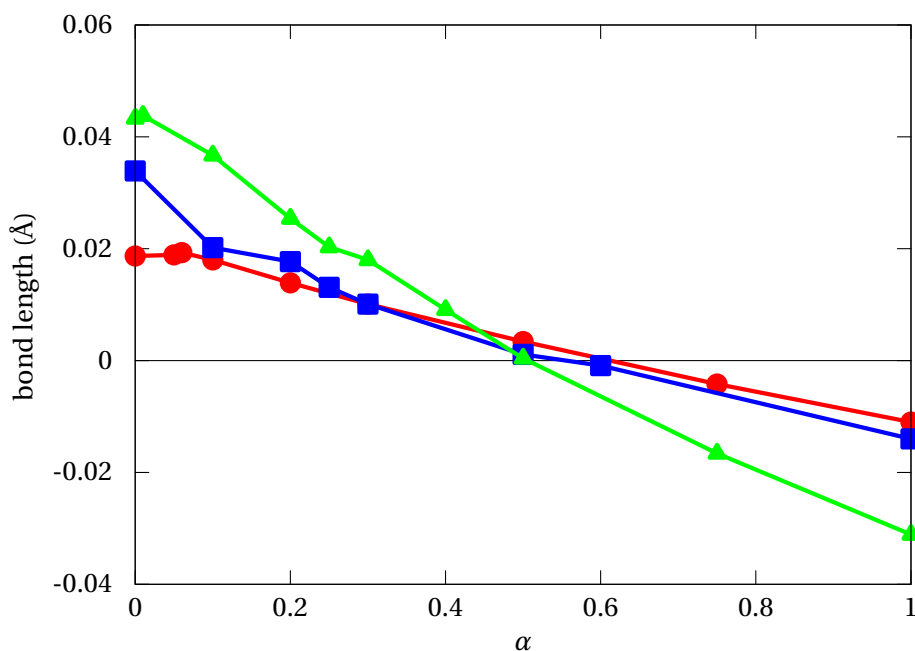
Figure 7.1 – Dependence of the Ge-C, Ge-H, and Ge-F bond lengths on the fraction α of nonlocal exchange for the molecules $Ge(CH_3)_4$ (squares, blue), GeH_4 (discs, red), and GeF_4 (triangles, green), respectively. The ADF code is used with the TZ2P basis set. The bond lengths are given as deviations with respect to experimental values: $d_{Ge-C} = 1.945$ Å (Ref. [66]), $d_{Ge-H} = 1.514$ Å (Ref. [105]), and $d_{Ge-F} = 1.67$ Å (Ref. [41]).

agreement with experiment is found for $\alpha \cong 0.5$. As will be seen below, the structural variations observed here can be considered to be marginal since they do not have a significant impact on the calculated core-level shifts.

Ge $3d$ core-level shifts

Ge $3d$ binding energies referred to the vacuum level are calculated within an all-electron scheme for the set of molecules in Table 7.4. For each molecule, the calculations are performed with the PBEh(α) functional for three to five different values of α (ADF code with TZ2P basis set). The molecular structures used in the binding energy calculations are optimized at the corresponding level of theory. The calculated binding energies are found to vary linearly with α.

Since we focus in this work on the accuracy of core-level shifts, we apply a global shift k to the calculated binding energies E^{b} before comparing with experimental values. In this way, systematic errors inherent to the absolute binding energies, such as those resulting from the relativistic approximation used, do not affect the comparison with experiment. For a set of calculated binding energies obtained with the functional PBEh(α), the global shift k is taken

Table 7.5 – Comparison between calculated and measured Ge $3d$ binding energies for a set of Ge-based molecules. We obtain PBE and PBE0 binding energies using molecular structures optimized at the corresponding level of theory (ADF code with TZ2P basis set). With respect to the calculated results, the reported values for PBE and PBE0 include a global shift k of 0.31 and −0.16 eV, respectively. The adopted k minimizes the rms deviation (rms ΔE_b) with respect to the experimental values (Ref. [11]). Energies are in eV.

Molecule	PBE	PBE0	Expt.
$Ge(CH_3)_4$	36.18	36.08	36.13
$(CH_3)_3GeH$	36.44	36.35	36.35
$(CH_3)_2GeH_2$	36.78	36.67	36.68
$(CH_3)GeH_3$	37.09	37.01	36.98
GeH_4	37.61	37.46	37.40
GeH_3Br	38.17	38.12	38.15
GeH_3Cl	38.32	38.29	38.27
$(CH_3)GeHF_2$	39.08	39.13	39.02
$(CH_3)GeCl_3$	39.04	39.13	39.11
$GeBr_4$	39.31	39.47	39.45
$GeCl_4$	39.95	40.09	40.10
GeF_4	41.72	41.93	42.05
rms ΔE^b	0.041	0.016	–

to minimize the rms deviation with respect to the experimental data [11], namely

$$\text{rms}\,\Delta E_b(\alpha) = \sqrt{\frac{1}{N}\sum_i^N \left[E_b^i(\alpha) + k(\alpha) - E_b^i(\text{expt.}) \right]^2}, \tag{7.3}$$

where the sum is over the molecules in the considered set.

In Table 7.5, we show the comparison with experiment for binding energies calculated with the semilocal PBE functional (α=0) and with the hybrid PBE0 functional (α=0.25). The reported data include a global shift of 0.31 and −0.16 eV for PBE and PBE0, respectively. The accuracy of calculated Ge $3d$ core-level shifts can be estimated through rms ΔE_b, and results in 0.041 eV for PBE and in 0.016 eV for PBE0. These results indicate that core-level shifts obtained with the PBE functional are already very accurate and that a further improvement can be achieved with the PBE0 functional. The good agreement between PBE and PBE0 shifts is analogously found for ionization potentials in molecules [44] and defect levels [6] in solids, and stems from the localized nature of the core-level state [7, 8].

While the PBE0 hybrid functional is recommended for a large class of systems, it is admitted that the optimal α might be material or even property dependent [117]. Therefore, we investigate how rms ΔE_b depends on the fraction α of nonlocal exchange. For each value of α, we first derive theoretical values through the linear interpolation of our results obtained for a
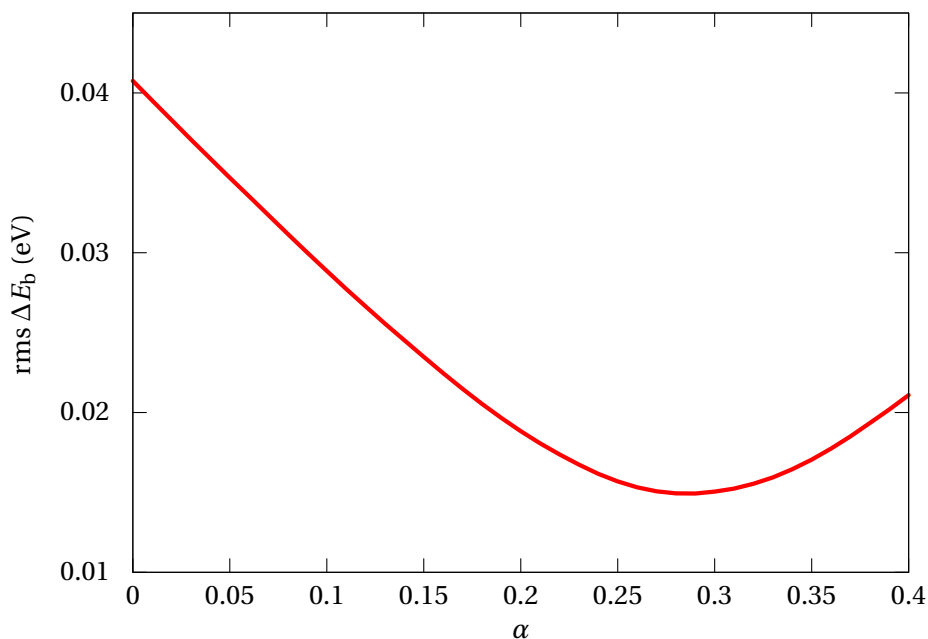
Figure 7.2 – Root mean square deviation ΔE_b of the Ge $3d$ core-level shift with respect to experimental results as a function of the fraction α of nonlocal exchange used in the PBEh(α) functional. The smallest rms deviation ($\Delta E_b = 0.015$ eV) is achieved for α=0.28.

limited set of α values. Then, an optimal global shift $k(\alpha)$ is determined as explained above. The rms ΔE_b resulting from this procedure are displayed as a function of α in Fig. 7.2. The minimal value of the rms ΔE_b is obtained for $\alpha = 0.28$ (rms $\Delta E_b = 0.015$). This error does not differ significantly from the one achieved with $\alpha = 0.25$. In the following hybrid functional calculations, we will thus stick to the common PBE0 functional, which corresponds to the latter value of α.

Ge $2p$ vs Ge $3d$ core-level shifts

In calculations performed on various excited configurations of the Ge atom, Ge $2p$ and Ge $3d$ core-level shifts are found to be very similar (cf. Sec. 7.2). To confirm this trend in more general terms, we here compare Ge $2p$ and Ge $3d$ shifts for the considered set of Ge-based molecules. The core-level shift calculations are performed with the PBE0 functional within an all-electron scheme (ADF code with TZ2P basis set). We use atomic coordinates obtained at the same level of theory. The calculated Ge $2p$ and Ge $3d$ core-level shifts are given in Table 7.6. For the considered set of molecules, the shift ranges over an interval of almost 6 eV, but the difference between the two core-level shifts remains always smaller than 0.1 eV. The similarity of Ge $2p$ and Ge $3d$ core-level shifts is supported by experimental observations [47, 124]. Thus, we only consider Ge $3d$ core-level shifts in the following.

Table 7.6 – Comparison between calculated Ge $3d$ and Ge $2p$ core-level shifts in Ge-based molecules. The shifts are determined with the PBE0 hybrid functional in an all-electron scheme (ADF code with TZ2P basis set). The atomic structures used are obtained at the same level of theory. The core-levels are referred to respective levels of the GeH$_4$ molecule. The last column gives the difference between Ge $2p$ and Ge $3d$ shifts. Energies are in eV.

Molecule	$2p$	$3d$	Diff.
Ge(CH$_3$)$_4$	-1.411	-1.392	-0.019
(CH$_3$)$_3$GeH	-1.137	-1.122	-0.015
(CH$_3$)$_2$GeH$_2$	-0.816	-0.795	-0.021
(CH$_3$)GeH$_3$	-0.441	-0.454	0.013
GeH$_3$Br	0.726	0.655	0.071
GeH$_3$Cl	0.880	0.892	-0.012
CH$_3$GeHF$_2$	1.663	1.660	0.003
CH$_3$GeCl$_3$	1.720	1.665	0.055
GeBr$_4$	2.084	1.999	0.085
GeCl$_4$	2.632	2.595	0.037
GeF$_4$	4.386	4.451	-0.065

Accuracy of present pseudopotential implementation

In order to address interface models, the pseudopotential scheme is more practical not only because of the lower numerical cost involved but also because of the suitable periodic boundary conditions. However, structural relaxations at the hybrid functional level remain numerically expensive, and it thus appears convenient to use model structures optimized at the semilocal PBE level. In this section, we use the set of Ge-based molecules to quantify the loss of accuracy due to these simplifications.

We first examine the validity of the pseudopotential approximation, in which the relaxation of core electrons upon electron excitation is neglected. For this purpose, we adopt a given atomic configuration of the molecules (corresponding to the geometries obtained at the PBE level) and perform core-level shift calculations at the PBE0 level. By comparing the first two columns in Table 7.7, one sees that core-level shifts obtained with the pseudopotential scheme are very accurate with deviations with respect to all-electron results lower than 0.06 eV. The comparison with all-electron results is a critical step of the validation process which ensures that the pseudopotential scheme gives quantitatively reliable shifts [1].

The comparison is then extended to all-electron calculations performed on molecular structures consistently optimized at the hybrid functional level (Table 7.7). Overall deviations

---

1. We submitted the pseudopotentials used in Ref. [122] to a similar comparison against all-electron results focusing on the core-level shift between the idealized Ge(GeH$_3$)$_4$ and Ge(OGeH$_3$)$_4$ molecules (cf. Sec. 7.3). This test revealed an enhanced shift by 0.59 eV with respect to the corresponding all-electron shift, to be compared with the deviation of 0.05 eV found within the present pseudopotential scheme.

Table 7.7 – Comparison between pseudopotential (PP) and all-electron (AE) Ge $3d$ core-level shifts for various Ge-based molecules calculated at the PBE0 level. The pseudopotential results correspond to structures optimized at the PBE level ($\mathbf{R}_{PBE}$). The all-electron results (ADF code with TZ2P basis set) are obtained for the same geometries ($\mathbf{R}_{PBE}$) and for structures consistently optimized at the PBE0 level ($\mathbf{R}_{PBE0}$). The respective differences between the AE and PP calculations are given by Δ_1 and Δ_2. The core-levels are referred to that of the GeH_4 molecule. Energies are in eV.

| | PP | AE | | AE | |
Molecule	$\mathbf{R}_{PBE}$	$\mathbf{R}_{PBE}$	Δ_1	$\mathbf{R}_{PBE0}$	Δ_2
$Ge(CH_3)_4$	-1.375	-1.343	0.032	-1.378	-0.002
$(CH_3)_3GeH$	-1.120	-1.119	0.001	-1.114	0.005
$(CH_3)_2GeH_2$	-0.805	-0.792	0.013	-0.792	0.013
$(CH_3)GeH_3$	-0.442	-0.462	-0.020	-0.451	-0.009
GeH_3Br	0.700	0.690	-0.010	0.657	-0.043
GeH_3Cl	0.863	0.852	-0.011	0.824	-0.039
$(CH_3)GeHF_2$	1.710	1.709	-0.001	1.664	-0.046
$(CH_3)GeCl_3$	1.689	1.714	0.025	1.668	-0.021
$GeBr_4$	2.007	2.065	0.058	2.005	-0.002
$GeCl_4$	2.630	2.681	0.051	2.625	-0.004
GeF_4	4.505	4.561	0.056	4.465	-0.040

remain below 0.05 eV, indicating that the combined use of the PBE structures and the pseudopotential scheme does not deteriorate the overall accuracy in a significant manner. In particular, we note that the comparison between pseudopotential and all-electron core-level shifts calculated at the PBE0 level does not suffer significantly from the fact that the pseudopotentials are generated at the PBE level of theory, in agreement with previous findings for ionization potentials [28].

In the last part of this subsection, we use the flexibility of the pseudopotential code to provide deeper insight into the underlying reasons for the overall better performance of PBE0 with respect to PBE. As seen above, the differences between PBE and PBE0 optimized structures do not affect the core-level shifts in an appreciable way (Table 7.7). Therefore the effect should be searched in the electronic-structure description. In Table 7.8, we compare core-level shifts obtained through a full PBE0 electronic minimization with those obtained through a first-order perturbational scheme based on PBE wave functions. The comparison shows that the differences between the PBE and PBE0 wave functions lead to negligible differences in the core-level shifts. This suggests that the better agreement recorded for the PBE0 core-level shifts should be assigned to the improved energy differences achieved with the PBE0 functional, possibly due to the reduced self-interaction, rather than to an improved description of the wave functions.

Table 7.8 – Comparison between Ge $3d$ core-level shifts obtained selfconsistently at the PBE0 level (Ψ_{PBE0}) with those obtained via a perturbational scheme based on PBE wave functions (Ψ_{PBE}), for various Ge-based molecules. The difference between the two shifts is given in the last column. In both calculations, we use the same molecular geometries corresponding to those obtained at the PBE level. The core-levels are referred to that of the GeH_4 molecule. Energies are in eV.

Molecule	Ψ_{PBE0}	Ψ_{PBE}	Diff.
$Ge(CH_3)_4$	-1.375	-1.378	-0.002
$(CH_3)_3GeH$	-1.120	-1.121	-0.002
$(CH_3)_2GeH_2$	-0.805	-0.806	-0.001
$(CH_3)GeH_3$	-0.442	-0.442	-0.001
GeH_3Br	0.700	0.699	-0.001
GeH_3Cl	0.863	0.861	-0.002
$(CH_3)GeHF_2$	1.710	1.702	-0.008
$(CH_3)GeCl_3$	1.689	1.684	-0.005
$GeBr_4$	2.007	2.005	-0.002
$GeCl_4$	2.630	2.624	-0.005
GeF_4	4.505	4.490	-0.015

Ge(001)-$c(4 \times 2)$ surface

In this section, we continue with the validation of our theoretical approach by calculating Ge $3d$ core-level shifts at the Ge(001) surface. This surface is known to reconstruct through the formation of rows of buckled dimers and has been characterized in detail by high resolution XPS [51, 85, 130, 88]. Given the fact that the surface core-level shifts are at most 0.5 eV, the calculations in this section are only performed at the PBE level. Indeed, for such small shifts the estimated improvement achieved through the use of a hybrid functional would not exceed the overall expected accuracy.

We thus generate a model for the Ge(001) surface showing the $c(4 \times 2)$ dimer reconstruction. In the primitive surface cell, we use 12 Ge layers and 11 Å of vacuum separating the slabs in the z direction normal to the surface. Dangling bonds on the bottom of the slab are terminated with hydrogen atoms to simulate bulk Ge. The four bottommost Ge layers are kept fixed in bulk positions. For the geometry optimization, we use a $4 \times 4 \times 1$ Monkhorst pack mesh, which is taken to be off-center to avoid the vanishing band gap of Ge at the Γ point. With these settings, the use of the next available denser grid of **k**-points results in an total-energy change of less than 0.1 meV per atom. The structural relaxation gives a dimer bond of 2.58 Å and a dimer tilt angle of 20.1°, in excellent agreement with previous DFT calculations [51]. The relaxed structure is illustrated in Fig. 7.3.

To minimize spurious interactions between the core hole and its images, the primitive cell is repeated four times for the calculation of Ge $3d$ core-level shifts. We thus use a tetragonal
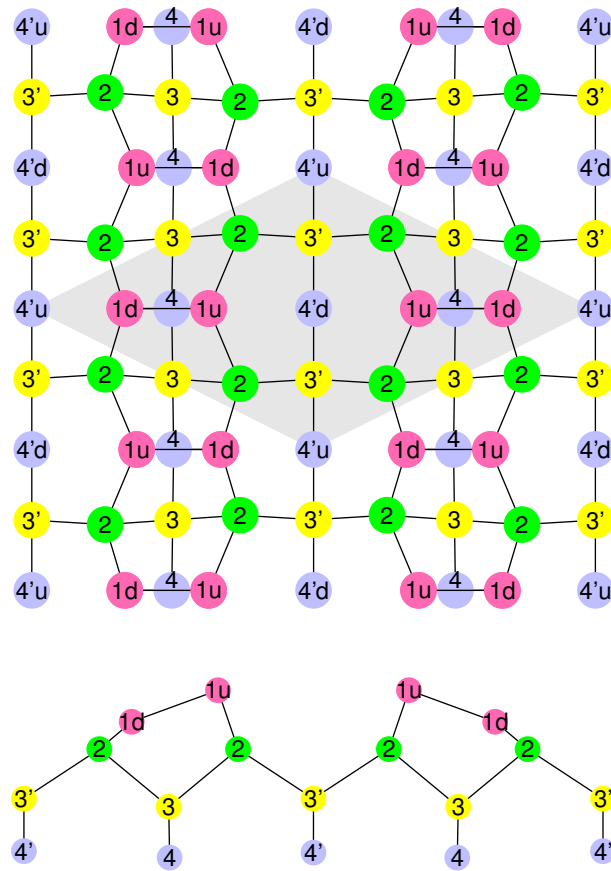
Figure 7.3 – Top view (top panel) and side view (bottom panel) of the Ge(001) surface with the $c(4 \times 2)$ surface reconstruction. The numbers indicate the layers after a common labeling convention (Refs. [159] and [51]). Atoms in the same layer share the same level of grey (color). The shaded area shows the primitive surface unit cell.

cell structure (cf. Fig. 7.3) with a lateral dimension of 30.7 bohr. The Brillouin zone is sampled with an off-centered $2 \times 2 \times 1$ **k**-point mesh ensuring the same density of **k**-points as in the primitive surface cell calculations. For the adopted mesh, the smallest band gap is 0.35 eV. Figure 7.3 shows the different Ge sites of the reconstructed surface that we consider in our calculation of Ge $3d$ core-level shifts.

The calculated Ge $3d$ core-level shifts are shown in Fig. 7.4. The largest shifts with respect to the bulk line are found for the upper atoms of the buckled dimers (1u) which are less effective in charge screening because of electron depletion. The calculated values are compared to various experimental data in Table 7.9. Overall, the agreement between theory and experiment is very good with deviations of at most 0.1 eV. This level of agreement strengthens our theoretical approach and allows us to address with confidence more complex systems which have not yet fully been settled by experimental studies.
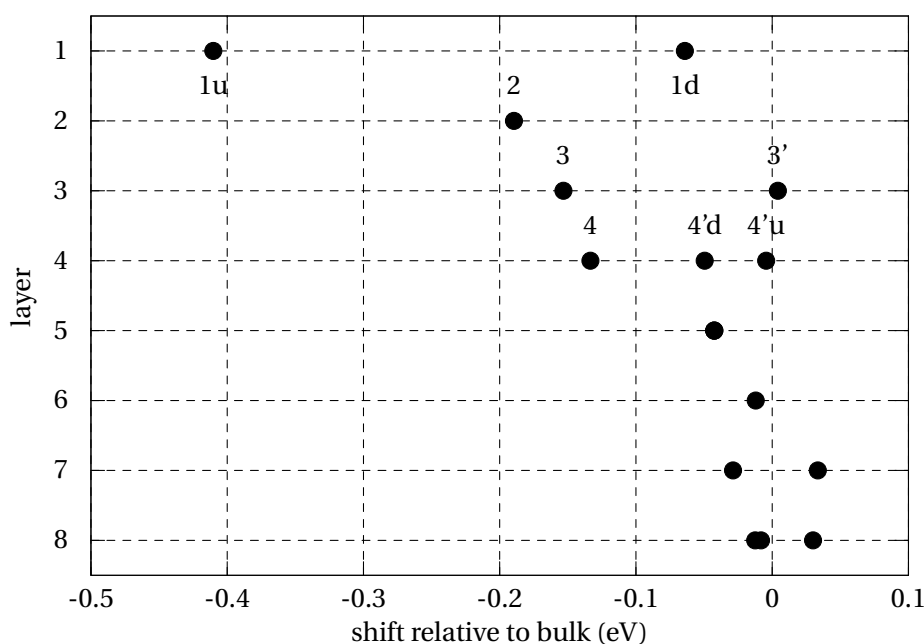
Figure 7.4 – Calculated Ge $3d$ core-level shifts at the Ge(001)-$c(4 \times 2)$ surface. The notation corresponds to that used in Fig. 7.3. The shifts are given with respect to the bulk line, which is obtained through an average of the Ge $3d$ core-levels of the atoms belonging to 6th, 7th, and 8th layers.

7.3 Core-level shifts at the Ge/GeO$_2$ interface

Idealized Ge oxide molecules

To investigate the role of the local chemistry on the Ge $3d$ core-level shifts, we first study idealized Ge oxide molecules which reproduce the various oxidation states of Ge in the transition region. We consider GeO$_n$(GeH$_3$)$_4$ molecules, in which O atoms are inserted in n of the Ge-Ge bonds, with n varying between 0 and 4. For illustration, the $n = 1$ case is shown in Fig. 7.5. The Ge-O bond length and the Ge-O-Ge angle are kept fixed at 1.795 Å and 180°, respectively.

The calculated Ge $3d$ core-level shifts for such idealized molecules are given in Fig. 7.6. The shifts are calculated for varying oxidation state n and for varying fraction α of nonlocal exchange in the functional. The core-level shifts are found to be proportional to both oxidation state n and fraction α. At the PBE level, the core-level separation between the lowest ($n = 0$) and highest oxidation state ($n = 4$) is 2.0 eV. For $\alpha = 0.25$ and $\alpha = 1$, the separation increases to 2.25 eV and 3 eV, respectively.

Table 7.9 – Calculated Ge $3d$ core-level shifts at the Ge(001)-$c(4 \times 2)$ surface compared to available experimental data. The shifts are referred to the bulk line, which in the calculation is taken to correspond to average shift of the atoms belonging to 6th, 7th, and 8th layers. All shifts are given in eV.

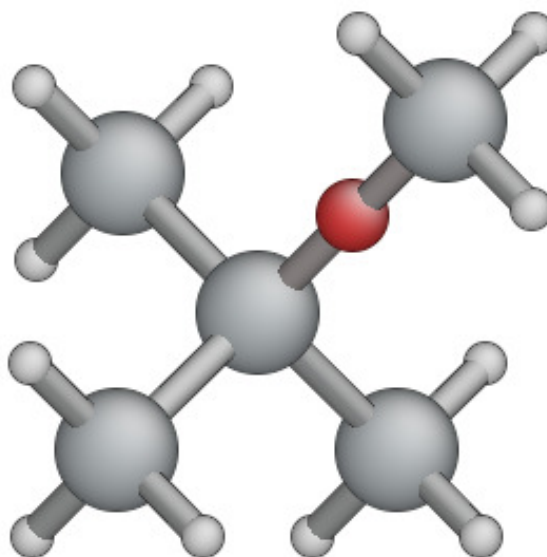| | Theory | Experiment | | | |
	Present	Ref. [51]	Ref. [85]	Ref. [130]	Ref. [88]
1u	-0.42	-0.51	-0.50	-0.43	-0.56
1d	-0.07	-0.10	-	-	-
2	-0.20	-0.23	-0.17	-	-0.24
3	-0.16	-	-	-	-
3$'$	0.00	-	-	-	-
4	-0.14	-	-	-	-
4$'$u	-0.01	-	-	-	-
4$'$d	-0.06	-	-	-	-

Figure 7.5 – Ball and stick model of the idealized $GeO_1(GeH_3)_4$ molecule representing the oxidation state $n = 1$.

Ge/GeO$_2$ interface models

Since the interface dipole contributes directly to the core-level shift across the interface, it is important to use a realistic description of the interfacial atomic structure. However, the bond pattern at the Ge/GeO$_2$ interface is at present essentially unknown. The two model structures which will be used in the present work are inspired from the structure at Si/SiO$_2$
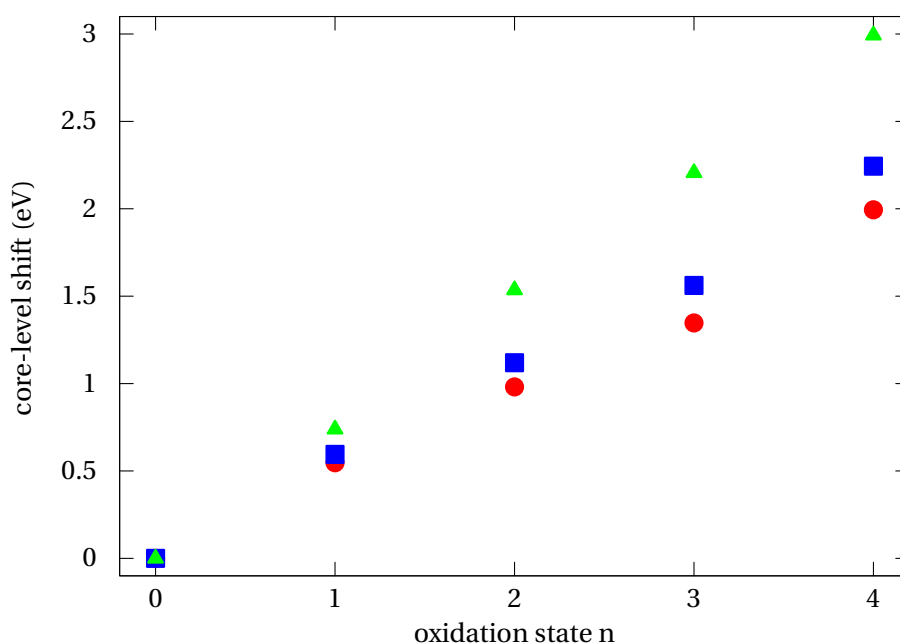
Figure 7.6 – Calculated core-level shifts for the idealized $GeO_n(GeH_3)_4$ molecules vs oxidation state n. Circles (red), squares (blue), and triangles (green) correspond to calculations performed with PBE, PBE0, and PBEh($\alpha = 1.0$) functionals, respectively. The levels are referred to that of the oxidation state $n = 0$.

interface which has undergone extensive investigations [113, 24, 23]. It should be understood that the present structures for the Ge/GeO_2 interface can only be validated through extensive comparisons with experimental data.

The first Ge/GeO_2 interface model comprises 217 atoms in a superlattice geometry with alternate layers of Ge and GeO_2 of approximately equal thickness [Fig. 7.7(a)]. In the interfacial plane, it has a $\sqrt{8} \times \sqrt{8}$ repeat unit with a side of 8.1 Å. The model was generated in Ref. [31] through full structural relaxations, which preserved the topology of its parent Si/SiO_2 interface structure [58, 24, 23]. In short, the model shows a smooth transition region between crystalline Ge and amorphous GeO_2 with reasonable structural parameters and without any coordination defect, all Ge atoms being fourfold coordinated and all O atoms twofold coordinated. The transition region shows the appearance of all intermediate oxidation states of Ge (Ge^{+1}, Ge^{+2}, and Ge^{+3}). The density of the GeO_2 region is 3.5 g/cm^3. For a more detailed description of the structure of this model, we refer the reader to Refs. [31] and [30]. This model has previously also been used for the calculation of the valence band offset, resulting in a value of 3.4 eV [31, 34].

The second interface model also has superlattice geometry but the GeO_2 is found in a crystalline β-cristobalite phase [Fig. 7.7(b)]. The connection is achieved as in a similarly constructed model of the Si/SiO_2 interface and occurs without any coordination defect [109, 112].
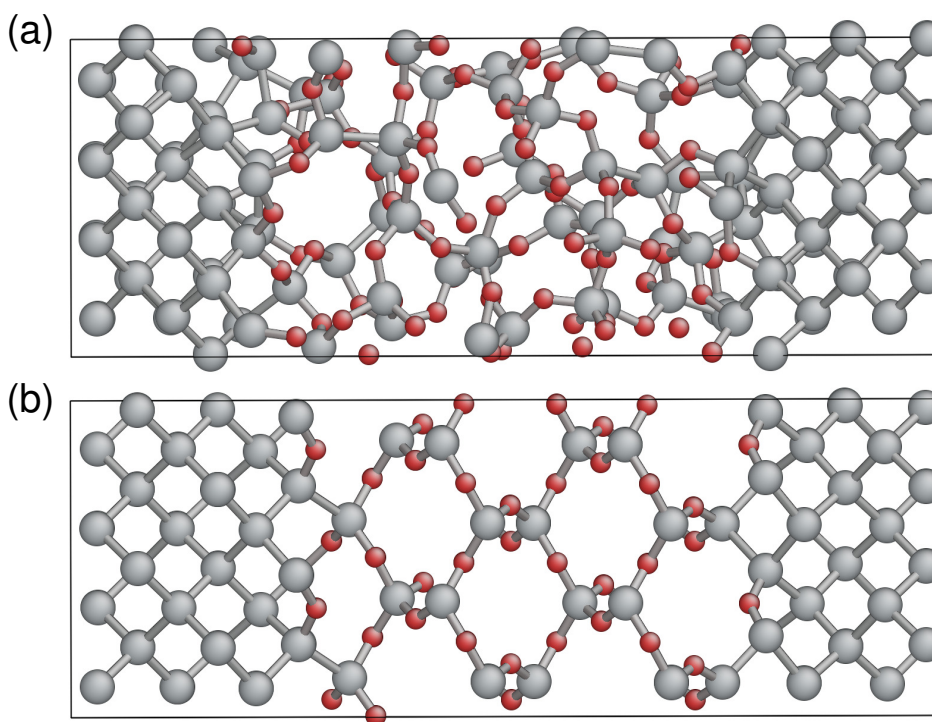
Figure 7.7 – Atomic structure of two Ge/GeO$_2$ interface models used in this work, in which the oxide is either (a) amorphous or (b) crystalline. The balls representing the Ge atoms are light grey while those representing the O atoms are dark grey (red).

In the interfacial plane, this model has the same repeat unit as the interface model with an amorphous oxide. The Ge layer consist of 9 atomic layers of Ge (11.6 Å). Following a similar approach as for the first model [31], we allow the oxide to relax in the direction normal to the interface, leading to a thickness of 21 Å and a density of 3.2 g/cm^3. While this model is expected to show overall similar electronic properties as the first one, it carries the advantage of having a small interfacial repeat unit together with a C$_8$ rotational symmetry around an axis perpendicular to the interface. This allows one to achieve easy scaling of the model in the lateral directions. In particular, we also use models with interfacial repeat units containing 4, 16, and 32 interface Ge atoms.

Calculation of core-level shift through potential alignment

We are here interested in determining the Ge $3d$ core-level shift across the Ge/GeO$_2$ interface including the effect of the interface dipole. This corresponds to the shift ΔE_{XPS} between the oxidation state $n = 0$ in Ge and the oxidation state $n = 4$ in GeO$_2$. The interface also implies a dielectric discontinuity between the dielectric constants of Ge (ϵ=16) and GeO$_2$ (ϵ=2.8), which leads to difficulties in treating electrostatic screening effects in the core-hole calculations because of their long-range nature. Therefore, two different procedures will be applied to

determinine this shift. In the present section, we apply a method which is commonly used for the alignment of band structures at interfaces [145, 13]. All calculations in this section are performed with the pseudopotential-plane-wave scheme, first at the PBE level, and then with the PBE0 functional without further relaxing the atomic coordinates. The application of a more direct method is deferred to the next section.

The method we apply here consists in performing the core-hole calculations separately in bulk models of the two interface components. The interface model is only used to determine the line-up of a reference potential V_{ref} across the interface, which then allows us to connect the two bulk calculations. More specifically:

$$\Delta E_{\text{XPS}} = E_{\text{b}}^{\text{GeO}_2} - E_{\text{b}}^{\text{Ge}} + \Delta V_{\text{ref}} = \Delta E_{\text{b}} + \Delta V_{\text{ref}}, \tag{7.4}$$

where $E_b^{\text{GeO}_2}$ and E_b^{Ge} are obtained from bulk calculations in GeO_2 and Ge, respectively:

$$
\begin{aligned}
E_b^{\text{GeO}_2} &= E_+ + V_{\text{ref}}^{\text{GeO}_2} - E_0, \tag{7.5} \\
E_b^{\text{Ge}} &= E_+ + V_{\text{ref}}^{\text{Ge}} - E_0. \tag{7.6}
\end{aligned}
$$

In particular, we note that in our pseudopotential scheme the calculations of both $E_b^{\text{GeO}_2}$ and E_b^{Ge} involve a same constant value, which is eliminated when taking the difference, $\Delta E_{\text{b}} = E_{\text{b}}^{\text{GeO}_2} - E_{\text{b}}^{\text{Ge}}$. The offset ΔV_{ref} of the reference potential across the interface,

$$\Delta V_{\text{ref}} = V_{\text{ref}}^{\text{Ge}} - V_{\text{ref}}^{\text{GeO}_2}, \tag{7.7}$$

is determined from the interface model calculation. We note that the calculations involving a positively charged core hole are in this way only performed for bulk models, where the total energy can be properly corrected [90, 95]. To deal with the long-range electrostatic effects in the bulk calculations, we applied a simple Madelung-like correction [90, 95], as this correction has been demonstrated to be particularly accurate for well localized charges [83]. The calculation involving the interface model is only used for the potential alignment and is charge neutral. The fact that the electrostatic correction only needs to be applied to the bulk calculations is a clear advantage of the present potential-alignment method.

As reference potential V_{ref}, we take the average electrostatic potential around the Ge nucleus. This is achieved through a Gaussian weight function with width of 0.175 bohr centered on the Ge atom. The variations of V_{ref} correspond to initial-state core-level shifts as obtained within a first-order perturbation scheme [112]. In this perspective, the term ΔE_{b} corresponds to the difference between the final-state core-hole relaxation energies in the two components.

We thus first address the initial-state shift by focusing on the potential offset ΔV_{ref} across the interface models. For both interfaces, we find that a $3 \times 3 \times 1$ **k**-point mesh yields fully converged initial-state shifts[2]. The calculated initial-state shifts of the Ge core-levels are

---

2. A denser mesh yielded changes of initial core-level shifts lower than 5 meV. A single k-point was used in the z
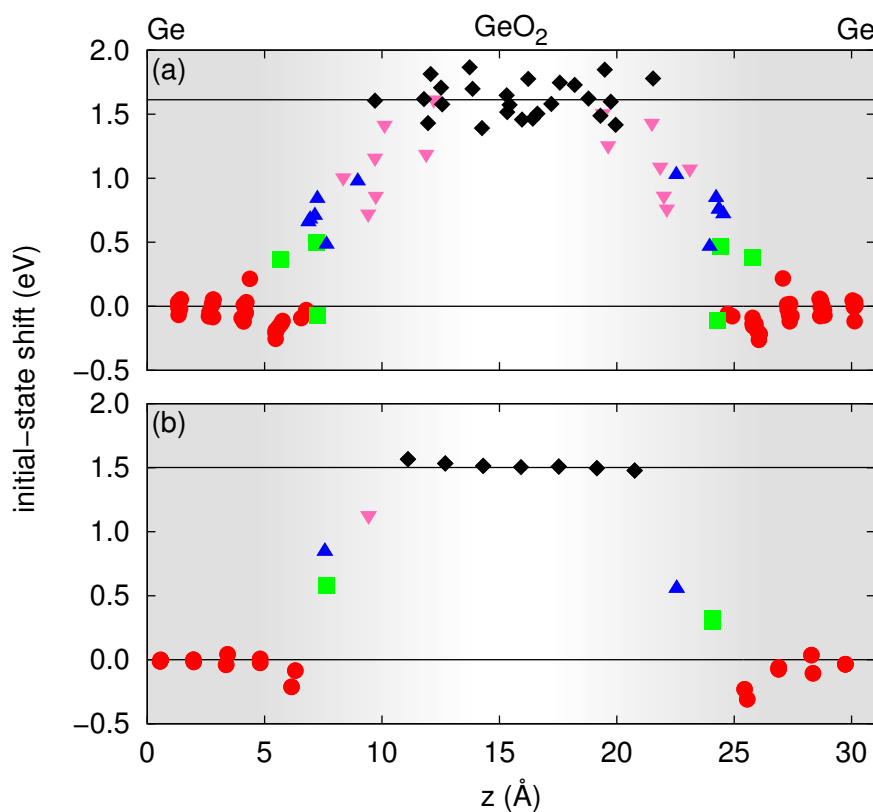
Figure 7.8 – Initial-state Ge $3d$ core-level shifts across the Ge/GeO$_2$ interface as obtained within the PBE functional, for the model interface (a) with an amorphous oxide and (b) with a crystalline oxide, respectively. The various oxidation states are labeled: Ge^0 (disks, red), Ge^{+1} (squares, green), Ge^{+2} (upwards-pointing triangles, blue), Ge^{+3} (downwards-pointing triangles, magenta), and Ge^{+4} (diamonds, black). The shifts are referred to the average shift of the central four Ge layers (lower horizontal line). The upper horizontal line corresponds to the average shift of the Ge^{+4} oxidation state in the central region of the oxide (13 Å < z < 19 Å).

shown in Fig. 7.8 for both our interface models. For the interface with an amorphous oxide, we find an initial-state shift of 1.6 eV when going from the center of the Ge layer to the center of the oxide layer. The interface with a crystalline oxide yields approximately the same value (1.5 eV). The initial-state shifts associated to intermediate oxidation states appear to be regularly spaced between the two limiting cases.

To accurately determine $E_{\rm b}^{\rm Ge}$ in bulk Ge, we use cubic supercells of two different sizes (64 and 216 atoms). For each cell, the **k**-point sampling is increased symmetrically in all directions until the binding energies are found to be converged. For the 64-atom and 216-atom cells, we determine electrostatic corrections of 0.11 and 0.07 eV, respectively [95]. The scaling is fully consistent with the behavior of a point charge, thus allowing for straightforward extrapolation.

direction because of the slab geometry. Furthermore, this results in an isotropically uniform k-point density.

Table 7.10 – Core-level separation ΔE_{XPS} between Ge^0 and Ge^{+4} oxidation states across the Ge/GeO$_2$ interface, as obtained through the potential alignment method. We use two interface models which are distinguished by the nature of the oxide. The total core-level shift ΔE_{XPS} is the sum of the difference in initial-state shift (ΔV) and in core-hole relaxation energy (ΔE_{b}) between the two interface components [cf. Eq. (7.4)]. The calculations are performed with PBE and PBE0 functionals. Energies are in eV.

Interface	Functional	ΔV	ΔE_{b}	ΔE_{XPS}
amorphous	PBE	1.60	0.94	2.54
β-cristobalite	PBE	1.50	1.13	2.63
amorphous	PBE0	1.54	1.22	2.76
β-cristobalite	PBE0	1.52	1.23	2.75

Determining $E_{\text{b}}^{\text{GeO2}}$ depends to some extent on the bulk model adopted for the oxide. We here consider two bulk GeO$_2$ structures which consistently reflect the respective structural arrangements in the two interface models. The first oxide structure corresponds to a model of amorphous GeO$_2$ generated previously via first-principles molecular dynamics [31, 19]. The structure contains 126 atoms at the experimental density (3.64 g/cm^3) in a periodically repeated cubic unit cell and is composed of cornersharing Ge(O$_{1/2}$)$_4$ tetrahedra. The second oxide structure that we consider corresponds to the crystalline β-cristobalite phase. We ensure that our bulk model preserves the same structural arrangement found in the respective interface model. In this way, we construct two almost cubic supercells containing 48 and 384 atoms. The **k**-point sampling in the Brillouin zone is increased until full convergence of the desired binding energies is achieved. However, it is found that Γ-point sampling is always sufficient, leading to errors of only 8 meV in the worst case, corresponding to the oxide with 48 atoms. For eliminating the spurious electrostatic interactions, we use Makov-Payne corrections [95]. For the amorphous model, this leads to an increase of the calculated binding energy by 0.58 eV. For the crystalline models of 48 and 384 atoms, the Makov-Payne corrections are 0.90 and 0.45 eV, respectively. The scaling is fully consistent with the point-charge behavior, thereby validating the use of these corrections.

In our pseudopotential approach, only the difference E_{b} between the binding energies in bulk Ge and bulk GeO$_2$ is physically meaningful and represents the difference in core-hole relaxation energy between the two interface components. The calculated values together with the initial-state shifts are given in Table 7.10. The total core-level shift ΔE_{XPS} is obtained according to Eq. (7.4) and is found to be 2.5 eV for the interface with the amorphous oxide and 2.6 eV for the interface with the crystalline oxide. The two final values are thus very close, despite a slightly larger difference of about 0.2 eV found for the core-hole relaxation energies in the two bulk oxides.

To improve upon the PBE description, we also calculate the core-level separation ΔE_{XPS} with the hybrid PBE0 functional. The atomic structures obtained with the PBE functional are

preserved without allowing for further relaxation, as this does not lead to any deterioration of the accuracy (cf. Sec. 7.2). The calculation of the initial-state shifts in the interface models is performed with a **k**-point sampling restricted to the sole Γ point, to further alleviate the numerical cost. On the basis of PBE calculations with the same settings, this entails deviations of 0.1 eV with respect to full convergence for ΔV. Assuming that the **k**-point sampling errors do not depend on the functional, we use the PBE deviations to correct to PBE0 values of ΔV. Table 7.10 shows that the initial-state shifts obtained in the PBE0 differ by less than 0.1 eV from those obtained in the PBE.

For the determination of the core-hole relaxation term ΔE_b, the **k**-point sampling in the Ge bulk calculation is performed with the Baldereschi point [12], while the Γ-point is used for the bulk oxide models. On the basis of our PBE results, this reduced sampling does not give errors larger than 10 meV for ΔE_b. As shown in Table 7.10, the calculated values of ΔE_b in the PBE0 are slightly larger than in the PBE. In conclusion of this section, we thus find that the potential alignment method yields, for both interface models, a full core-level shift ΔE_XPS of 2.75 eV at the PBE0 level of theory, up to 0.1–0.2 eV larger than found in the PBE.

Direct calculation of core-level shift followed by electrostatic correction

In this section, the Ge core-level shifts including the core-hole relaxation are directly determined through calculations involving the Ge/GeO$_2$ interface models. All calculations in this section are performed with the pseudopotential-plane-wave scheme, both at the PBE and PBE0 levels of theory. Since the interface models are in the superlattice geometry and subject to periodic boundary conditions, the dielectric environment affecting the core-hole relaxation is different than for an isolated interface. This difference is here accounted for within a classical electrostatics model and then used to correct the calculated values.

Core-level shifts are directly calculated for our two interface models. For both interfaces, we use a $3 \times 3 \times 1$ **k**-point mesh. The calculated shifts are given in Fig. 7.9. In the PBE, the average separation ΔE_XPS between the core-levels of Ge^0 and Ge^{+4} oxidation states is found to be ~2.0 eV for both interfaces (cf. Table 7.11). The shifts of the intermediate oxidation states lie in between, but the spacing between their average levels is no longer constant and increases with oxidation state, as the Ge screening becomes progressively less effective at increasing distance from the substrate.

Using the same atomic structures obtained in the PBE, we also perform core-level shift calculations at the PBE0 level for representative atoms chosen in the Ge and GeO$_2$ regions of the superlattice models (cf. Fig. 7.9). In these calculations, the Brillouin zone is sampled at the sole Γ point, but convergence corrections of the order of 0.08 eV are estimated from analogous calculations at the PBE level and incorporated in the final PBE0 result. As can be seen in Table 7.11, the values of ΔE_XPS obtained in the direct PBE0 calculations are larger than those obtained in the respective PBE calculations by 0.2–0.3 eV.
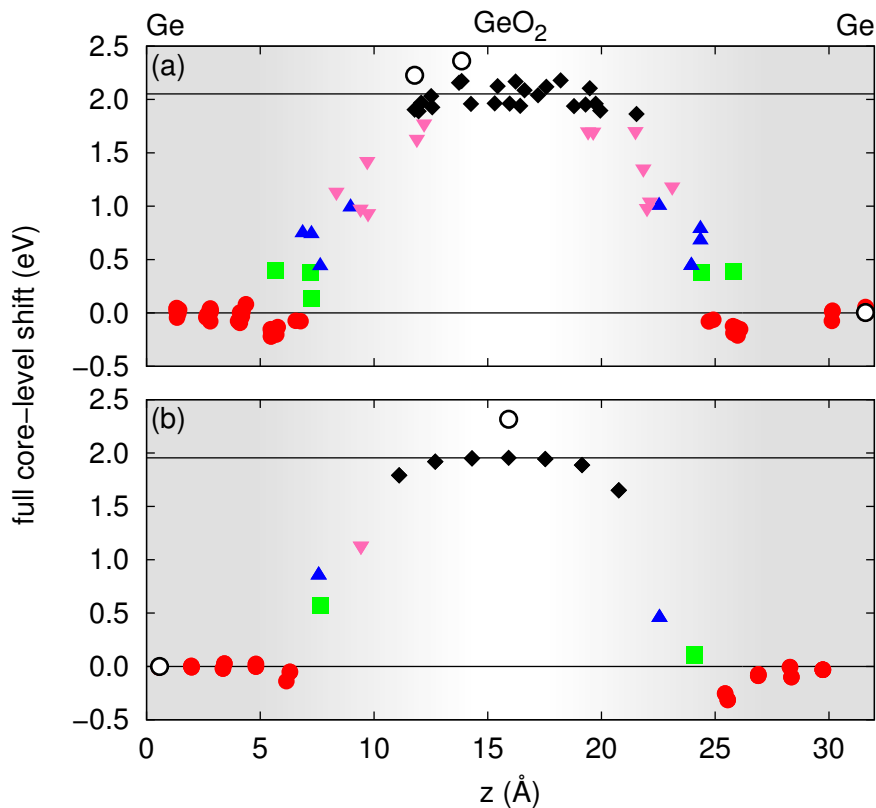
Figure 7.9 – Full Ge $3d$ core-level shifts across the Ge/GeO$_2$ interface as obtained in the PBE, for the model interface (a) with an amorphous oxide and (b) with a crystalline oxide. Same notation as in Fig. 7.8. The three open circles correspond to calculations performed with the PBE0 functional.

In these direct calculations, the total energy is obtained for a system with a positively charged core hole. The use of periodic boundary conditions requires the use of a uniform background charge to achieve charge neutrality in the simulation cell. Furthermore, the physical environment determined by the superlattice model significantly differs from the actual environment due to a single interface. Hence, such calculations suffer from finite-size effects which are difficult to eliminate because of the long-range nature of the Coulomb potential. While several correction schemes have been proposed in the literature to deal with such effects in homogeneous dielectric media [95, 87, 52], similar schemes to treat dielectrically discontinuous systems have remained far less explored.

In the following, we develop such a correction scheme for interfaces in the superlattice geometry within a classical electrostatics model. In such a classical model, the interface components are distinguished by their dielectric constants and the core hole relaxation energy corresponds to the polarization energy of a positive unit charge. More specifically, we are interested in comparing the dielectric relaxation energy E_{per} of a core hole found in the middle of one

Table 7.11 – Core-level separation ΔE_{XPS} between Ge^0 and Ge^{+4} oxidation states across the Ge/GeO$_2$ interface, as obtained through direct calculation followed by classical electrostatics correction. We use two interface models which are distinguished by the nature of the oxide. The uncorrected results as obtained via direct calculations and the corrections pertaining to shifts on the Ge (δ_{Ge}) and GeO$_2$ (δ_{GeO_2}) sides of the interfaces are also provided. Calculations are performed with PBE and PBE0 functionals. Energies are in eV.

Interface	Functional	Corrections		ΔE_{XPS}	
		δ_{Ge}	δ_{GeO_2}	Direct	Corrected
amorphous	PBE	0.03	0.33	2.05	2.41
β-cristobalite	PBE	0.01	0.36	2.00	2.37
amorphous	PBE0	0.03	0.33	2.23	2.59
β-cristobalite	PBE0	0.01	0.36	2.30	2.66

of the superlattice layers with the respective energy E_{iso} of an isolated core hole in a bulk medium having the same dielectric constant as the layer. The desired correction is then given by $\delta = E_{\text{iso}} - E_{\text{per}}$. In our case, we need one such a correction for the Ge layer, δ_{Ge}, and one for the GeO$_2$ layer, δ_{GeO_2}.

For numerical convenience, the charge representing the core-hole is modeled by a normalized Gaussian charge distribution centered at $\mathbf{r}_0$,

$$\rho(\mathbf{r}) = \frac{1}{\sqrt{2\pi\sigma^2}} e^{-(\mathbf{r}-\mathbf{r}_0)/(2\sigma^2)} \tag{7.8}$$

where σ is the spread of the function and is taken to be equal to 1 bohr unless mentioned otherwise. The electrostatic energy of interest can be expressed as

$$U = \frac{1}{2} \int d^3 r' \rho(\mathbf{r}') V(\mathbf{r}') \tag{7.9}$$

where V is the electrostatic potential. This energy corresponds to the self-energy of the Gaussian charge distribution in the specified dielectric environment.

The determination of the electrostatics correction consists in determining the difference between the self-energy in a homogeneous dielectric medium and that in a periodic model representing the interface. In a homogeneous dielectric medium with a dielectric constant ϵ, the electrostatic self-energy U of the Gaussian charge distribution can be obtained analytically and corresponds to:

$$E_{\text{iso}}(\epsilon) = \frac{1}{2\sigma\epsilon\sqrt{\pi}}. \tag{7.10}$$
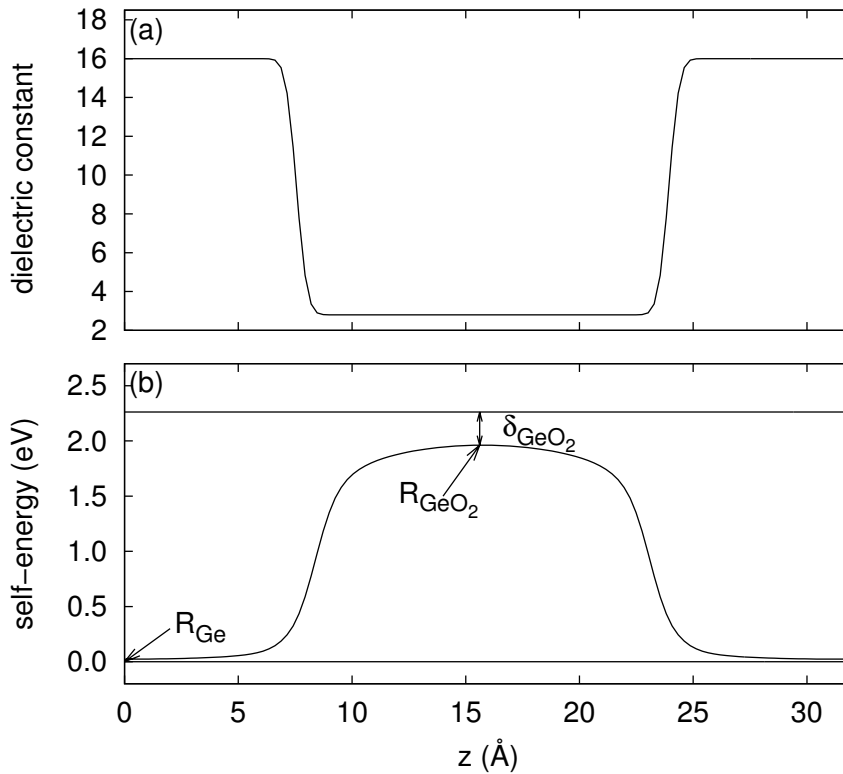
Figure 7.10 – (a) Local dielectric constant across the periodically repeated simulation cell varying nearly abruptly between the dielectric constant of Ge and that of GeO_2. (b) Electrostatic self-energy of a Gaussian charge distribution with $\sigma = 1$ bohr as its center varies across the periodically repeated simulation cell. The electrostatic energies E_{iso} corresponding to the same charge distribution in homogeneous dielectrics with dielectric constants of Ge and of GeO_2 are indicated by horizontal lines. The electrostatic corrections δ_{GeO_2} and δ_{Ge} are evaluated in the central positions R_{GeO_2} and R_{Ge} of the respective layers.

In our classical electrostatics description, the superlattice model consists of alternating layers with dielectric constants of 16 for Ge and of 2.8 for GeO_2, as illustrated in Fig. 7.10(a). The local dielectric constant $\epsilon(z)$ varies smoothly for facilitating its numerical treatment, but the region of variation is taken to be much smaller than other distances involved. The size of the periodically repeated simulation cell and the thickness of the layers are set as in the density-functional calculation, unless mentioned otherwise. In this periodic simulation cell, the Gaussian charge distribution is compensated by a uniform background of opposite charge to avoid the divergence of the energy. The potential V appearing in Eq. (7.9) is obtained by addressing the Poisson equation for this system:

$$\nabla \cdot [\epsilon(\mathbf{r}) V(\mathbf{r})] = -\rho(\mathbf{r}) \tag{7.11}$$

Table 7.12 – Corrections δ_{Ge} and $\delta_{\mathrm{GeO_2}}$ from classical electrostatics for various spreads σ of the Gaussian charge distribution. The corrections $\delta = E_{\mathrm{iso}} - E_{\mathrm{per}}$ are evaluated at the center of the respective layers in a simulation cell which corresponds to that used in the density functional calculations.

σ (bohr)	δ_{Ge} (eV)	$\delta_{\mathrm{GeO_2}}$ (eV)
0.5	0.129	−0.106
1.0	0.130	−0.103
1.5	0.131	−0.097

or, equivalently,

$$\epsilon(\mathbf{r})\nabla^2 V(\mathbf{r}) + \nabla\epsilon(\mathbf{r}) \cdot \nabla V(\mathbf{r}) = -\rho(\mathbf{r}). \tag{7.12}$$

We solve this equation numerically by describing the charge density and the potential on a three-dimensional mesh with a uniform spacing of 0.5 bohr[3].

The potential is then used in Eq. ((7.9)) to obtain U, which in this case corresponds to the electrostatic self-energy $E_{\mathrm{per}}(z)$. We note that the self-energies defined by U in Eq. (7.9) depend on the spread σ and diverge for $\sigma \to 0$. On the opposite, the corrections $\delta = E_{\mathrm{iso}} - E_{\mathrm{per}}$ do not depend on σ insofar the distances to the interfaces are signficantly larger than σ. This is numerically confirmed in Table 7.12.

Figure 7.10(b) shows the evolution of the electrostatic self-energy $U(z_0)$ as the center z_0 of the Gaussian charge distribution varies across the simulation cell. The corrections $\delta_{\mathrm{GeO_2}}$ and δ_{Ge} are obtained by taking the difference between the self-energy calculated in the middle of the layers and the respective self-energies pertaining to the homogeneous bulk media, $E_{\mathrm{iso}}(\epsilon_{\mathrm{GeO_2}})$ and $E_{\mathrm{iso}}(\epsilon_{\mathrm{Ge}})$. We note that the correction is much larger in the GeO$_2$ than in the Ge layer, where the high dielectric constant effectively screens the inserted charge on a short distance.

We note that the correction defined in this way does not only correct the spurious electrostatic interactions due to the periodic boundary conditions but also eliminates the residual physical electrostatics effects due to the proximity of the interfaces in the periodic model. The latter feature satisfies our target of achieving by this correction the core-level shift between atoms situated on opposite sides of the interface but at large distances from the interface itself. Thus, the corrections defined in this way aim at achieving the same final result as that obtained through the potential alignment method applied in Sec. 7.3.

To check the validity of the adopted corrections, we investigate how they perform for increasing lateral dimension of the periodic simulation cell. First, we calculate within classical electrostatic, the corrections $\delta_{\mathrm{GeO_2}}$ and δ_{Ge} for a periodic superlattice model with alternating layers of homogeneous dielectrics with dielectric constants equal to 16 (Ge) and 2.8 (GeO$_2$). Figure 7.11

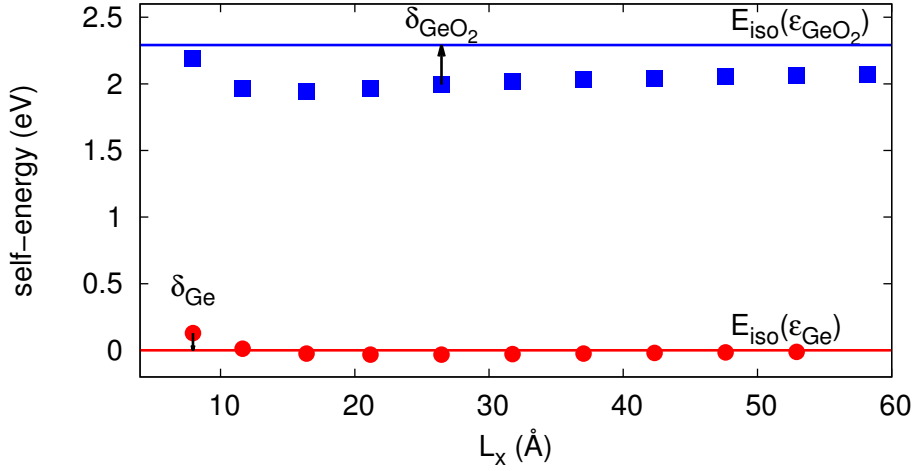3. The actual calculation is than done in reciprocal space.

Figure 7.11 – Electrostatic self-energy E_{per} of a Gaussian charge distribution (with spread $\sigma=1$ bohr) calculated for a periodic model interface of alternating layers of two homogeneous dielectrics with dielectric constants equal to 16 (Ge) and 2.8 (GeO$_2$). The self-energy E_{per} is evaluated at the center of the Ge (disks, red) and of the GeO$_2$ (squares, blue) layers for varying lateral dimension L_x of the supercell ($L_y = L_x$). The thicknesses of the layers is kept fixed and correspond to those used in the density functional simulation cell. The horizontal lines indicate the self-energy of an isolated Gaussian charge distribution $E_{iso}(\epsilon)$ in a homogeneous medium of dielectric constant ϵ. The arrows illustrate the definition of the correction terms δ_{GeO_2} and δ_{Ge}. $E_{iso}(\epsilon_{Ge})$ is taken as reference.

shows the self-energy of a Gaussian charge distribution at the center of the respective layers as a function of the lateral dimension L_x ($L_y = L_x$). The size of the supercell in the vertical direction is kept fixed and identical to that in the density-functional calculations. On the GeO$_2$ side, the correction reaches values up to 0.35 eV for the range of L_x considered. On the Ge side, the correction δ_{Ge} is much smaller.

We then construct a series of periodic interface models with crystalline oxides showing interfacial repeat units of varying size. In particular, we consider square repeat units containing 4, 8, 16, and 32 Ge atoms, which correspond to lateral dimensions L_x of 8.2, 11.6, 16.4, and 23.2 Å, respectively. For all these models, we calculate the total energies for Ge $3d$ core holes located in the middle of the Ge and GeO$_2$ layers and derive the corresponding shift ΔE_{XPS} between Ge^0 and Ge^{+4} oxidation states. In these calculations, convergence with **k**-point sampling is ensured. The calculated values are reported in Fig. 7.12 as a function of the lateral side of the supercell. The calculated core-level shift is found to increase monotonically with lateral side. At variance, when the corrections from classical electrostatics δ_{GeO_2} and δ_{Ge} from Fig. 7.11 are added to the calculated shifts, one clearly observes that the shifts reach convergence. In particular, at $L_x = 11.6$ Å, corresponding to the side used for the Ge/GeO$_2$ interface models in Sec. 7.3, the deviation from the converged result is lower than 0.03 eV. The larger deviations
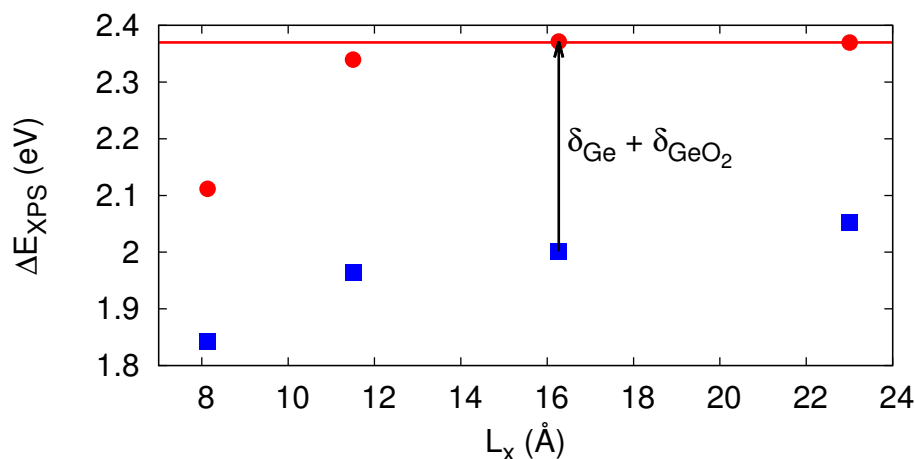
Figure 7.12 – Ge $3d$ core-level shifts (squares, blue) calculated within the PBE functional for a series of periodic Ge/GeO$_2$ interface models with crystalline oxides showing different lateral dimensions L_x ($L_y = L_x$). The periodicity and the layer thicknesses in the vertical direction are kept fixed and correspond to the model introduced in Sec. 7.3. The core-level shift is taken between atoms at the centers of the Ge and GeO$_2$ layers. Core-level shifts including δ_{GeO_2} and δ_{Ge} corrections from classical electrostatics (cf. Fig. 7.11) are also shown (disks, red). The horizontal line corresponds to the converged result inferred from the calculations.

at $L_x = 8.2$ Å indicate that classical electrostatics give insufficient corrections and suggest that quantum-mechanical effects due to the relatively close periodic images might still be operative [140].

From the present analysis, we infer that the model interfaces with a lateral side of $L_x = 11.6$ Å give sufficiently accurate results provided the corrections of classical electrostatics are included. These corrections apply indifferently to core-level shifts calculated in the PBE and in the PBE0. The corrected values of the ΔE_{XPS} shifts for the two model interfaces considered are reported in Table 7.11. The two interface models give consistent values, around 2.4 in the PBE and around 2.6–2.7 eV in the PBE0.

7.4 Discussion and conclusion

Table 7.13 summarizes the main result of this work which corresponds to the theoretical determination of the Ge $3d$ core-level shift ΔE_{XPS} between Ge^0 and Ge^{+4} oxidation states at the Ge/GeO$_2$ interface. This shift is calculated through two different methods and for two different interface models. We find a rms deviation of 0.18 eV between the two different methods. Since the two applied methods target the same physical quantity ΔE_{XPS}, this residual deviation solely reflects the numerical difficulty in achieving a converged result for a given interface model.

Table 7.13 – Comparison between calculated core-level shift ΔE_{XPS} for the two interface models considered in this work as obtained through the potential alignment method (Sec. 7.3) and through direct calculation with addition of electrostatic corrections (Sec. 7.3). The calculations refer to PBE and PBE0 functionals. Energies are in eV.

Interface	Functional	Potential alignment	Direct with corrections
amorphous	PBE	2.54	2.41
β-cristobalite	PBE	2.63	2.37
amorphous	PBE0	2.76	2.59
β-cristobalite	PBE0	2.75	2.66

The difference between the two interface structures is always smaller than 0.1 eV, despite the different interfacial bond pattern in the two models. Nevertheless, the two models also have features in common. Indeed, both interface structures show no coordination defects and a similar bond density reduction, thus reproducing the main features of their parent Si/SiO_2 interface models. Hence, the close agreement for ΔE_{XPS} further confirms that the interface dipole does not differ significantly among models satisfying such conditions, as previously found in investigations on band offsets [33, 57].

Considering on the same footing the results obtained for different models and through different methods, we find $\Delta E_{XPS} = 2.49$ eV in the PBE and $\Delta E_{XPS} = 2.69$ eV in the PBE0, with respective rms deviations of 0.10 and 0.07 eV. In the following, the discussion is based on the result obtained in the PBE0, which is expected to yield a closer agreement with experiment (cf. Sec. 7.2).

Experimental determinations of ΔE_{XPS} are found to depend on the growth procedure used for the Ge/GeO_2 interface. Interfaces with oxides grown by thermal oxidation in O_2 atmosphere generally give $\Delta E_{XPS} \cong 3.3$ eV [129, 124, 106, 42, 101, 79], but much larger values (3.7–3.8 eV) are found in experiments in which the oxidation is achieved with O_3 and atomic O [119, 158]. Our PBE0 value of 2.7 eV is significantly lower than all available experimental determinations. The discrepancy is much larger than both the numerical error with which we determine ΔE_{XPS} and the expected accuracy associated to the PBE0 level of theory. This leads to the conclusion that the Ge/GeO_2 interface structure differs from those represented by the adopted model structures. In other terms, the interface structure that appears to give a satisfactory description of the Si/SiO_2 interface[24, 159] does not provide an acceptable description of the *a priori* analogous Ge/GeO_2 interface.

This conclusion, which follows from the comparison between theoretical and experimental ΔE_{XPS}, reinforces an analogous conclusion reached on the basis of a comparison between calculated and measured valence band offsets in chapter 6. Indeed, we determined a valence band offset of 3.4 eV for one of the model interface structures studied in the present work in
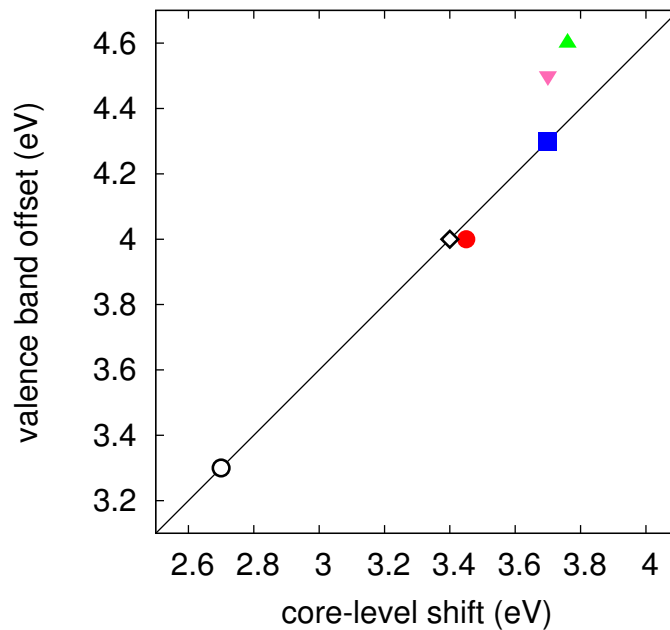
Figure 7.13 – (Color online) Ge 3d core-level shift ΔE_{XPS} and valence band offset (VBO) as determined theoretically (open symbols) and experimentally (closed symobols) for a given Ge/GeO$_2$ interface model or sample. The circle corresponds to the model interface with an amorphous oxide (ΔE_{XPS} from the present work and VBO from chapter 6.2. The straight line is consistent with our calculated values but allows for an undetermined contribution to the interface dipole, e.g. as resulting from the valence alternation pair in Ref. [33] (diamond). The VBOs corresponding to the red disk (Ref. [106]) and the blue square (Ref. [119]) are obtained through valence-band photoemission, while those corresponding to the magenta downwards-pointing (Ref. [119]) and green upwards-pointing triangles (Ref. [158]) are derived through Kraut's method.

chapter 6. This value is significantly lower than found in experimental studies which yield values ranging between 4.0 and 4.5 eV [106, 119, 158].

In Fig. 7.13, calculated and measured values are compared in a VBO-ΔE_{XPS} plot. Only experimental data corresponding to ΔE_{XPS} and VBO determined for the same sample are considered. The experimental VBOs are either determined through valence-band photoemission or through the use of Kraut's method. The spread of the available experimental data clearly indicates that the interface dipole depends on the sample at hand. However, an uncontrolled contribution to the interface dipole affects the core-level shift and the valence band offset by the same amount. It is therefore meaningful to compare the calculated results with experiment allowing for an undetermined contribution to the interface dipole. This results in the straight line in Fig. 7.13. Overall, the available experimental results are consistent with the intrinsic relation between ΔE_{XPS} and VBO found in the calculation. In particular, the data corresponding to VBOs measured through valence-band photoemission show excellent agreement, while the VBOs obtained with Kraut's method are only slightly larger. This result strengthens the results

of our calculations and suggests that the difference between the theoretical and the various experimental interface structures only lies in their interface dipole.

The actual interface structure at Ge/GeO_2 interfaces remains an open question. There have been several investigations indicating that substoichiometric germanium oxide is intrinsically different than its silicon counterpart [16, 143, 17, 92, 20]. In particular, we performed first-principles molecular dynamics on substoichiometric GeO_x finding a structure with a high concentration of negatively charged threefold coordinated Ge atoms and positively charged threefold coordinated O atoms (cf. chapter 3). Bonding motifs of this kind carrying opposite charge are known as valence alternation pairs [76]. In chapter 6, we have shown that when these pairs are properly oriented with respect to the interface a sizeable contribution to the interface dipole can be obtained. This offers a possible interpretation scheme which could reconcile the theoretical and experimental values for ΔE_{XPS} and the VBO. However, also other mechanisms might affect the interface dipole, such as the charge trapping in point defects or the occurrence of high or low density layers in the transition region. It should be noted that the interface dipole required to move in the direction of the experimental data should oppose the natural dipole created by the electronegativity difference in the Ge-O bond.

In summary, this work focuses on the Ge $3d$ core-level shift at Ge/GeO_2 interfaces. It is first demonstrated that such core-level shifts are reliably described within semilocal and hybrid density functional schemes through comparison with experiment for a set of Ge-based molecules. Then, the numerical problem consisting in determining such shifts for interface models subject to periodic boundary conditions is addressed. Two different strategies are pursued and found to yield consistent results. The most reliable theoretical estimate of the Ge $3d$ core-level shift is found to be significantly lower than found in experimental studies. However, the theoretical core-level shift is found to deviate from measured shifts in the same way as the calculated valence band offset does from respective experimental data. This result suggests that the theoretical relation between core-level shift and valence band offset is consistent with experimental data. The deviation from experiment resides in the actual interface dipole at the interface, which is apparently not well reproduced in the structural models of the Ge/GeO_2 interface used so far. Since these models are inspired from the structure at the Si/SiO_2 interface, we reach the conclusion that the atomic structure at Ge/GeO_2 interfaces must be inherently different. Identifying the bonding pattern at this interface appears as a prioritary issue in view of envisaging valid strategies for defect passivation.

8 Conclusion

The present thesis addresses the Ge/GeO$_2$ interface, with particular focus on the interfacial region between Ge and GeO$_2$. The actual interface structure at Ge/GeO$_2$ interfaces remains an open question. There are several results indicating that substoichiometric germanium oxide is intrinsically different than its silicon counterpart. In particular in chapter 3, we calculated deviations from the bond energy picture for a set of crystalline models representing different oxidation states. The so called penalty energies for substoichiometric GeO$_x$ are found to be significant smaller than corresponding penalty energies for SiO$_x$ structures. Furthermore, the oxygen vacancy formation energies at a Si/SiO$_2$/HfO$_2$ interface and at its germanium counterpart are compared. We found a higher stability of the vacancy for all relevant chemical potentials at the germanium-based interface. These two studies indicate, that the formation of an interfacial region at the Ge/GeO$_2$ interface is more favored than at the Si/SiO$_2$ interface.

To model the amorphous oxide region, we performed first-principles molecular dynamics (MD) for different oxygen concentrations. For substoichiometric GeO, we found a structure with high concentrations of negatively charged threefold coordinated Ge atoms and of positively charged threefold coordinated O atoms (see chapter 4). Bonding motifs of this kind carrying opposite charge are known as valence alternation pairs [76]. The energetics of the MD structures are similar to regularly bonded GeO structures generated with a bond switching Monte Carlo scheme. This suggests, that the interfacial structure at the Ge/GeO$_2$ interface contains a mixture of both structural types. This suggestion is further supported by a MD structure generated via hybrid density functional molecular dynamics.

Differences between the two structure types appear, when charge trapping is considered. In chapter 5.1, we demonstrate that the MD structure is prone to electron and hole trapping. The trapping states correspond to the formation and breaking of Ge–Ge bonds. We calculate charge transition levels for electron and hole trapping for two different values of valence band offset (VBO) corresponding to experimental observations. When a large VBO is adopted (4.5 eV), the $\epsilon(0/-)$ level appears in the middle of the Ge band gap, which might explain the bad performance of n-type doped Ge devices. The $\epsilon(+/0)$ charge transition level lies at the Ge valence band edge in the case of high VBO, while it falls within the band for lower VBOs. Thus,

it is expected that this level does not affect the electrical performance of the device.

Next, we decompose the hole trapping reaction in elementary steps and find excellent agreement with energies obtained from model structures. We use elementary reactions to find the cost for breaking a Ge–Ge bond and to form a VAP. These reaction energies are dependent on the oxygen concentration. VAPs across the interface are energetically preferred in low oxygen concentrations. However, estimated energies for VAP formation are larger (by ~ 1 eV) than the Ge–Ge bond level. A large part of the missing energy can probably be assigned to strain effects in our model systems. A further stabilization effect might be related to the concentration of VAPs. As seen in chapter 5.3 dangling bond passivation with H atoms is effective for a single VAP in an otherwise regularly bonded GeO structure, whereas the charge transition level of H^+ in the MD structure is 0.7 eV higher. This suggests an additional cooperative stabilization effect between the VAPs which goes beyond the description of elementary reactions. This extra stabilization effect would also explain the equivalent energies of the MD structures and the regularly bonded disordered models.

In chapter 6, we calculate the valence band offset for an atomistic model structure of the Ge/GeO_2 interface. The model is obtained from a Si/SiO_2 model interface showing an amorphous oxide. The obtained value of 3.4 eV is smaller than experimental VBOs for the Ge/GeO_2 interface. We show, that when VAPs are properly oriented with respect to the interface a sizeable contribution to the interface dipole can be obtained. In VAPs, positive charge centers are related to O atoms, whereas negative charge centers are related to Ge atoms. This suggest a natural order of VAPs across the interface, where positive charges are in the oxide and negative charges are on the Ge side. This order guarantees that the dipole created by the electronegativity differences in the Ge–O bond is reduced, and results in an increase of the VBO at the Ge/GeO_2 interface.

A large spread of X-ray photoemission spectroscopy data for the Ge/GeO_2 interface is experimentally observed. In chapter 7 we calculate Ge core-level shifts for a wide range of Ge-based systems: excited atomic states, molecules, surfaces, and two Ge/GeO_2 interfaces. The first systems are used to demonstrate the accuracy of our theoretical scheme. We found excellent agreement with experimental XPS shifts for the molecules and the surface. The core-level shift between the two oxidation states Ge^0 and Ge^4 at the Ge/GeO_2 interface was found to be 2.7 eV. Experimental determinations of ΔE_{XPS} are found to depend on the growing procedure used for the Ge/GeO_2 interface. Interfaces with oxides grown by thermal oxidation in O_2 atmosphere generally give $\Delta E_{XPS} \cong 3.3$ eV [129, 124, 106, 42, 101, 79], but much larger values (3.7–3.8 eV) are found in experiments in which the oxidation is achieved with O_3 and atomic O [119, 158]. Our PBE0 value of 2.7 eV is significantly lower than all available experimental determinations. Hence, the interface structure that appears to give a satisfactory description of the Si/SiO_2 interface [24, 159] does not provide an acceptable description of the *a priori* analogous Ge/GeO_2 interface. For instance we attribute a missing contribution to the interface dipole of ~ 0.6 eV which would consistently correct both the VBO and the XPS shift. VAPs are possible candidates to explain the reduced interface dipole.

A direct experimental confirmation of VAPs seems to be difficult. Device characterization schemes based on electrical measurements are insufficient. These techniques allow just to count the number of defects inside the Ge band gap. Since neutral VAPs show no states in the Ge band gap, they cannot be detected with such measurements. Electron spin resonance (ESR) used to characterize dangling bonds at the Si/SiO_2 interface does not give any dangling-bond signal at the Ge/GeO_2 interface [1]. Doubly occupied Ge dangling bonds, which are not paramagnetic and therewith not ESR active might be responsible for this, but there are also other explanations [151, 27, 71]. An indication for the occurrence of threefold coordinated O atoms has been found in a valence band photoemission experiment on thin substoichiometric GeO_x layers through a backwards shift of the O $2p$ peak [14].

We have shown, that hybrid density functional methods can be used to calculate accurate VBOs and core-level shifts for model interfaces. We found significant differences between the Ge/GeO_2 interface and the Si/SiO_2 interface. For a detailed understanding of the Ge/GeO_2 interface a systematic physical characterization is needed. In particular, Ge/GeO_2 interfaces realized with different growth procedures should be distinguished. Only through such a detailed experimental analyse combined with atomistic simulations, we could enhance our detailed understanding of the structure of the Ge/GeO_2 interface, and eventually make the realization of a Ge-based device possible.

Bibliography

[1] V. V. Afanas'ev, Y. G. Fedorenko, and A. Stesmansan, *Interface traps and dangling-bond defects in (100)Ge/HfO$_2$*, Appl. Phys. Lett. **87** (2005), 032107.

[2] V. V. Afanas'ev and A. Stesmans, *Energy band alignment at the (100)Ge/HfO$_2$ interface*, Appl. Phys. Lett. **84** (2004), 2319.

[3] ———, *Spectroscopy of electron states at interfaces of (100)Ge with high-κ insulators*, Mater. Sci. Semicond. Process. **9** (2006), 764.

[4] V. V. Afanas'ev, A. Stesmans, A. Delabie, F. Bellenger, M. Houssa, and M. Meuris, *Electronic structure of GeO$_2$-passivated interfaces of (100)Ge with Al$_2$O$_3$ and HfO$_2$*, Appl. Phys. Lett. **92** (2008), 022109.

[5] Audrius Alkauskas, Peter Broqvist, Fabien Devynck, and Alfredo Pasquarello, *Band offsets at semiconductor-oxide interfaces from hybrid density-functional calculations*, Phys. Rev. Lett. **101** (2008), 106802.

[6] Audrius Alkauskas, Peter Broqvist, and Alfredo Pasquarello, *Defect energy levels in density functional calculations: Alignment and band gap problem*, Phys. Rev. Lett. **101** (2008), 046405.

[7] ———, *Defect levels through hybrid density functionals: Insights and applications*, Phys. Status Solidi B **248** (2011), 775.

[8] Audrius Alkauskas and Alfredo Pasquarello, *Band-edge problem in the theoretical determination of defect energy levels: The o vacancy in ZnO as a benchmark case*, Phys. Rev. B **84** (2011), 125206.

[9] Wanda Andreoni and Alessandro Curioni, *New advances in chemistry and material science with CPMD and parallel computing*, Parallel Computing **26** (2000), 819.

[10] Neil W. Ashcroft and David N. Mermin, *Solid state physics*, 1 ed., Thomson Learning, 1976.

[11] Albert A. Bakke, Hsiang-Wen Chen, and William L. Jolly, *A table of absolute core-electron binding-energies for gaseous atoms and molecules*, J. Electron Spectrosc. Relat. Phenom. **20** (1980), 333.

[12] Alfonso Baldereschi, *Mean-value point in the brillouin zone*, Phys. Rev. B **7** (1973), 5212.

Bibliography

[13] Alfonso Baldereschi, Stefano Baroni, and Raffaele Resta, *Band offsets in lattice-matched heterojunctions: A model and first-principles calculations for gaas/alas*, Phys. Rev. Lett. **61** (1988), 734.

[14] Tery L. Barr, Mehran Mohsenian, and Li Mei Chen, *Xps valence band studies of the bonding chemistry of germanium oxides and related systems*, Appl. Surf. Sci. **51** (1991), 71.

[15] Axel D. Becke, *A new mixing of Hartree-Fock and local density-functional theories*, J. Chem. Phys. **98** (1993), 1372.

[16] Jan Felix Binder, Peter Broqvist, and Alfredo Pasquarello, *First principles study of substoichiometric germanium oxides*, Microelectron. Eng. **86** (2009), 1760.

[17] _____ , *Electron trapping in substoichiometric germanium oxide*, Appl. Phys. Lett. **97** (2010), 092903.

[18] _____ , *Charge trapping in substoichiometric germanium oxide*, Microelectron. Eng. **88** (2011), 1428.

[19] _____ , *Electron density of states at ge/oxide interfaces due to geox formation*, Microelectron. Eng. **88** (2011), 391.

[20] _____ , *Stability of valence alternation pairs across the substoichiometric region at Ge/GeO$_2$ interfaces*, Physica B (2011), –.

[21] Mauro Boero, Alfredo Pasquarello, Johannes Sarnthein, and Roberto Car, *Structure and hyperfine parameters of E_1' centers in α-quartz and in vitreous SiO$_2$*, Phys. Rev. Lett. **78** (1997), 887.

[22] Angelo Bongiorno and Alfredo Pasquarello, *Validity of the bond-energy picture for the energetics at Si-SiO$_2$ interfaces*, Phys. Rev. B **62** (2000), R16326.

[23] _____ , *Atomistic structure of the Si(100)–SiO$_2$ interface: A synthesis of experimental data*, Appl. Phys. Lett. **83** (2003), 1417.

[24] Angelo Bongiorno, Alfredo Pasquarello, Mark S. Hybertsen, and L. C. Feldman, *Transition structure at the Si(100)–SiO$_2$ interface*, Phys. Rev. Lett. **90** (2003), 186101.

[25] M. H. Brodsky and R. S. Title, *Electron spin resonance in amorphous silicon, germanium, and silicon carbide*, Phys. Rev. Lett. **23** (1969), 581.

[26] Peter Broqvist, Audrius Alkauskas, and Alfredo Pasquarello, *Band alignments and defect levels in Si–HfO$_2$ gate stacks: Oxygen vacancy and Fermi-level pinning*, Appl. Phys. Lett. **92** (2008), 132911.

[27] _____ , *Defect levels of dangling bonds in silicon and germanium through hybrid functionals*, Phys. Rev. B **78** (2008), 075203.

[28] _____ , *Hybrid-functional calculations with plane-wave basis sets: Effect of singularity correction on total energies, energy eigenvalues, and defect energy levels*, Phys. Rev. B **80** (2009), 085114.

[29] Peter Broqvist, Jan Felix Binder, and Alfredo Pasquarello, (unpublished).

[30] _____, *Atomistic model structure of the Ge(100)–GeO$_2$ interface*, Microelectron. Eng. **86** (2009), 1589.

[31] _____, *Band offsets at the Ge/GeO$_2$ interface through hybrid density functionals*, Appl. Phys. Lett. **94** (2009), 141911.

[32] _____, *Formation of substoichiometric GeO$_x$ at the Ge–HfO$_2$ interface*, Appl. Phys. Lett. **97** (2010), 202908.

[33] _____, *Band offsets at Ge/GeO$_2$ interfaces: Effect of different interfacial bonding patterns*, Microelectron. Eng. **88** (2011), 1467.

[34] _____, *Erratum: "Band offsets at the Ge/GeO$_2$ interface through hybrid density functionals" [Appl. Phys. Lett. **94**, 141911 (2009)]*, Appl. Phys. Lett. **98** (2011), 129901.

[35] Peter Broqvist and Alfredo Pasquarello, *Oxygen vacancy in monoclinic HfO$_2$: A consistent interpretation of trap assisted conduction, direct electron injection, and optical absorption experiments*, Appl. Phys. Lett. **89** (2006), 262904.

[36] _____, *Band gaps and dielectric constants of amorphous hafnium silicates: A first-principles investigation*, Appl. Phys. Lett. **90** (2007), 082907.

[37] _____, *First principles investigation of defects at interfaces between silicon and amorphous high-κ oxides*, Microelectron. Eng. **84** (2007), 2022.

[38] K. L. Brower, *Kinetics of H$_2$ passivation of P$_b$ centers at the (111) Si-SiO$_2$ interface*, Phys. Rev. B **38** (1988), 9657.

[39] W. Bues and H. V. Wartenberg, *Das system Ge/GeO/GeO$_2$*, Zeitschrift für anorganische und allgemeine Chemie **266** (1951), 281.

[40] Nathalie Capron, Peter Broqvist, and Alfredo Pasquarello, *Migration of oxygen vacancy in HfO$_2$ and across the HfO$_2$/SiO$_2$ interface: A first-principles investigation*, Appl. Phys. Lett. **91** (2007), 192905.

[41] A. D. Caunt, H. Mackle, and L. E. Sutton, *The germanium-fluorine bond length in germanium tetrafluoride*, Trans. Faraday Soc. **47** (1951), 943.

[42] M. Caymax, S. Van Elshocht, M. Houssa, A. Delabie, T. Conard, M. Meuris, M.M. Heyns, A. Dimoulas, S. Spiga, M. Fanciulli, J.W. Seo, and L.V. Goncharova, *HfO$_2$ as gate dielectric on Ge: Interfaces and deposition techniques*, Mater. Sci. Eng. B **135** (2006), 256.

[43] S. A. Chambers, T. Droubay, T. C. Kaspar, and M. Gutowski, *Experimental determination of valence band maxima for SrTiO$_3$, TiO$_2$, and SrO and the associated valence band offsets with Si(001)*, J. Vac. Sci. Technol. B **22** (2004), 2205.

[44] Larry A. Curtiss, Paul C. Redfern, Krishnan Raghavachari, and John A. Pople, *Assessment of gaussian-2 and density functional theories for the computation of ionization potentials and electron affinities*, J. Chem. Phys. **109** (1998), 42.

[45] Philipp Dahinden, Peter Broqvist, and Alfredo Pasquarello, *Charge transition levels of nitrogen dangling bonds at Si/SiO$_2$ interfaces: A first-principles study*, Phys. Rev. B **81** (2010), 085331.

119

[46] Andrea Dal Corso, Alfredo Pasquarello, Alfonso Baldereschi, and Roberto Car, *Generalized-gradient approximations to density-functional theory: A comparative study for atoms and solids*, Phys. Rev. B **53** (1996), 1180.

[47] Terri Deegan and Greg Hughes, *An X-ray photoelectron spectroscopy study of the HF etching of native oxides on Ge(111) and Ge(100) surfaces*, Appl. Surf. Sci. **123-124** (1998), 66.

[48] Fabien Devynck, Feliciano Giustino, Peter Broqvist, and Alfredo Pasquarello, *Structural and electronic properties of an abrupt 4H-SiC(001)/SiO$_2$ interface model: Classical molecular dynamics simulations and density functional calculations*, Phys. Rev. B **76** (2007), 075351.

[49] A. Dimoulas, D.P. Brunco, S. Ferrari, J.W. Seo, Y. Panayiotatos, A. Sotiropoulos, T. Conard, M. Caymax, S. Spiga, M. Fanciulli, Ch. Dieker, E.K. Evangelou, S. Galata, M. Houssa, and M.M. Heyns, *Interface engineering for Ge metal-oxide-semiconductor devices*, Thin Solid Films **515** (2007), 6337.

[50] W. F. Egelhoff, *Core-level binding-energy shifts at surfaces and in solids*, Surface Science Reports **6** (1987), 253.

[51] P. E. J. Eriksson and R. I. G. Uhrberg, *Surface core-level shifts on clean si(001) and ge(001) studied with photoelectron spectroscopy and density functional theory calculations*, Phys. Rev. B **81** (2010), 125443.

[52] Christoph Freysoldt, Jörg Neugebauer, and Chris G. Van de Walle, *Fully Ab Initio finite-size corrections for charged-defect supercell calculations*, Phys. Rev. Lett. **102** (2009), 016402.

[53] M. Fuchs, M. Bockstedte, E. Pehlke, and M. Scheffler, *Pseudopotential study of binding properties of solids within generalized gradient approximations: The role of core-valence exchange correlation*, Phys. Rev. B **57** (1998), 2134.

[54] J. L. Gavartin, D. Munoz Ramo, A. L. Shluger, G. Bersuker, and B. H. Lee, *Negative oxygen vacancies in HfO$_2$ as charge traps in high-k stacks*, Appl. Phys. Lett. **89** (2006), 082908.

[55] Luigi Giacomazzi, P. Umari, and Alfredo Pasquarello, *Vibrational spectra of vitreous germania from first-principles*, Phys. Rev. B **74** (2006), 155208.

[56] Paolo Giannozzi, Stefano Baroni, Nicola Bonini, Matteo Calandra, Roberto Car, Carlo Cavazzoni, Davide Ceresoli, Guido L Chiarotti, Matteo Cococcioni, Ismaila Dabo, Andrea Dal Corso, Stefano de Gironcoli, Stefano Fabris, Guido Fratesi, Ralph Gebauer, Uwe Gerstmann, Christos Gougoussis, Anton Kokalj, Michele Lazzeri, Layla Martin-Samos, Nicola Marzari, Francesco Mauri, Riccardo Mazzarello, Stefano Paolini, Alfredo Pasquarello, Lorenzo Paulatto, Carlo Sbraccia, Sandro Scandolo, Gabriele Sclauzero, Ari P Seitsonen, Alexander Smogunov, Paolo Umari, and Renata M Wentzcovitch, *QUANTUM ESPRESSO: A modular and open-source software project for quantum simulations of materials*, J. Phys.: Condens. Matter **21** (2009), 395502.

[57] Feliciano Giustino, Angelo Bongiorno, and Alfredo Pasquarello, *Atomistic models of the Si(100)–SiO$_2$ interface: structural, electronic and dielectric properties*, J. Phys.: Condens. Matter **17** (2005), S2065.

[58] Feliciano Giustino and Alfredo Pasquarello, *Infrared spectra at surfaces and interfaces from first principles: Evolution of the spectra across the Si(100)–SiO₂ interface*, Phys. Rev. Lett. **95** (2005), 187402.

[59] _____, *Theory of atomic-scale dielectric permittivity at insulator interfaces*, Phys. Rev. B **71** (2005), 144104.

[60] Julien Godet, Feliciano Giustino, and Alfredo Pasquarello, *Proton-induced fixed positive charge at the Si(100)-SiO₂ interface*, Phys. Rev. Lett. **99** (2007), 126102.

[61] Gonzalo Gutiérrez and José Rogan, *Structure of liquid GeO₂ from a computer simulation model*, Phys. Rev. E **69** (2004), 031201.

[62] Lester Guttman, *Ring structure of the crystalline and amorphous forms of silicon dioxide*, J. Non-Cryst. Solids **116** (1990), 145.

[63] F. Gygi and A. Baldereschi, *Self-consistent Hartree-Fock and screened-exchange calculations in solids: Application to silicon*, Phys. Rev. B **34** (1986), 4405.

[64] D. R. Hamann, *Energetics of silicon suboxides*, Phys. Rev. B **61** (2000), 9899.

[65] D. R. Hamann, M. Schlüter, and C. Chiang, *Norm-conserving pseudopotentials*, Phys. Rev. Lett. **43** (1979), 1494.

[66] J. Lawrence Hencher and Frank J. Mustoe, *The molecular structure of tetramethylgermane determined by gas phase electron diffraction*, Can. J. Chem. **53** (1975), 3542.

[67] Jochen Heyd, Gustavo E. Scuseria, and Matthias Ernzerhof, *Hybrid functionals based on a screened coulomb potential*, J. Chem. Phys. **118** (2003), 8207.

[68] _____, *Erratum: "Hybrid functionals based on a screened Coulomb potential" [J. Chem. Phys. 118, 8207 (2003)]*, J. Chem. Phys. **124** (2006), 219906.

[69] M. Heyns and M. Houssa, *High-k gate dielectrics*, Series in Material Science and Engineering, Taylor & Francis, 2003, pp. –.

[70] P. Hohenberg and W. Kohn, *Inhomogeneous electron gas*, Phys. Rev. **136** (1964), B864.

[71] M. Houssa, G. Pourtois, V. V. Afanas'ev, and A. Stesmans, *First-principles study of ge dangling bonds in GeO₂ and correlation with electron spin resonance at Ge/GeO₂ interfaces*, Appl. Phys. Lett. **99** (2011), 212103.

[72] M. Houssa, G. Pourtois, M. Caymax, M. Meuris, and M.M. Heyns, *Electronic properties of (001)Ge/Ge(Hf)O₂ interfaces: A first-principles study*, Surf. Sci. **602** (2008), L25.

[73] Michel Houssa, Alessandra Satta, Eddy Simoen, Brice De Jaeger, Marc Meuris, Matty Caymax, and Marc Heyns, *Electrical performance of Ge devices*, Germanium-Based Technologies, Elsevier, Oxford, 2007, pp. 233 – 265.

[74] Kerstin Hummer, Judith Harl, and Georg Kresse, *Heyd-Scuseria-Ernzerhof hybrid functional for calculating the lattice dynamics of semiconductors*, Phys. Rev. B **80** (2009), 115205.

[75] Yoshiki Kamata, *High-k/Ge MOSFETs for future nanoelectronics*, Materials Today **11** (2008), 30.

Bibliography

[76] Marc Kastner, David Adler, and H. Fritzsche, *Valence-alternation model for localized gap states in lone-pair semiconductors*, Phys. Rev. Lett. **37** (1976), 1504.

[77] Keith and Refson, *Moldy: a portable molecular dynamics simulation program for serial and parallel computers*, Comput. Phys. Commun. **126** (2000), 310.

[78] Shirley V. King, *Ring configurations in a random network model of vitreous silica*, Nature **213** (1967), 1112.

[79] K. Kita, S.K. Wang, M. Yoshida, C.H. Lee, K. Nagashio, T. Nishimura, and A. Toriumi, *Comprehensive study of GeO_2 oxidation, GeO desorption and GeO_2-metal interaction -Understanding of Ge processing kinetics for perfect interface control*, Electron Devices Meeting (IEDM), 2009 IEEE International, 2009.

[80] Koji Kita, Sho Suzuki, Hideyuki Nomura, Toshitake Takahashi, Tomonori Nishimura, and Akira Toriumi, *Direct evidence of GeO volatilization from GeO_2/Ge and impact of its suppression on GeO_2/Ge metal–insulator–semiconductor characteristics*, Jpn. J. Appl. Phys. **47** (2008), 2349.

[81] D. D. Koelling and B. N. Harmon, *A technique for relativistic spin-polarised calculations*, J. Phys. C: Solid State Phys. **10** (1977), 3107.

[82] Hannu-Pekka Komsa, Peter Broqvist, and Alfredo Pasquarello, *Alignment of defect levels and band edges through hybrid functionals: Effect of screening in the exchange term*, Phys. Rev. B **81** (2010), 205118.

[83] Hannu-Pekka Komsa and Alfredo Pasquarello, *Intrinsic defects in GaAs and InGaAs through hybrid functional calculations*, Physica B (2011), –.

[84] E. A. Kraut, R. W. Grant, J. R. Waldrop, and S. P. Kowalczyk, *Precise determination of the valence-band edge in X-ray photoemission spectra: Application to measurement of semiconductor interface potentials*, Phys. Rev. Lett. **44** (1980), 1620.

[85] Erik Landemark, C. J. Karlsson, L. S. O. Johansson, and R. I. G. Uhrberg, *Electronic structure of clean and hydrogen-chemisorbed Ge(001) surfaces studied by photoelectron spectroscopy*, Phys. Rev. B **49** (1994), 16523.

[86] Thomas Lange, Walter Njoroge, Hansjörg Weis, Manfred Beckers, and Matthias Wuttig, *Physical properties of thin GeO_2 films produced by reactive DC magnetron sputtering*, Thin Solid Films **365** (2000), 82.

[87] Stephan Lany and Alex Zunger, *Assessment of correction methods for the band-gap problem and for finite-size effects in supercell defect calculations: Case studies for ZnO and GaAs*, Phys. Rev. B **78** (2008), 235104.

[88] G. Le Lay, J. Kanski, P. O. Nilsson, U. O. Karlsson, and K. Hricovini, *Surface core-level shifts on Ge(100): $c(4 \times 2)$ to 2×1 and $1 times 1$ phase transitions*, Phys. Rev. B **45** (1992), 6692.

[89] Choong Hyun Lee, Toshiyuki Tabata, Tomonori Nishimura, Kosuke Nagashio, Koji Kita, and Akira Toriumi, *Ge/GeO_2 interface control with high-pressure oxidation for improving electrical characteristics*, Appl. Phys. Express **2** (2009), 071404.

[90] M Leslie and N J Gillan, *The energy and elastic dipole tensor of defects in ionic crystals calculated by the supercell method*, J. of Phys. C: Solid State Phys. **18** (1985), 973.

[91] M. Levy, *Universal variational functionals of electron densities, first-order density matrices, and natural spin-orbitalsand solution of the v-represtability problem*, Proc. Natl. Sci. USA **76** (1979), 6062.

[92] L. Lin, K. Xiong, and J. Robertson, *Atomic structure, electronic structure, and band offsets at Ge:GeO:GeO$_2$ interfaces*, Appl. Phys. Lett. **97** (2010), 242902.

[93] Steven G. Louie, Sverre Froyen, and Marvin L. Cohen, *Nonlinear ionic pseudopotentials in spin-density-functional calculations*, Phys. Rev. B **26** (1982), 1738.

[94] O. Madelung (ed.), *Physics of group IV elements and III-V compounds*, Springer, Berlin, 1982.

[95] G. Makov and M. C. Payne, *Periodic boundary conditions in ab initio calculations*, Phys. Rev. B **51** (1995), 4014.

[96] Richard M. Martin, *Electronic structure: Basic theory and practical methods*, Cambridge University Press, 2004.

[97] E. Martinez, O. Renault, L. Fourdrinier, L. Clavelier, C. Le Royer, C. Licitra, T. Veyron, J. M. Hartmann, V. Loup, L. Vandroux, M. J. Guittet, and N. Barrett, *Band offsets of HfO$_2$/GeON/Ge stacks measured by ultraviolet and soft x-ray photoelectron spectroscopies*, Appl. Phys. Lett. **90** (2007), 053508.

[98] Nicola Marzari and David Vanderbilt, *Maximally localized generalized Wannier functions for composite energy bands*, Phys. Rev. B **56** (1997), 12847.

[99] Hiroshi Matsubara, Takashi Sasada, Mitsuru Takenaka, and Shinichi Takagi, *Evidence of low interface trap density in GeO$_2$/Ge metal-oxide-semiconductor structures fabricated by thermal oxidation*, Appl. Phys. Lett. **93** (2008), 032104.

[100] M Micoulaut, L Cormier, and G S Henderson, *The structure of amorphous, crystalline and liquid GeO$_2$*, J. Phys.: Condens. Matter **18** (2006), R753.

[101] Alessandro Molle, Md. Nurul Kabir Bhuiyan, Grazia Tallarida, and Marco Fanciulli, *In situ chemical and structural investigations of the oxidation of Ge(001) substrates by atomic oxygen*, Appl. Phys. Lett. **89** (2006), 083504.

[102] Gordon E. Moore, *Cramming more components onto integrated circuits*, Electronics **38** (1965), 8.

[103] Arash A. Mostofi, Jonathan R. Yates, Young-Su Lee, Ivo Souza, David Vanderbilt, and Nicola Marzari, *wannier90: A tool for obtaining maximally-localised Wannier functions*, Comput. Phys. Commun. **178** (2008), 685.

[104] Jungwoo Oh and Joe Campbell, *Thermal desorption of Ge native oxides and the loss of Ge from the surface*, J. Electron. Mater. **33** (2004), 364.

[105] Keiichi Ohno, Hiroatsu Matsuura, Yasuki Endo, and Eizi Hirota, *The microwave spectra of deuterated silanes, germanes, and stannanes*, J. Mol. Spectrosc. **118** (1986), 1.

[106] Akio Ohta, Hiroshi Nakagawa, Hideki Murakami, Seiichirou Higashi, and Seiichi Miyazaki, *Photoemission study of ultrathin GeO$_2$/Ge heterostructures formed by UV-O$_3$ oxidation*, e-J. Surf. Sci. and Nanotech. **4** (2006), 174.

[107] Alfredo Pasquarello, *Network transformation processes during oxidation of silicon*, Microelectron. Eng. **48** (1999), 89.

[108] Alfredo Pasquarello, Mark S. Hybertsen, and Roberto Car, *Si 2p core-level shifts at the Si(001)-SiO$_2$ interface: A first-principles study*, Phys. Rev. Lett. **74** (1995), 1024.

[109] ———, *Comparison of structurally relaxed models of the Si(001)-SiO$_2$ interface based on different crystalline oxide forms*, Appl. Surf. Sci. **104-105** (1996), 317.

[110] ———, *Si 2p core-level shifts in small molecules: A first principles study*, Phys. Scr. **T66** (1996), 118 (English).

[111] ———, *Structurally relaxed models of the Si(001)–SiO$_2$ interface*, Appl. Phys. Lett. **68** (1996), 625.

[112] ———, *Theory of Si 2p core-level shifts at the Si(001)-SiO$_2$ interface*, Phys. Rev. B **53** (1996), 10942.

[113] ———, *Interface structure between silicon and its oxide by first-principles molecular dynamics*, Nature **396** (1998), 58.

[114] G. Pastore, E. Smargiassi, and F. Buda, *Theory of ab initio molecular-dynamics calculations*, Phys. Rev. A **44** (1991), 6334.

[115] E. Pehlke and M. Scheffler, *Evidence for site-sensitive screening of core holes at the Si and Ge (001) surface*, Phys. Rev. Lett. **71** (1993), 2338.

[116] John P. Perdew, Kieron Burke, and Matthias Ernzerhof, *Generalized gradient approximation made simple*, Phys. Rev. Lett. **77** (1996), 3865.

[117] John P. Perdew, Matthias Ernzerhof, and Kieron Burke, *Rationale for mixing exact exchange with density functional approximations*, J. Chem. Phys. **105** (1996), 9982.

[118] John P. Perdew and Stefan Kurth, *Density functionals for non-relativistic coulomb systems*, Density Functionals: Theory and Applications (D. Joubert, ed.), Springer, 1997.

[119] M. Perego, G. Scarel, M. Fanciulli, I. L. Fedushkin, and A. A. Skatova, *Fabrication of GeO$_2$ layers using a divalent ge precursor*, Appl. Phys. Lett. **90** (2007), 162115.

[120] M. Perego, G. Seguini, and M. Fanciulli, *Energy band alignment of HfO$_2$ on Ge*, J. Appl. Phys. **100** (2006), 093718.

[121] Ravi Pillarisetty, *Academic and industry research progress in germanium nanodevices*, Nature **479** (2011), 324.

[122] G. Pourtois, M. Houssa, A. Delabie, T. Conard, M. Caymax, M. Meuris, and M. M. Heyns, *Ge 3d core-level shifts at (100)Ge/Ge(Hf)O$_2$ interfaces: A first-principles investigation*, Appl. Phys. Lett. **92** (2008), 032105.

[123] K. Prabhakaran, F. Maeda, Y. Watanabe, and T. Ogino, *Thermal decomposition pathway of Ge and Si oxides: observation of a distinct difference*, Thin Solid Films **369** (2000), 289.

[124] K. Prabhakaran and T. Ogino, *Oxidation of Ge(100) and Ge(111) surfaces: an UPS and XPS study*, Surface Science **325** (1995), 263.

[125] David L. Price, Marie-Louise Saboungi, and Adrian C. Barnes, *Structure of vitreous germania*, Phys. Rev. Lett. **81** (1998), 3207.

[126] Sebastien Le Roux and Philippe Jund, *Ring statistics analysis of topological networks: New approach and application to amorphous GeS_2 and SiO_2 systems*, Computational Materials Science **49** (2010), 70.

[127] Jayanta K. Rudra and W. Beall Fowler, *Oxygen vacancy and the $E_1^{'}$ center in crystalline SiO_2*, Phys. Rev. B **35** (1987), 8223.

[128] Philip S. Salmon, Adrian C. Barnes, Richard A. Martin, and Gabriel J. Cuello, *Structure of glassy GeO_2*, J. Phys.: Condens. Matter **19** (2007), 415110.

[129] D. Schmeisser, R.D. Schnell, A. Bogen, F.J. Himpsel, D. Rieger, G. Landgren, and J.F. Morar, *Surface oxidation states of germanium*, Surface Science **172** (1986), 455.

[130] R. D. Schnell, F. J. Himpsel, A. Bogen, D. Rieger, and W. Steinmann, *Surface core-level shifts for clean and halogen-covered Ge(100) and Ge(111)*, Phys. Rev. B **32** (1985), 8052.

[131] Kang-Ill Seo, Paul C. McIntyre, Shiyu Sun, Dong-Ick Lee, Piero Pianetta, and Krishna C. Saraswat, *Chemical states and electronic structure of a HfO_2/Ge(001) interface*, Appl. Phys. Lett. **87** (2005), 042902.

[132] R. Shaltaf, G.-M. Rignanese, X. Gonze, Feliciano Giustino, and Alfredo Pasquarello, *Band offsets at the Si/SiO_2 interface from many-body perturbation theory*, Phys. Rev. Lett. **100** (2008), 186401.

[133] William B. Shockley, John Bardeen, and Walter H. Brattain, *Nobel prize in physics 1956 - presentation speech*, Nobel Lectures, Physics 1942-1962, Elsevier Publishing Company, Amsterdam, 1964.

[134] L. N. Skuja, *Photoluminescence of intrinsie defects in glassy GeO_2. Twofold coordinated Ge and nonbridging oxygen*, Phys. Status Solidi A **114** (1989), 731.

[135] J. A. Speer and B. J. Cooper, *Crystal-structure of synthetic hafnon, $HfSiO_4$, comparison with zircon and the actinide orthosilicates*, Am. Mineral. **67** (1982), 804.

[136] A. Stesmans, *Interaction of P_b defects at the (111)Si/SiO_2 interface with molecular hydrogen: Simultaneous action of passivation and dissociation*, J. Appl. Phys. **88** (2000), 489.

[137] M. Stutzmann and J. Stuke, *Paramagnetic states in doped amorphous silicon and germanium*, Solid State Commun. **47** (1983), 635.

[138] Tomoyuki Tamura, Guang-Hong Lu, Ryoichi Yamamoto, and Masanori Kohyama, *First-principles study of neutral oxygen vacancies in amorphous silica and germania*, Phys. Rev. B **69** (2004), 195204.

[139] M. Tanenbaum, L. B. Valdes, E. Buehler, and N. B. Hannay, *Silicon n-p-n grown junction transistors*, J. Appl. Phys. **26** (1955), 686.

[140] Samuel E. Taylor and Fabien Bruneval, *Understanding and correcting the spurious interactions in charged supercells*, Phys. Rev. B **84** (2011), 075155.

[141] G. te Velde, F. M. Bickelhaupt, E. J. Baerends, C. Fonseca Guerra, S. J. A. van Gisbergen, J. G. Snijders, and T. Ziegler, *Chemistry with ADF*, J. Comput. Chem. **22** (2001), 931.

[142] N. Troullier and José Luriaas Martins, *Efficient pseudopotentials for plane-wave calculations*, Phys. Rev. B **43** (1991), 1993.

[143] L. Tsetseris and S. T. Pantelides, *Morphology and defect properties of the Ge–GeO$_2$ interface*, Appl. Phys. Lett. **95** (2009), 262107.

[144] Yuhai Tu and J. Tersoff, *Structure and energetics of the Si–SiO$_2$ interface*, Phys. Rev. Lett. **84** (2000), 4393.

[145] Chris G. Van de Walle and Richard M. Martin, *Theoretical calculations of heterojunction discontinuities in the Si/Ge system*, Phys. Rev. B **34** (1986), 5621.

[146] Chris G. Van de Walle and Jörg Neugebauer, *First-principles calculations for defects and impurities: Applications to III-nitrides*, J. Appl. Phys. **95** (2004), 3851.

[147] E. van Lenthe, E. J. Baerends, and J. G. Snijders, *Relativistic regular two-component Hamiltonians*, J. Chem. Phys. **99** (1993), 4597.

[148] Petr Viscor, *In-situ measurements of the density of amorphous germanium prepared in ultra-high vacuum*, J. Non-Cryst. Solids **101** (1988), 170.

[149] Akira Wada, Kazuhiko Endo, Meishoku Masahara, Chi-Hsien Huang, and Seiji Samukawa, *Low activation energy, high-quality oxidation of Si and Ge using neutral beam*, Appl. Phys. Lett. **98** (2011), 203111.

[150] Sheng Kai Wang, Koji Kita, Choong Hyun Lee, Toshiyuki Tabata, Tomonori Nishimura, Kosuke Nagashio, and Akira Toriumi, *Desorption kinetics of GeO from GeO$_2$/Ge structure*, J. Appl. Phys. **108** (2010), 054104.

[151] J. R. Weber, A. Janotti, P. Rinke, and C. G. Van de Walle, *Dangling-bond defects and hydrogen passivation in germanium*, Appl. Phys. Lett. **91** (2007), 142101.

[152] Clemens Winkler, *Mittheilungen über das Germanium*, Journal für Praktische Chemie **34** (1886), 177.

[153] _____ , *Mittheilungen über das Germanium*, Journal für Praktische Chemie **36** (1887), 177.

[154] F. Wooten, K. Winer, and D. Weaire, *Computer generation of structural models of amorphous Si and Ge*, Phys. Rev. Lett. **54** (1985), 1392.

[155] Adrian C. Wright, George Etherington, J. A. Erwin Desa, Roger N. Sinclair, G. A. N. Connell, and J. C. Mikkelsen Jr., *Neutron amorphography*, J. Non-Cryst. Solids **49** (1982), 63.

[156] K. Xiong, Y. Du, K. Tse, and J. Robertson, *Defect states in the high-dielectric-constant gate oxide HfSiO$_4$*, J. Appl. Phys. **101** (2007), 024101.

[157] K. Xiong, J. Robertson, M. C. Gibson, and S. J. Clark, *Defect energy levels in HfO$_2$ high-dielectric-constant gate oxide*, Appl. Phys. Lett. **87** (2005), 183505.

[158] M. Yang, R. Q. Wu, Q. Chen, W. S. Deng, Y. P. Feng, J. W. Chai, J. S. Pan, and S. J. Wang, *Impact of oxide defects on band offset at GeO$_2$/Ge interface*, Appl. Phys. Lett. **94** (2009), 142903.

[159] Oleg V. Yazyev and Alfredo Pasquarello, *Origin of fine structure in Si 2p photoelectron spectra at silicon surfaces and interfaces*, Phys. Rev. Lett. **96** (2006), 157601 (English).

[160] S. B. Zhang and John E. Northrup, *Chemical potential dependence of defect formation energies in GaAs: Application to Ga self-diffusion*, Phys. Rev. Lett. **67** (1991), 2339.

Acknowledgements

CURRICULUM VITAE

JAN FELIX BINDER

PRESENT ADDRESS

Bd. de Perolles 15
1700 Fribourg
Switzerland

PERSONAL DETAILS

Gender : Male
Date of birth : 27th of November, 1979
Place of birth : Hameln, Germany
Nationality : German

EDUCATION

05/2008–04/2012	Ph.D. in Physics, École Polytechnique Fédérale de Lausanne, Switzerland. Thesis : "Electronic and Structural Properties of the Ge/GeO_2 Interface through Hybrid Functionals". Supervisor : Alfredo Pasquarello.
01/2007–12/2007	Diploma thesis in Physics, Universität Hamburg, Germany. Thesis : "*Ab-initio* Studies of Cobalt on Platinum (111)". Supervisor : Alexander Lichtenstein.
04/2003–12/2007	Undergraduate studies in Physics, Universität Hamburg.

PUBLICATIONS

J. F. Binder, P. Broqvist, and A. Pasquarello,
First principles study of substoichiometric germanium oxides,
Microelectronic Engineering, **86** (2009), 1760.

P. Broqvist, J. F. Binder, and A. Pasquarello,
Band offsets at the Ge/GeO$_2$ interface through hybrid density functionals,
Applied Physics Letters, **94** (2009), 141911.
Citations : **17**

P. Broqvist, J. F. Binder, and A. Pasquarello,
Atomistic model structure of the Ge(100)-GeO$_2$ interface,
Microelectronic Engineering, **86** (2009), 1589.

J. F. Binder, P. Broqvist, and A. Pasquarello,
Electron trapping in substoichiometric germanium oxide,
Applied Physics Letters, **97** (2010), 092903.
Citations : **12**

P. Broqvist, J. F. Binder, and A. Pasquarello,
Formation of substoichiometric GeO$_x$ at the Ge–HfO$_2$ interface,
Applied Physics Letters, **97** (2010), 202908.

J. F. Binder, P. Broqvist, and A. Pasquarello,
Electron density of states at Ge/oxide interfaces due to GeO$_x$ formation,
Microelectronic Engineering, **88** (2011), 391.

J. F. Binder, P. Broqvist, and A. Pasquarello,
Charge trapping in substoichiometric germanium oxide,
Microelectronic Engineering, **88** (2011), 1428.

J. F. Binder, P. Broqvist, and A. Pasquarello,
Stability of valence alternation pairs across the substoichiometric region at Ge/GeO$_2$ interfaces,
Physica B (in press), doi : 10.1016/j.physb.2011.08.075.

P. Broqvist, J. F. Binder, and A. Pasquarello,
First principles study of electronic and structural properties of the Ge/GeO$_2$ interface,
Physica B (in press), doi : 10.1016/j.physb.2011.08.037.

P. Broqvist, J. F. Binder, and A. Pasquarello,
Band offsets at Ge/GeO$_2$ interfaces : Effect of different interfacial bonding patterns,
Microelectronic Engineering, **88** (2011), 1467.

J. F. Binder, P. Broqvist, H. P. Komsa and A. Pasquarello,
Germanium core-level shifts at Ge/GeO$_2$ interface through hybrid functionals,
submitted to Physical Review B.

Insulating Films on Semiconductors (INFOS)
29th of June to the 1st of July 2009, Clare Collage, Cambridge, UK.

E-MRS Spring Meeting
7th of June to the 11th of June 2010, Congress Center, Strasbourg, France.

Psi-K conference 2010
12th of September to 16th of September 2010, Henry Ford Building at Freie Universitat Berlin.

Insulating Films on Semiconductors (INFOS)
21th of June to 24st of June 2011, Grenoble,France.

13th International Conference on the Formation of Semiconductor Interfaces
3th of July to 8th of July 2011, Prague, Czech Republic.